ARL

The University of Texas at Austin

TECHNICAL REPORT

ARL-TR-99-2
1 July 1999

Copy Number 3

Plasma Sound Source Basic Research

Final Report under Grant N00014-94-1-0150
1 November 1993 - 30 September 1997

Robert L. Rogers, James C. Espinosa,
David L. Fisher, and Austin M. Gleeson

Prepared for: Office of Naval Research
Department of the Navy • Arlington, VA 22217-5660

Applied Research Laboratories•The University of Texas at Austin•Post Office Box 8029•Austin, Texas 78713-8029

REPORT DOCUMENTATION PAGE

Form Approved
OMB No. 0704-0188

1. REPORT DATE *(DD-MM-YYYY)*	2. REPORT TYPE	3. DATES COVERED *(From - To)*
01-07-1999	Final	1 Nov 1993 - 30 Sep 1997

4. TITLE AND SUBTITLE
PLASMA SOUND SOURCE BASIC RESEARCH

5a. CONTRACT NUMBER

5b. GRANT NUMBER
N00014-94-1-0150

5c. PROGRAM ELEMENT NUMBER
61153N

6. AUTHOR(S)
Rogers, Robert L.
Espinosa, James C.
Fisher, David L.
Gleeson, Austin M.

5d. PROJECT NUMBER

5e. TASK NUMBER

5f. WORK UNIT NUMBER

7. PERFORMING ORGANIZATION NAME(S) AND ADDRESS(ES)
APPLIED RESEARCH LABORATORIES
THE UNIVERSITY OF TEXAS AT AUSTIN
P O BOX 8029
AUSTIN TX 78713-8029

8. PERFORMING ORGANIZATION REPORT NUMBER
ARL-TR-99-2

9. SPONSORING/MONITORING AGENCY NAME(S) AND ADDRESS(ES)
OFFICE OF NAVAL RESEARCH
ONR 331
800 NORTH QUINCY STREET
ARLINGTON VA 22217-5000

10. SPONSOR/MONITOR'S ACRONYM(S)
ONR

11. SPONSORING/MONITORING AGENCY REPORT NUMBER

12. DISTRIBUTION AVAILABILITY STATEMENT
Approved for public release:
Distribution unlimited.

13. SUPPLEMENTARY NOTES

14. ABSTRACT

This report investigates the phenomena of breakdown and initial arc formation of a plasma sound source. The prebreakdown phase is examined experimentally. A proton-hopping model is proposed that is qualitatively consistent with the data. A literature review of the behavior of water near electrodes shows water having a regular, solid-like structure, permitting use of proton-hopping models to calculate specifics of ion transport in the electrode vicinity. A mechanism for obtaining the transition of the H+ ions to a high mobility state and shortcomings of electron-based breakdown models are discussed. Experimental data indicate that breakdown occurs from structures not strongly pressure dependent. An arc model (finite difference one-dimensional) is developed showing interior dynamics of the discharge and conversion of electrical energy to hydromechanical energy on the bubble, including radiative and conductive heat transport, particle transport, ionization, compressibility of the filling plasma, and the compressibility of the surrounding water. Some calculated results of this model are presented.

15. SUBJECT TERMS
Breakdown and initial arc formation of a plasma sound source; Conversion of electrical to hydromechanical energy; Electron-based breakdown models; and Plasma sound source.

16. SECURITY CLASSIFICATION OF:			17. LIMITATION OF ABSTRACT	18. NUMBER OF PAGES	19a. NAME OF RESPONSIBLE PERSON
a. REPORT	b. ABSTRACT	c. THIS PAGE			19b. TELEPONE NUMBER *(Include area code)*
UU	UU	UU		102	

This page intentionally left blank.

TABLE OF CONTENTS

Page

LIST OF FIGURES

LIST OF TABLES

This page intentionally left blank.

1.0 OVERVIEW AND BACKGROUND

Plasma sound sources (PSS), or sparkers, have been used for many years in the geophysical prospecting business. Efforts to improve the state of the art of spark sources have met with limited success, especially in salt water, because the mechanisms leading to the breakdown and formation of the arc have not been well understood. The breakdown and arc formation are key factors in governing how efficiently electrical energy can be transferred to the plasma, and ultimately to sound. Prior efforts have shown that electrical parameters of the discharge circuit have a major influence on the frequency and amplitude of the sound produced.[1]

This report documents the latest efforts to understand the phenomena associated with arc formation and electrical-to-acoustic transduction. Related efforts previous to this effort focused on the internal transport processes and the dissociation and ionization of the water as energy was deposited in the bubble.[2] Also, a semi-empirical model was developed that allowed accurate calculation of the bubble hydrodynamic signature, and was incorporated into a model that allowed the calculation of the full hydrodynamics of multiple bubbles generated in close proximity.[3] The work documented in the following sections is the next step, and focuses on the prebreakdown and arc formation phase, as well as the interior dynamics of the arc after it is formed.

One of the most important factors in understanding the behavior of the transduction mechanism is understanding the processes involved in the dielectric breakdown of water and the formation of an arc. Very little progress has been made in recent years in developing theories that adequately explain observed behavior. In this work, a significant effort was made to understand the dielectric breakdown processes of water and to focus on the dielectric breakdown behavior in the parameter regimes that occur during the formation of a typical discharge of a PSS.

Many theories use electrons as the primary charge transport mechanisms for breakdown in water. However, high speed photographic evidence collected under this effort, and documented in the literature, shows that the leaders are primarily initiated from the anode and not from the cathode. Thus, these theories have to be patched up to account for this behavior. A new theoretical approach is given here that does not use electron transport, but rather considers protons, or hydronium ions (H+), as the primary charge carrier. Experimental and theoretical evidence is also given that strongly suggests that thermal mechanisms, that is, steam bubble generation and subsequent breakdown in the bubble, do not accurately account for the behavior observed during the prebreakdown phase. Because of the complexity of charge transport in salt water, the theory presented here is primarily useful for explaining the breakdown in fresh water.

This report is divided into two main parts. First is the discussion of the dielectric breakdown. This section discusses many of the above points. The second section is the discussion of the arc modeling in water. Some initial calculated results are given that show that the interior dynamics of the arc have a number of interesting processes that occur, including the generation of radial acoustic waves that are excited by the resistive gradients in the arc. Finally, the conclusion discusses what further investigations might be made in understanding these phenomena.

2.0 BACKGROUND, THEORY, AND EXPERIMENT

2.1 INTRODUCTION

Dielectric breakdown is a spatially local phase transition in the electrical conductivity of a material. When a material is placed between two metal electrodes having a very large voltage drop between them, a tree-like spark will race across the material, discharging the voltage. The first investigations centered around dilute gases because of their relative simplicity. With the advancement of technology and condensed matter physics, it became possible to study both solids and liquids. Water has been one of the most studied, but also the least understood, of liquids. Almost all previous breakdown models have tried to incorporate electron avalanches, but all have failed to explain the phenomenon on even a qualitative level. A new approach will be presented in this section that will not rely on free electrons.

This phenomenon has been mostly studied by pulsed power engineers who are interested in using water in capacitors in order to increase their energy storage capacity. The work at Applied Research Laboratories, The University of Texas at Austin (ARL:UT), has focused on using underwater arcs as a source of low frequency sound and in increasing their transduction efficiency in sea water. *Understanding the breakdown process in water is critical for the development of efficient spark or plasma sound sources.* For the past 40 years, numerous experiments have been conducted around the world, examining the macroscopic phenomenology. The field strength and electrode geometry used at ARL:UT was sufficiently different than the literature that it was necessary to conduct experiments in order to show that these underwater discharges are fundamentally the same as previous studies. Unfortunately, no condensed matter or plasma physics experimentalists have been interested in this problem, so there is no microscopic information about dielectric breakdown in water. All previous models, including the present one, have been handicapped by this lack of data and have had to rely solely on the phenomenology. The current model

will rely on simulations done by quantum chemists for a microscopic picture of electrical conduction in water.

A summary will first be given of the macroscopic phenomenology of dielectric breakdown. It is impossible to include all experimental studies, which would only serve to confuse, so only the key points will be touched upon and the most significant papers referenced. A survey of previous models will then be presented with comments on how they fail qualitatively. Afterwards, a section will be devoted to discussing what is known about electrical conduction in pure water and how this knowledge affects these theories. Experimental data collected at ARL:UT will then be presented in order to show that bubble formation is a secondary phenomenon for these longer time scales. Sequences of photographs combined with oscillograms will be included in the presentation. From the phenomenology and the microscopic picture of water, a model will then be formulated that will consist of a near-liquid density wavefront that will be made up of excess charge inhabiting a region of aligned water molecules. Some simple one-dimensional calculations will be presented, and future possible experiments will be suggested in order to test this model further.

2.2 LITERATURE SURVEY

2.2.1 Breakdown Experiments

When two metal electrodes are placed in water and a sufficiently high voltage is placed across them, a tree-like structure grows off one of the electrodes and bridges the gap, forming an arc. This phenomena is called dielectric breakdown. An instructive example is the sequence of photographs with 0.4 μs time intervals taken by Mel'nikov et al.[4] Here, the gap is being illuminated by an arc light and is about 5 mm across; the initial voltage is about 12 kV. As seen in the frames, the leaders are much less luminous than the arc that is formed and either absorb or scatter the backlighting, appearing as dark filaments in the photograph. The tip of the leaders are at liquid water density.[5,6]

The approximate speed of leaders is 1 mm/μs, and they are about 0.1 mm thick. The stage before arc formation is called the prebreakdown stage. If the leaders do not cross the gap, the phenomena is called a corona. Whether any electrical discharge that does not produce leaders can be called a corona is not clear when reading through the literature, but for this study, this term will be used for any discharge that does not result in breakdown.

Studying dielectric breakdown in water is difficult because any experiments to study the microscopic nature of leaders are masked by the opacity of water, by bulk ionic currents, and by the destructive nature of the prebreakdown stage. Any spectra of water that are collected will only observe the visible spectrum since any other frequency radiation is strongly absorbed. The bulk ionic currents make it impossible to measure the current density in a leader. After one discharge, the electrode has become pitted and the water contaminated. These experimental difficulties have limited the type of information known about leader growth.

There are three types of data that have been collected: photographs, oscillograms, and visible spectra. The photos have been almost exclusively taken with framing cameras that are capable of a million frames per second.[7,8] The backlighting is either with light from a spark or a laser. Oscillograms of the voltage are usually measured indirectly by placing a high impedance resistor in parallel with the test cell and measuring the current with a current transformer. The gap current can be measured directly. Visible spectra have been taken in only one published experiment, and it is not obvious what physical significance they have.[9]

The only way to try to understand the electrical breakdown of water has been to observe how varying experimental conditions change leader growth. There are basically five different parameters that have been varied: dissolved impurities, bulk electric field, ambient hydrostatic pressure, electrode polarity, and electrode material. The dissolved impurities are always a type of salt. The

magnitude of the field has been increased by either raising the applied potential or making the field divergent by changing the electrode geometry. The polarity has been switched in an asymmetrical geometry such as a point-to-plate while keeping everything else constant. Finally, different metals have been used for the electrodes. Several important facts have been acquired by adjusting these five experimental parameters.

The first important piece of information is that the average velocity of leaders is proportional to the concentration of the impurities and not to the low dc field conductivity. L. G. Kutsenko and A. V. Kortnev[10] conducted a series of dielectric breakdown experiments in aqueous lithium chloride solutions; this type of solution has the unusual property of having a double-valued conductivity versus concentration curve.[5] Low concentrations have the same conductivity as high concentrations. The result of the experiment was that the breakdown time for two different concentrations, but the same conductivity, were not the same. Mel'nikov et al. used a crude point-to-plate electrode configuration to find the relationship between leader velocity and conductivity in aqueous sodium chloride solutions.[8] For the range 6×10^{-6} to 10^{-3} $\Omega^{-1}cm^{-1}$, the velocity is proportional to the square root of the conductivity while for higher values the velocity is constant. All the breakdown times for the above two experiments were on the order of microseconds. Jones and Kunhardt found that impurities had no effect on the breakdown time in nanoseconds.[11] Finally, from photographic evidence of microsecond experiments, it is clear that impurities make leaders branch out more with increase of concentration.

The effects of varying bulk field has also been studied. Naugol'nykh and Roi[12] found that a minimum field of 36 kV/cm is needed for leader formation. Mel'nikov et al., using a point-to-plate setup, observed that the velocity of leader growth increases monotonically with field and is on the order of 1 mm/μs.[13]

Pressure effects were found to depend on the timescale of the electrical discharge. Naugol'nykh and Roi[12] state that for bulk electric fields greater than

36 kV/cm and for microsecond breakdown times, there was no change in the discharge for pressures as high as 1000 atm. Jones and Kunhardt[14] found a weak pressure dependence for nanosecond discharges; the pressure range investigated went up to 4000 psi.

Electrode polarity has a large effect on the leader growth. Alkimov took photographs of a discharge occurring between two spheres and found that leaders grew off the anode and not the cathode.[15] Naugol'nykh and Roi, using point-to-plate electrode geometry, found that ten times the field is needed for leader growth when the point is the cathode versus anode.[12] They also found that leaders coming off a positive electrode travel about twice as fast as leaders coming off a negative electrode. Finally, polarity also affects the amount of branching of the leaders. Anodic leaders tend to be filamentary, while cathodic leaders tend to be bush-like.

The last experimental parameter that has been examined is the electrode material. Gripshover et al. studied four different types of materials: aluminum, brass, copper, and stainless steel. They observed that brass, copper, and stainless steel electrodes all had the same dielectric strength, while aluminum had about half the same strength. It was not stated if there was any difference in leader velocity or appearance.[16]

2.2.2 Breakdown Theories

There are basically two different models used to describe dielectric breakdown in water: electronic and thermal. The first model treats the liquid like a gas and relies on the macroscopic similarity between leaders in water and in gases. Without any theoretical calculation or experimental proof, it is stated that electron avalanches are produced at liquid densities.[17] To this date, there is no paper that develops this theory beyond just making analogies with gases; therefore, there will be no further discussion of electronic models.

Thermal models circumvent the problem of showing that electron avalanches can be produced at liquid densities by lowering the density of the water through joule heating. Many models require that a gas bridge be formed between the two electrodes before any electron avalanches form. Olson and Sutton use a thermodynamic approach to studying dielectric breakdown.[18] They calculated the energy needed to produce a steam bubble and found the amount needed not to be more than the amount discharged. Combining this result with acoustic data that show bubble growth, they conclude that breakdown results through dielectric breakdown of a steam bubble formed by joule heating. All photographic data taken by previous investigators invalidate this type of model. Breakdown for the field strengths used by Olson and Sutton is always by the formation of leaders.

Jones and Kunhardt developed a thermal model that actually gives a microscopic picture of dielectric breakdown.[14] They relied on field emission from a cathode. The ejected electrons heat up the water just enough to create a low density region large enough to support an electron avalanche, which then goes on to lower the density of another section of the water. The density of this gaseous region is set by a localization criterion experimentally discovered by P. Krebs. In order for an avalanche to form, the density must be less than this critical value.[19] This thermal wave then travels across the gap, leaving behind a highly ionized plasma gas. Once the wave bridges the gap, an arc is formed. The difficulty with this model is that it only works for a point-to-plate geometry, with the point being a cathode. The experiments conducted by Jones and Kunhardt used a parallel plate geometry; all photographs of symmetrical electrodes show leaders growing off of the anode and not the cathode.[14] It would seem that photographic evidence by itself would exclude this mechanism from occurring in their experiment but does not exclude the possibility of being correct for cathode point-to-plate experiments.

Some investigators have attempted to formulate a simplistic fluid model of proton hopping, but the calculations are so brief, they will not be discussed, but

are mentioned because they gave impetus to another idea, developed later in this report.[20,21]

2.2.3 Physical Chemistry of Water

To have any chance of success in modeling dielectric breakdown in water, it is important to understand charge transport in liquid water. To be able to evaluate the idea that electron avalanches can exist at liquid density, one must have a clear picture of the electronic band structure of water. The scientists most interested in studying electron dynamics and charge transport are radiation and physical chemists.[22] Goulet et al. have evaluated all the data acquired by radiation chemists and have arrived at a tentative picture for the electronic energy band structure.[23] They state that the band gap is about 9 eV, which makes water a very good electron insulator. The conduction and valence bands also have very sharp edges, making any kind of argument for Anderson delocalization for electrons in liquid water seem very implausible. The energy to dissociate a water molecule in pure water is about 0.5 eV/molecule. Thus, it takes an order of magnitude less energy to create excess protons than is required to create free electrons.

Protons, also known as hydronium ions (H^+), have a mobility of 3.62×10^{-3} $cm^2V^{-1}s^{-1}$, while hydroxyl ions (OH^-) have a mobility of 1.98×10^{-3} $cm^2V^{-1}s^{-1}$; solvated electrons (e_{aq}^-) have a mobility of 1.98×10^{-3} $cm^2V^{-1}s^{-1}$.[21-26] Any impurity ions like sodium or chloride have lower mobilities than excess protons because they become solvated; surrounding water molecules align their dipoles toward the impurity.[27] In order for the ion to move, it must carry along this polarization, which makes its effective mass far higher than an excess proton. "Pure" water does not have any solvated electrons but only hydroniums and hydroxyls. Low field conduction occurs by what has been called a Grotthus' mechanism.[24] Instead of an actual proton being moved spatially from one point to another, a series of bonds are broken and reformed, moving a positive charge in the direction of the electric field. There are many classical models that attempt to

describe proton migration, but none have been able to explain it quantitatively. The most popular model pictures proton migration as consisting of protons jumping from one water molecule to another one. The two rate-determining mechanisms are the rotation of an acceptor molecule and then the tunneling from a donor to an acceptor. A recent quantum model by Lobaugh and Voth points to the fact that proton transport is a quantum effect and should not be described by a classical picture.[28–32]

Until now, only the properties of the bulk water have been discussed. The water adjacent to an electrode is very complicated and has only recently been studied. To date, there has been only one experimental study of a charged electrode/water interface. M. Toney et al. used x-ray scattering from a silver electrode/NaF aqueous solution to study the structure of the interfacial layer of water.[33] They found that at a critical surface charge the interfacial water molecules have their electric dipoles aligned with the field and become compressed up to three times the density of bulk water. For the same charge density, both of these effects are stronger when the charge is positive versus negative. These results have been partially corroborated by quantum chemists using computer simulations. X. Xia and M. Berkowitz modeled the interfacial water and found that the dipoles do become aligned at the reported fields but that the compression is much less than that the experimentalists claim.[34–36] The main difference between the simulation and the experiment is that the computer program used pure water because including the NaF ions was too difficult. This ion omission may account for the differences in the results.

2.3 THEORY

2.3.1 Introduction

At the beginning of this report, it was stated that dielectric breakdown is not initiated by electron avalanches. In order to see why this viewpoint is useful, it is necessary to discuss charge transport in condensed matter. The beginning

of the discussion will describe how quasi-classical ideas for excess electrons fail at liquid water densities. Quantum field theoretic calculations or molecular dynamics simulations must be performed in order to describe the interaction of an excess electron with a surrounding liquid.[37–41] Over the years, a qualitative picture of transport of a single excess electron in water has emerged. It will be seen that excess electrons are very localized and should not be pictured quasi-classically; a quantum mechanical picture must be used. Instead of the classical idea of avalanches produced by collisions, a leader could be a region where the electron band structure has changed, creating inhabited extended states which contribute to a macroscopic increase in conductivity. Many materials that can undergo bulk metal insulator transitions have been modeled using various body physics. The classification system for the different possible transitions developed over the years will be used in order to see how water could become an electronic conductor and demonstrate the difficulty of such a scenario.

For low electric fields, chemists view water as an ionic conductor, and for very low impurity concentrations, proton transport is the accepted mechanism for charge conduction. The standard theory for proton hopping will be extended in order to describe the microscopic physics of a leader; the extension will make heavy use of previous work by physicists working on conduction in ice.[42–51] The leaders will be seen to consist of collective excitations, represented by solitons. This positive quasiparticle will have an effective mass much less and a mobility much greater than hydronium in bulk water. In order to fix the parameters of the family of soliton solutions, macroscopic phenomenological data must be used to infer microscopic properties. A simple one-dimensional fluid model will be used to make an educated guess for the mobility of the positive solitons and also quantitatively demonstrate why leaders have a unique speed; it will also qualitatively explain why they have a fractal shape. In conclusion, it will be shown how these new ideas describe the breakdown phenomenology qualitatively, and future experiments will be suggested.

2.3.2 Metal Insulator Transitions

For a quasi-classical description to work, the concept of a mean free path must be applicable. In other words, the excess electron wave function must not lose phase coherence or decay over interatomic distances. It is very difficult to calculate these two lengths from first principles for a substance as complicated as liquid water, but one can make inferences from measurements and quantum simulations. P. Krebs has taken data that seems to indicate that the electronic wave function decays on a scale equal to interatomic distances.[19] He measured mobility as a function of number density of water molecules and found a precipitous drop in its value when the density approaches $10^{20}/cm^3$, which is about two orders of magnitude less dense than liquid water. The experimental data do not approach liquid densities, so it is possible that the mobility may start to increase at bulk water density. From this drop in mobility, it is claimed that the electron has become localized. Quantum simulations of excess electrons in water seem to further support the experiments, since the wave function for a single electron is spread over about 5 angstroms, which is about the distance between two oxygen atoms in water.[41] The simulations make predictions about the properties of hydrated electrons that match up well with experimental values. Both of the above studies indicate that quasi-classical concepts such as mean free path are not applicable, which demonstrates that electron avalanches forming through collisions in liquid water is not a credible concept.

A proper way of imagining water becoming a conductor for electrons uses quantum field theoretic techniques. A large number of condensed matter physicists have studied bulk metal insulator transitions, both theoretically and experimentally.[52–54] There is at present a classification system for all the different transitions that have been studied. There are basically four metal insulator transitions: Anderson, Mott, Peierls, and band-crossing. In order to understand them, it is useful to look at Fig. 2.1, which is a model energy band structure.

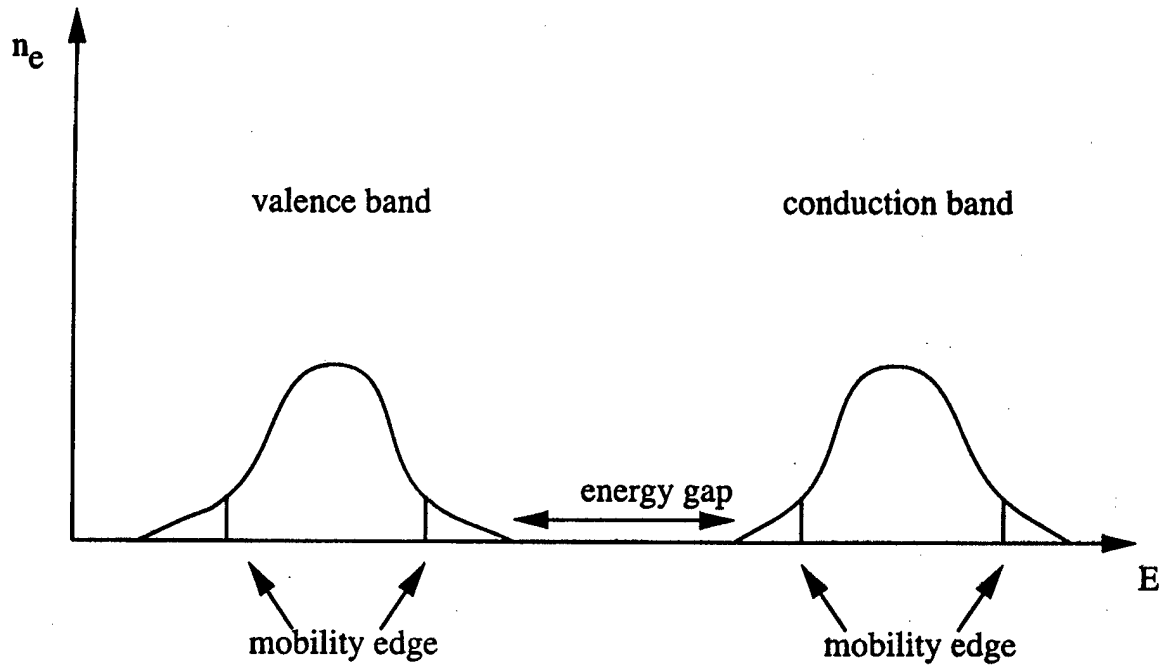

Figure 2.1
Model energy band structure.

AS-99-1

The figure shows that there is a valence and a conduction band separated by an energy gap. There may be certain special energies separating states within a band that have extended wave functions from those having localized wave functions; the ones inhabiting the tail of the model bands are the localized states. The energy separating these two kinds of wave functions is called the mobility edge because when a band energy is considered to be localized, there will be zero conductivity contribution from this part of the electronic spectrum. When a Fermi level crosses this mobility edge, this phenomenon is called an Anderson transition. It may be caused by moving the mobility edge by increasing or decreasing the disorder in the system or by moving the Fermi level by adding or subtracting donors (see Fig. 2.2). The band crossing transition is caused by changing the energy gap (see Fig. 2.3).

A possible way of causing the band crossing, and hence the required mobility increase, is by either increasing or decreasing the number density of the material. Both of the transitions mentioned above do not involve interacting electrons. The two remaining transitions rely heavily on electrons interacting with each other. The Mott transition is caused by electrons interacting through their spins; a common example is the addition of large quantities of metal alkali to liquid ammonia, which creates a liquid electronic conductor. The Peierls transition is produced by the interaction of the electrons through the ionic lattice.[55] The electrons reduce their energy through displacement of the ions and create an energy gap, producing an insulator. An example is shown in Fig. 2.4.

As already discussed in the literature survey, the energy band structure of water is seen to have a wide energy gap with the valence band fully populated while the conduction band is empty. The band edges are very sharp and do not appear to have any measurable Anderson localized states. It would seem that the only possible transition that the electrons could perform would be the band crossing mechanism through the lowering of the density of the water, which requires some type of energy input. Since dielectric breakdown can be initiated at an anode and excess electrons in water are nonexistent, it would seem that

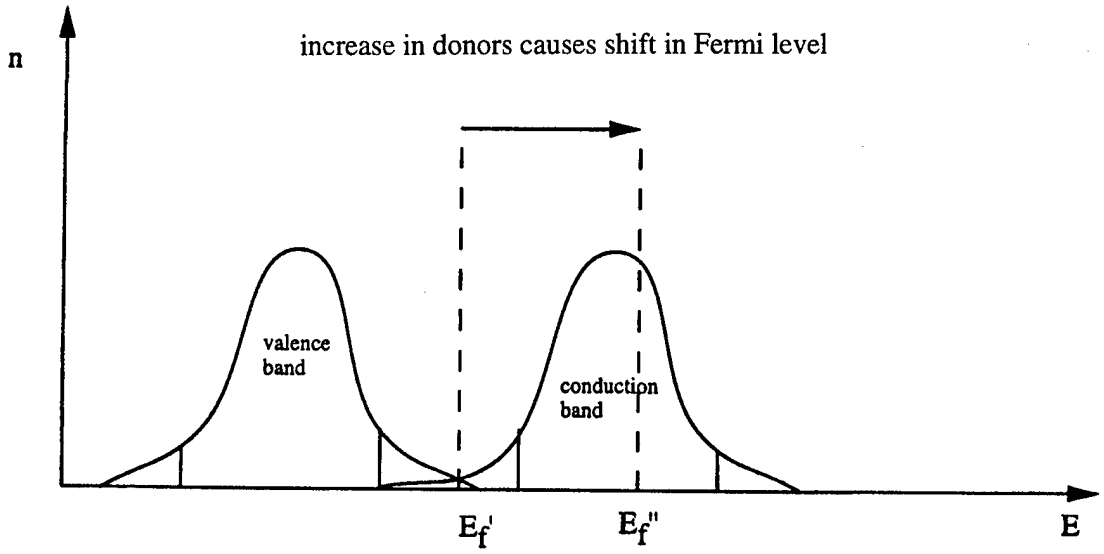

Figure 2.2
Anderson transition.

AS-99-2

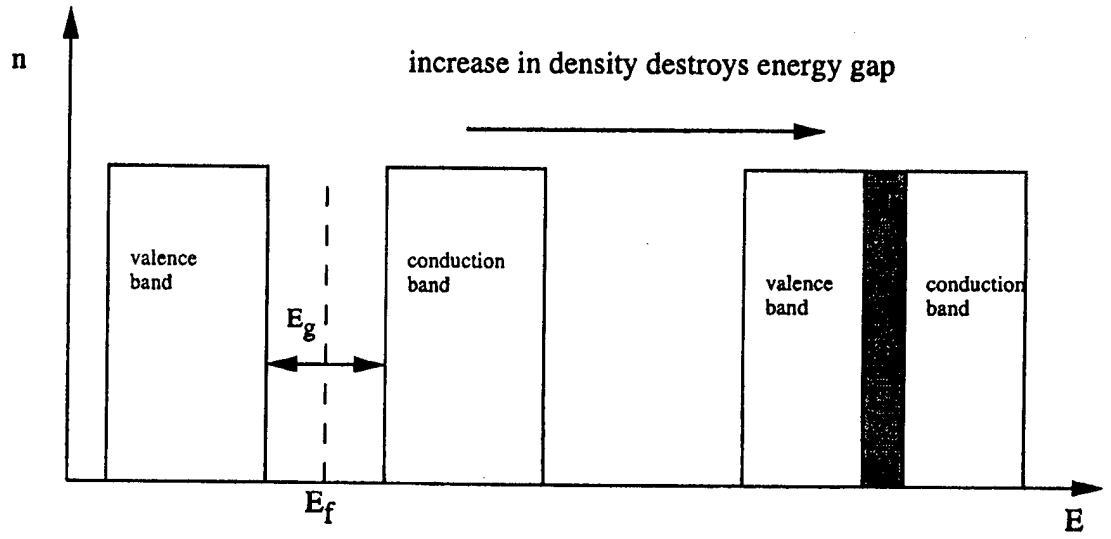

Figure 2.3
Band-crossing transition.

AS-99-3

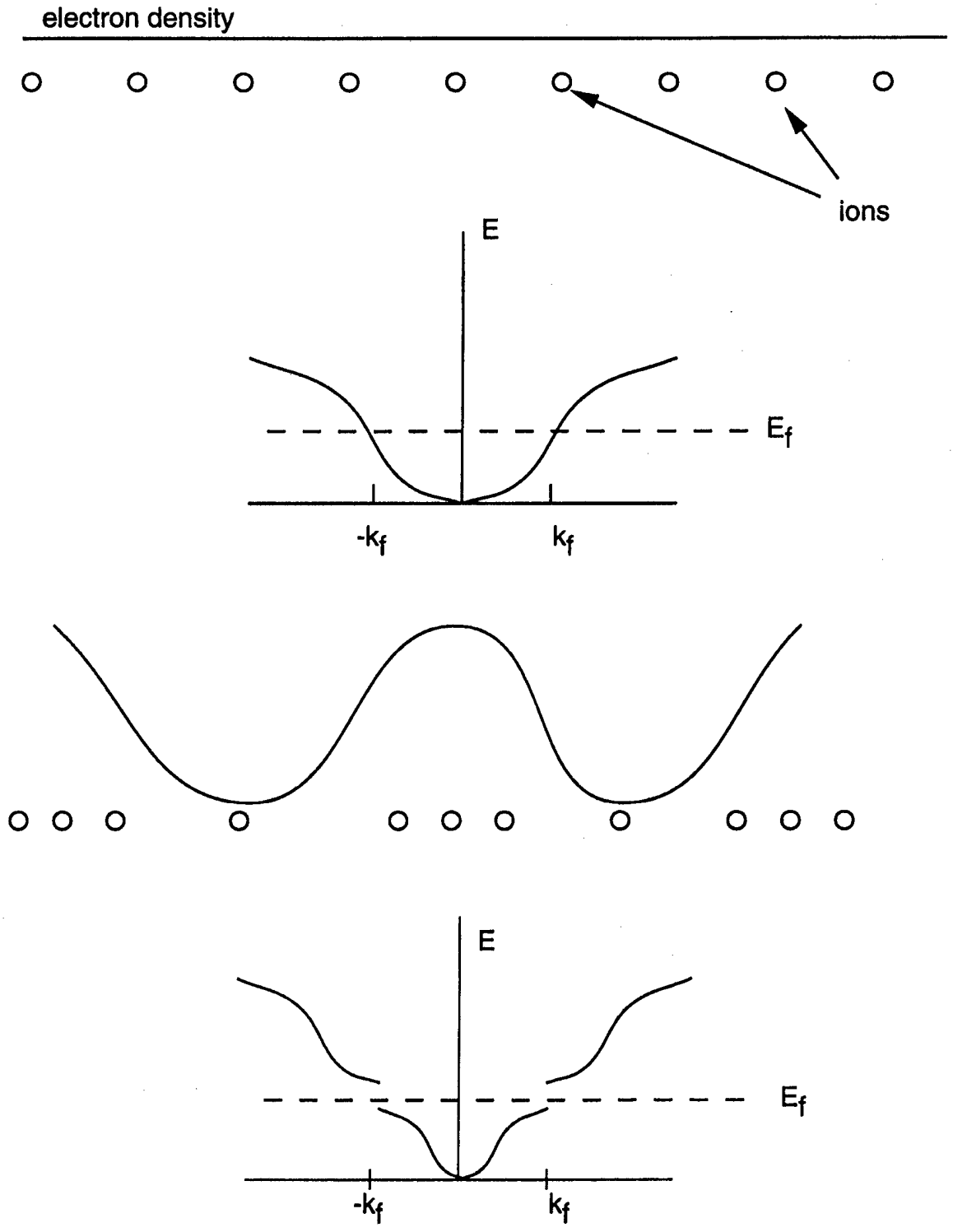

Figure 2.4

Peierls transition.

AS-99-4

the only electronic mechanism is the autoionization of individual molecules, but the electric field is too low for this to occur. In conclusion, electron avalanches produced by a band crossing transition are conceptually possible but prohibitively energy expensive.

2.3.3 Quasiparticle Transport

As already mentioned in the introduction, the standard theory of low dc field conduction in water is the Grotthus mechanism, which is represented in Fig. 2.5.[21]

Since experiments and simulations mentioned in the literature survey indicate that the water adjacent to the electrode becomes "solid-like," it proves to be useful to imagine the leader tip as having a similar structure, since the electric field will be the most intense here. The imagined structure of the leader tip is pictured in a one-dimensional model in Fig. 2.6.

Some previous investigators of conduction in ice have theorized that collective motion of protons can effectively lower the activation energy of charge transport; they have discovered that this motion can be represented by solitons, as depicted in Fig. 2.7.[48,56,57] Now we have a mechanism for charge transport with a mobility much higher than conduction in the bulk water. A brief outline of the calculations used to derive the properties of these solitons will be given.

The first assumption is that the oxygen atoms are frozen in a regular lattice. The protons lying between the oxygens interact with their nearest neighbor protons. A reasonable potential function is selected in order to simulate the background ion lattice. The Hamiltonian function for such a model is[57]

$$H = \sum_n \left[\frac{1}{2} m \left(\frac{dy_n}{dt} \right)^2 + \frac{1}{2} m \left(\frac{c_0}{l_0} \right)^2 (y_{n+1} - y_n)^2 + E_0 V \left(\frac{4\pi}{l_0} y_n \right) \right] , \quad (2.1)$$

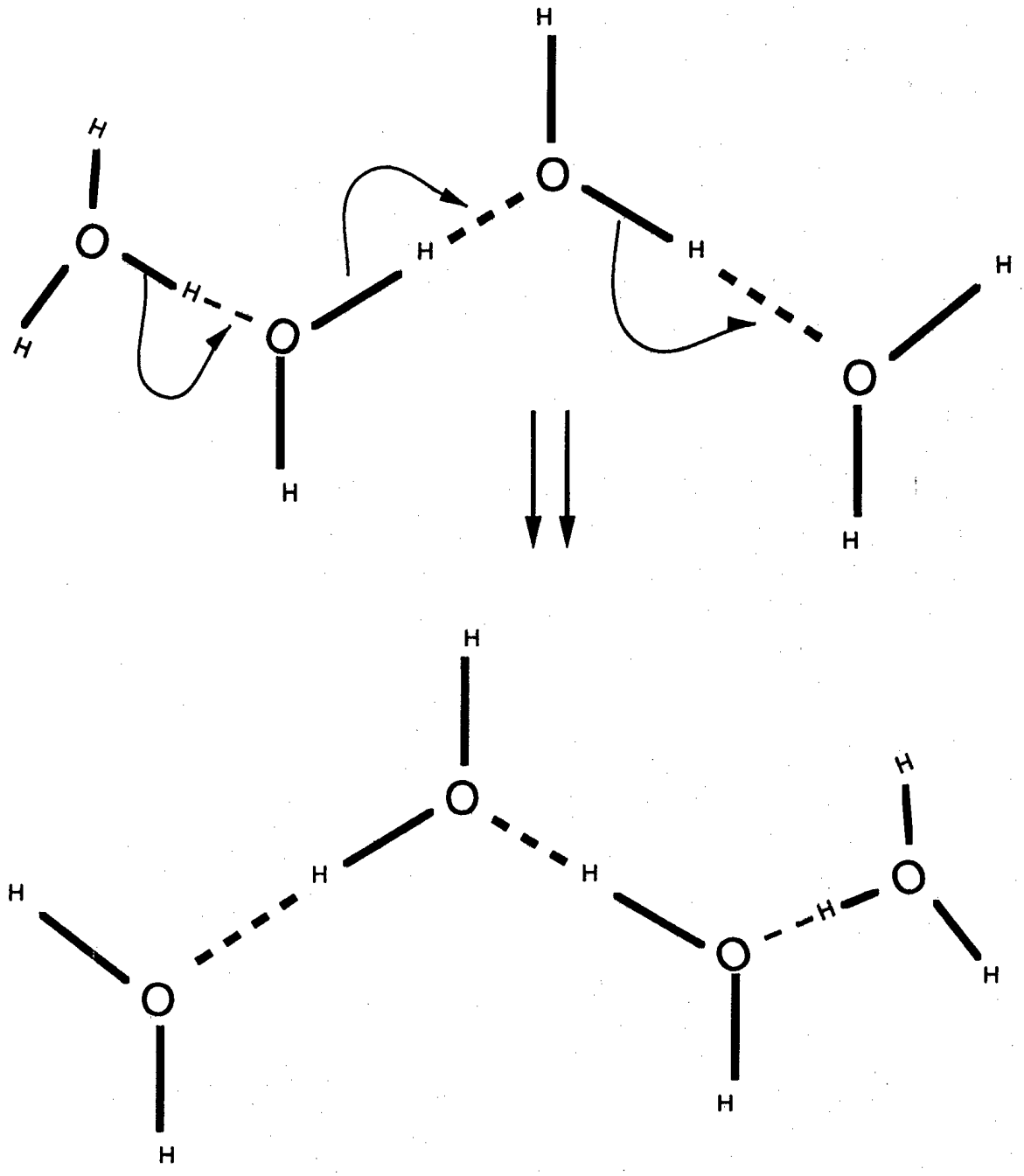

Figure 2.5
Grotthus' mechanism.

AS-99-5

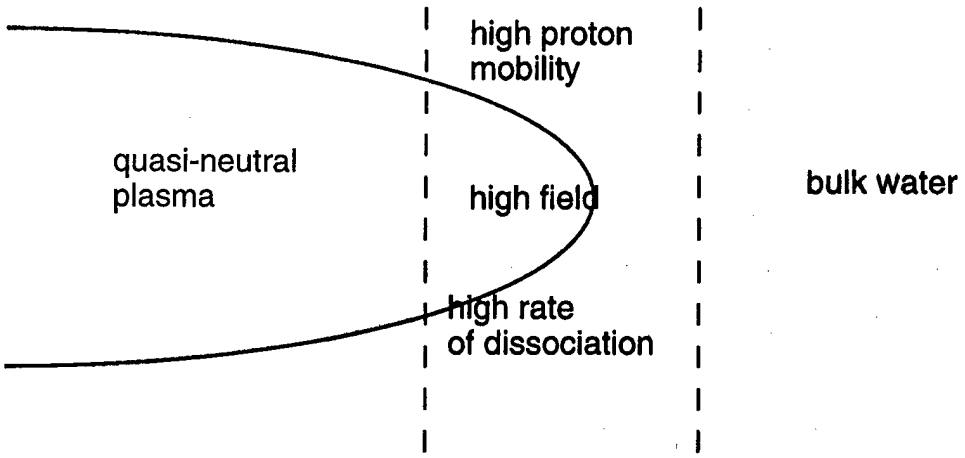

Figure 2.6

Leader structure.

AS-99-6

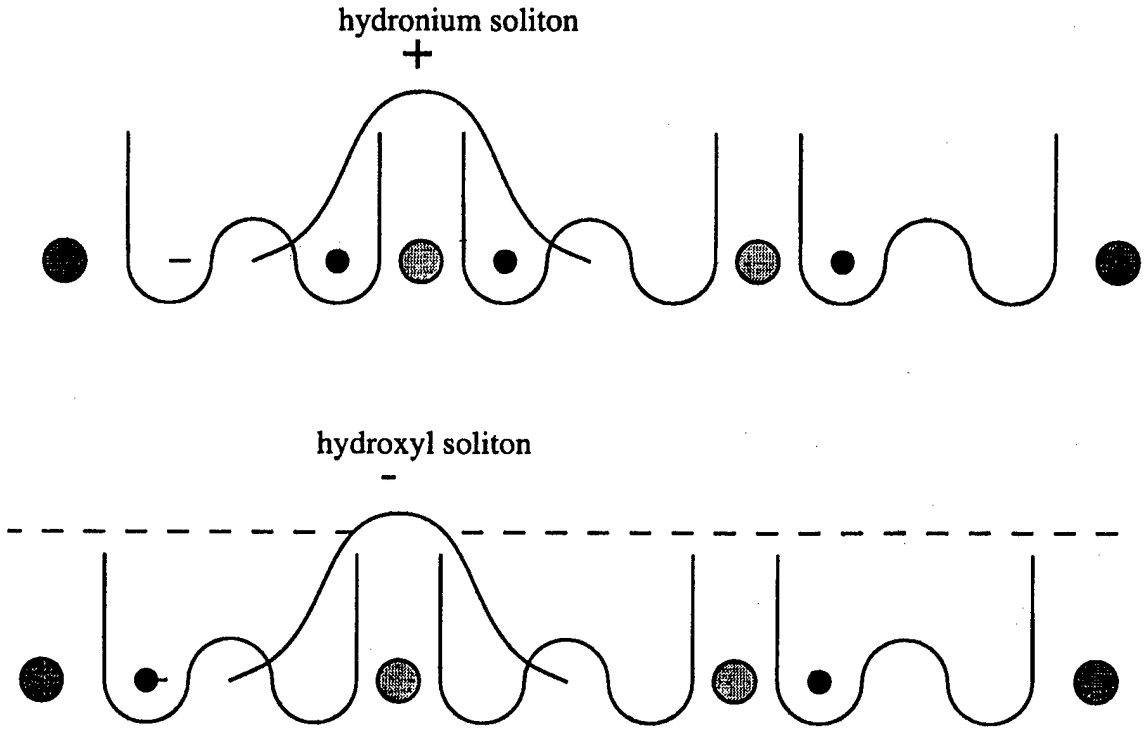

Figure 2.7

Hydronium and hydroxyl solitons.

AS-99-7

where

m is proton mass,

y_n is proton displacement measured from midpoint between oxygens,

l_o is fixed distance between oxygens,

c_O is speed of sound for protonic chain,

E_o is scaling energy for on-site potential,

$V(4\_y_n/1_0)$ is a doubly periodic potential.

From the Hamiltonian, it follows that the equations of motion are

$$\frac{d^2u_n}{d\tau^2} = \left(u_{n+1} - 2u_n + u_{n-1}\right) - \Omega_0^2 \frac{dV(u_n)}{du_n} \quad , \qquad (2.2)$$

where

n = 0, +1, +2, +3,...,

$u_n = 4\pi y_n/1_0$ is the dimensionless displacement,

$\Omega_o = \omega_0 t_0$ is a scaled frequency,

$\tau = t / t_)$ is a scaled time.

To arrive at analytic solutions for these systems of equations, one must assume the scaled frequency is in the displacive regime ($0 < \Omega_0 << 1$) and only consider long wavelength solutions, which is called the continuum limit approximation.[57,58] Having made these assumptions, one reduces the system of coupled equations to one partial differential equation,

$$u_{\tau\tau} - u_{xx} + \Omega_0^2 \frac{dV(u)}{du} = 0 \quad . \qquad (2.3)$$

Equation (2.3) can be solved for traveling wave solutions:

$$\frac{du_k}{ds} = \pm\gamma\Omega_o\left[2V(u_k)\right]^{1/2} , \qquad (2.4)$$

where

$s = x - vt$,

$y = (1-v^2)^{-1/2}$,

$v = v/c_0$,

$K = I^{\mp}B^{\mp}$.

u_k takes on values in two ranges:

$4\pi n - u_0 < u_I < 4\pi n - u_0$,

$4\pi n + u_0 < u_B < 4\pi(n+1) - u_0$,

$n = 0, \pm1, \pm2, \pm3, \ldots$.

The last step is now to select an analytic form for the doubly periodic potential:

$$V(u;\alpha,\beta) = \frac{2}{1-\alpha^2}\left(\frac{\varphi}{1-\beta\varphi}\right)^2 \qquad (2.5)$$

where

$$\varphi = \cos\left(u/2\right) - \alpha ,$$

$$\varphi = \cos\left(u_0/2\right),$$

$$u_o = 4\pi y_0 / l_0 ,$$

$\pm y_0$ are two equilibrium positions between oxygens,

α is parameter-fixing ratio of two heights.

The solutions to Eq. (2.4) are kink and antikink solitons. The general form is written as

$$s = \pm(\gamma Q_0)^{-1}\left[\ln(p_k) - \frac{1}{2}(1-\alpha^2)^{1/2}\beta q_k\right] . \qquad (2.6)$$

When k is

I^- →ionic defect→kink→negative polarity ,

I^+ →ionic defect→kink→positive polarity ,

then p_k , q_k are

$$P_I = \frac{R_0 + \tan(u_I/4)}{R_0 - \tan(u_I/4)} ,$$

$$q_I = u_I - 4\pi n ;$$

but when k is

B^- → bonding defect → antikink → negative polarity ,

B^+ → bonding defect → antikink → positive polarity ,

then p_k , q_k are

$$P_B = \frac{-R_0 + \tan(u_B/4)}{R_0 + \tan(u_B/4)} ,$$

$$q_B = -\left[u_B - 4\pi\left(n + \frac{1}{2}\right)\right] .$$

Various physical quantities can be calculated from the solution. Table 2.1 shows various sample quantities; following the table are the expressions for various parameters, listed in alphabetical order.

Table 2.1

Breakdown voltages.

Conductivity (mS/cm)	Capacitance (μF)	Breakdown Voltage (kV)
0.47	300	4.0
	600	4.0
	1200	3.0
	2350	2.0
5.60	300	3.5
	600	3.0
	1200	2.5
	2350	2.0
16.20	300	3.5
	600	2.5
	1200	2.0
	2350	1.8
28.00	300	3.5
	600	2.5
	1200	2.0
	2350	1.5
38.00	300	3.5
	600	2.5
	1200	2.0
	2350	1.5

A good check for internal consistency is that the width of the soliton must be bigger than the lattice spacing.

Soliton Charge

$$e_K = -\frac{ed_K}{4\pi}$$

where

$$d_K = \pm 2u_0 \rightarrow I^{\mp}$$

$$d_K = \pm(4\pi - 2u_0)$$

Soliton Energy

$$E_K(v) = \gamma E_K(0)$$

where

$$E_K(0) = 2^{3/2}\varepsilon_0\Omega_0 A_K$$

$$A_K(u) = \int_{\Lambda_K} du[V(u)]^{1/2}$$

where Λ_K is $[0,u_0]$ for $K = I^{\mp}$ or $[u_0,2\pi]$ for $K = B^{\mp}$

Soliton Mass

$$M_K = 2^{3/2}\Omega_0 A_K \varepsilon_0 / c_0$$

Soliton Mobility

$$\mu_K = 2^{3/2}\pi e l_0 R_K / mc_0 b\Omega_0 A_K$$

where

$$R_K = u_0 \text{ for } K = I^{\pm}$$

$$R_K = 2\pi - u_0 \text{ for } K = B^{\pm}$$

Soliton Width

$$W_K = \frac{R_K}{\gamma\Omega_0}\left(\frac{2}{V_K}\right)^{1/2} l_0$$

where

$$R_I = u_0$$

$$R_B = 2\pi - u_0$$

$$V_I = V(4\pi n)$$

$$V_B = V\left[4\pi\left(n+\frac{1}{2}\right)\right]$$

2.3.4 Macroscopic Fluid Description

Having a conceptual framework from which to calculate the mobility of the charge carriers in the leader, one next uses a macroscopic fluid description to infer the carriers' microscopic properties from dielectric breakdown experiments. To make the calculations manageable, one begins with two assumptions about the model. The leader is treated in only one dimension and is a perfect conductor. Only a brief overview is given here of the intermediate steps for an anodic leader. After all the calculations are finished, reasonable physical arguments are used to decide what happens when one relaxes the assumptions so that intelligent statements can be made about the real three-dimensional case.

The fluid approach adopted was first used by physicists trying to understand breakdown in gases.[59-62] The system of equations used consists of Maxwell's equations and charged fluid conservation equations.

$$\frac{\partial E}{\partial t} = 4\pi e n_+ u \quad , \tag{2.7}$$

$$\frac{\partial n_-}{\partial t} = S \quad , \tag{2.8}$$

$$\frac{\partial n_+}{\partial t} + \nabla \cdot (n_+ u) = S \quad , \tag{2.9}$$

$$u = \mu_+ E \quad , \tag{2.10}$$

$$\frac{\partial}{\partial t}\left(\frac{3}{2} n_+ T + \frac{1}{2} m_+ n_+ u^2\right) + \nabla \cdot \left(\frac{5}{2} n_+ T u + \frac{1}{2} m_+ n_+ u^2 u\right) + e n_+ E \bullet u = -V_{diss} S \quad . \tag{2.11}$$

where

n_+ and n_- are the number densities of the positive and negative quasiparticles,

S is the source term that includes dissociation and recombination,

m_+ is the mass of the positive quasiparticle,

u is the drift velocity of the positive quasiparticles,

m_+ is the mobility of the positive quasiparticles,

T is the temperature of the positive quasiparticles,

$Vdiss$ is the dissociation energy in the "ice-like" water,

E is the electric field.

Equation (2.7) is an equivalent expression for Poisson's equation (differentiated with respect to time), derived from Ampere's law. The next two equations express the conservation of positive and negative quasiparticles. Equation (2.11) expresses conservation of energy. The next step of simplification is to assume the quasiparticles are highly randomized and that their drift velocity is much less than their thermal speed; this assumption allows the reformulation of the conservation of momentum into Eq. (2.10). Compared with

n_+T, terms n_+uu , ∂ , and ∂t in Eq. (2.11) can be ignored. Inserting equations (2.7), (2.8), and (2.9) into (2.11) results in

$$\frac{\partial}{\partial t}\left[\left(\frac{3}{2}T+V_{diss}\right)n_+ +\frac{\left(E^2-E_1^2\right)}{8\pi}\right]+\nabla\cdot\left[\left(\frac{5}{2}T+V_{diss}\right)n_+u\right]=0 \quad , \quad (2.12)$$

where E_1 is the electric field upstream from the leader front; the electric field behind the wavefront is zero because of the perfect conductor hypothesis. It is assumed that the temperature and dissociation energy are constants.

With a little manipulation, Eq. (2.12) can be converted into

$$n_+ = \frac{-1}{\left(\frac{3}{2}T+V_{diss}\right)}\left[\frac{1}{8\pi}\left(E^2-E_1^2\right)+\frac{1}{4\pi e}\left(\frac{5}{2}T+V_{diss}\right)\nabla\cdot E\right] \quad . \quad (2.13)$$

This equation gives the number density of the quasiparticles as a function of the electric field. To get an expression for the electric field evolution, Eq. (2.10) is inserted into Eq. (2.7), resulting in:

$$\frac{\partial E}{\partial t}=\mu_+ n_+ E \quad . \quad (2.14)$$

The result is two coupled equations that can be solved for traveling waves. The first step in solving the equations is to assume a steady state and then perform a perturbation analysis to decide which waves are stable. From this analysis, one finds a restriction on the velocity of the leader:

$$V \equiv \left[1+\left(T/V_{diss}\right)\right]\mu_+ E_1 \quad . \quad (2.15)$$

This demonstrates that the velocity, V, of the model leader has one unique velocity and has linear dependence on the electric field and the impurity concentration.

The most important assumption in the model is that the leader is a perfect conductor. This hypothesis is physically appealing because all photographic evidence of dielectric breakdown show an arc instantaneously forming when a leader touches the opposite electrode; there is no return stroke in water as in some gas breakdowns. In this model, seeding would seem to have no effect on the rate of branching by a leader. In order for seeding to play a role, the perfect conductivity assumption must be weakened. The mathematics of such an approach would be entirely nonanalytic and would be numerically intensive, so a qualitative description will be given.

Implicit in the one-dimensional fluid model is the assumption that the leader tip maintains a fixed amount of accumulated charge, or that the fluid model is incompressible. Seeding adds to the tip excess charge, which can be discharged instantaneously into the electrode since the leader body is a perfect conductor; the amount of tip charge can be maintained regardless of the seeding. By weakening the perfect conductivity assumption, the impurities add excess charge to the tip that it lacks the ability to discharge. In three dimensions, a leader has an option in forestalling this charge accumulation; it can split into two leaders, dividing up the excess charge. A possible way of incorporating this idea is to use the fractal idea used by Pietronero et al.[63] Other researchers at ARL:UT used this fractal idea to develop a technique of acquiring quantitative information about the rate of branching from oscillograms.[64] Meshing the one-dimensional fluid model with the fractal concept will be the objective of future work.

The formulated picture of a leader describes how experimental parameters such as electric field, impurity concentration, and polarity affect the dielectric breakdown of water. A quantitative method has been developed for estimating the mobility of the charge carriers in the leader and a qualitative explanation for

the branching of leaders. A future dielectric breakdown experiment with heavy water, which has the identical electronic structure as light water, could test this hypothesis.

2.4 EXPERIMENTAL

2.4.1 Overview

The experiments conducted at ARL:UT were not an attempt to acquire microscopic data. The voltages and breakdown times used for the PSS are sufficiently different from those used in the literature on dielectric failure of water that it was unclear if any connection existed between the literature and the regime in which spark sources operate. At first glance, it seemed that the breakdown times were sufficiently long that a thermal process would be able to explain the phenomenon. A phenomenological set of data was collected using a PSS electrode called the "wide gap coaxial" (WGC) and a point-to-ring corona electrode. These experiments, combined with photographs, clearly show that PSS is operating in a mixed regime of leader growth and ionic heating. The empirical evidence and the photographs indicate that the breakdown is through a leader growing into liquid water and not through the formation of a gas bridge between the electrodes. The thermal processes divert energy away from the arc formation and are, therefore, important from an efficiency standpoint but are not the cause of dielectric breakdown.

The order in which the data will be discussed is not the chronological order in which the experiments were conducted. The experiments can be roughly divided into two different groups: empirical and photographic. Empirical experiments consisted of collecting large quantities of electrical waveforms for identical experimental parameters and then, after altering a single parameter, repeating the process. These empirical tests shed light on the effects of salinity, pressure, and circuit capacitance for the PSS regime. Photographs were taken of the WGC and of the point-to-ring electrode. They clearly show that a

nonbubble process is the cause of electrical discharges in water. For each series of data, a brief description of the experimental setup will be given, followed by example waveforms, concatenated statistics graphs, and a short discussion of the physical insight given by the data.

2.4.2 Water Tank Experimental Setup

The first set of data to be discussed was taken in a cylindrical concrete pool whose bottom consisted of earth. The dimensions of the pool were 12 ft in diameter and 3 ft deep. In order to keep the water clean, several layers of pool liners covered the inside of the pool. To avoid puncture by the underwater explosions, two layers of 2-in.-thick ethafoam were placed between the bottom of the pool and the liners in an attempt to absorb the shocks. A March AC-SC-Md pump circulated the water, and debris were collected by a Hayward inline basket filter, which was cleaned out periodically. The pump had the capacity to circulate the entire volume of the pool in an hour, which gave the pump a circulation rate of about 600 gallons per hour. To keep debris in the water to a minimum, a pool cover was constructed and placed over the water, even during underwater discharges. The fresh water was straight from an ARL:UT city tap line.

Conductivity was measured using a model CDCN-36 controller from Omega and a conductivity electrode model CDCN-36-EG from the same company. The controller had four different conductivity range settings; the error in the readings was ±10% of the maximum value of the selected range. The electrode was calibrated with commercial standardized solutions. The tap water was found to have a conductivity of 400 μS/cm. The salinity of the water was changed by mixing in rock salt. To ensure complete dissolution, a wire meshed container holding the rock salt was connected to the output side of the rotary pump, not allowing any large pieces of undissolved salt to enter the pool. To ensure the saline solution remained homogeneous, the omega electrode was placed at different depths and positions. Four different mixtures were compared to check conductivity differences: rock salt in tap water, rock salt in distilled

water, reagent NaCl in tap water, and reagent NaCl in distilled water. All four solutions were found to be electrically identical.

The electrical setup consisted of a high voltage power supply, a high voltage capacitor bank, 29 ft of RG-220 coaxial cable, and a WGC electrode. A schematic showing the relation of this setup with the pool is shown in Fig. 2.8.

The power supply was capable of charging up to 10 kV. The capacitor hut consisted of banks of 50 μF capacitors connected in parallel, each rated up to 20 kV. The largest bank consisted of 12 capacitors connected in parallel. Multiple banks could be connected in parallel by connecting their coaxial cables to a bus bar. This bus bar was connected to a liquid-mercury-filled switch called an ignitron. The 29 ft section of RG-220 attached to the WGC electrode was then connected to the bus bar to which the base of the ignitron was connected. Figure 2.9 is a schematic representing the inside of the capacitor hut.

Two Pearson current sensors were used to measure the current passing through the RG-220 and through a 10-kΩ precision high voltage resister that was connected in parallel to the WGC electrode. The cable connecting the capacitor bank and the electrode was only 29 ft. The LC discharge time constant of the capacitor bank was much smaller than the prebreakdown times measured. Therefore, the voltage in the hut could be assumed to be the same as the voltage at the load during the prebreakdown phase up to the instant of breakdown.

The coaxial cables from the Pearson current monitors were fed into the instrument hut and connected to a lightning arrestor box in order to safeguard the Nicolet model 4570 oscilloscope from any stray power surges and to increase the safety of the operator. The bnc cables connecting the lightning arrestor with the oscilloscope were wrapped around at least one ferrite coil as an attempt to reduce the electrical noise. The data was saved on 5-1/4-in. diskettes. A trigger circuit inside the capacitor hut was initiated by a square wave pulse from a function generator inside the operator hut.

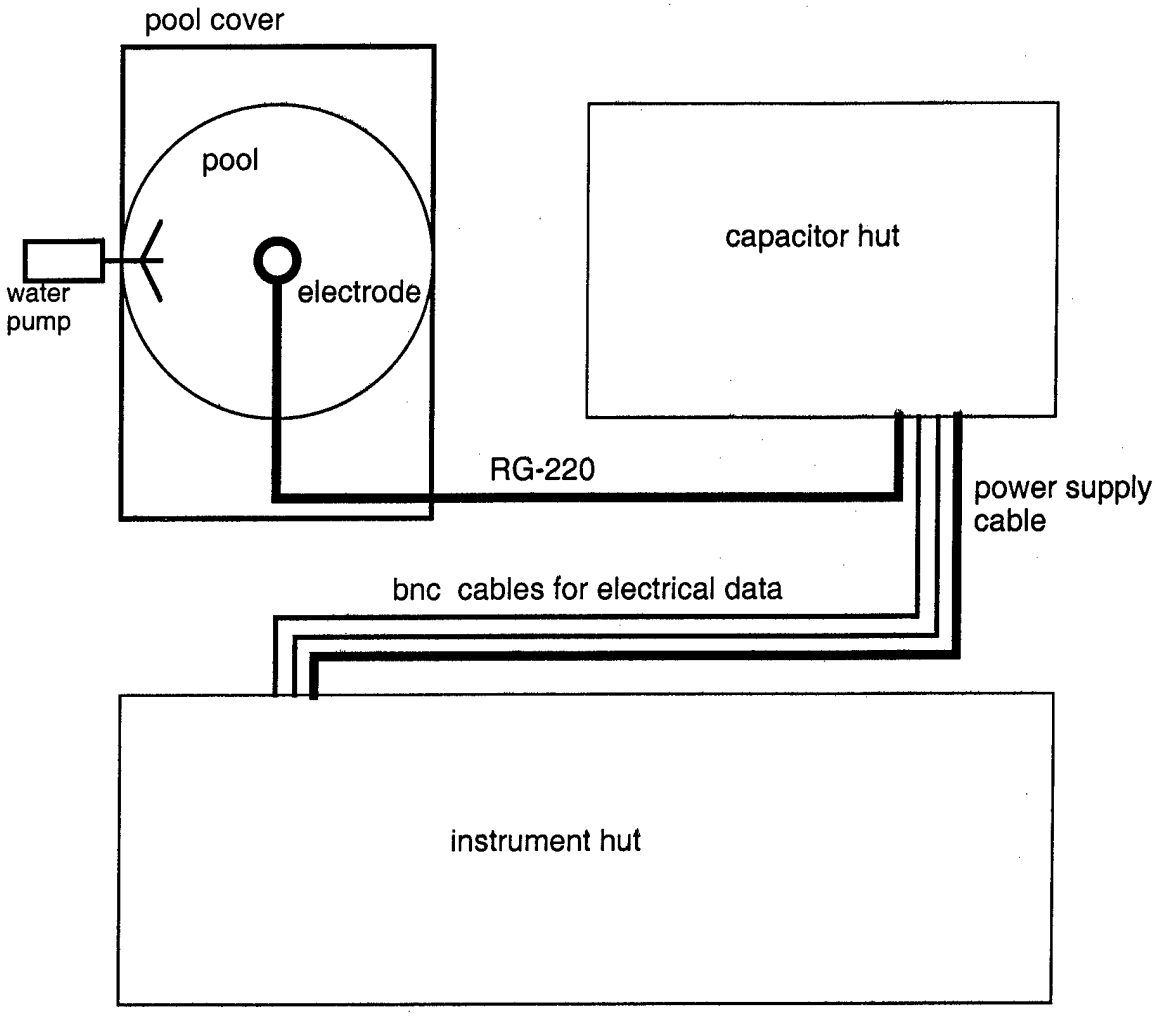

Figure 2.8

Experimental setup.

AS-99-8

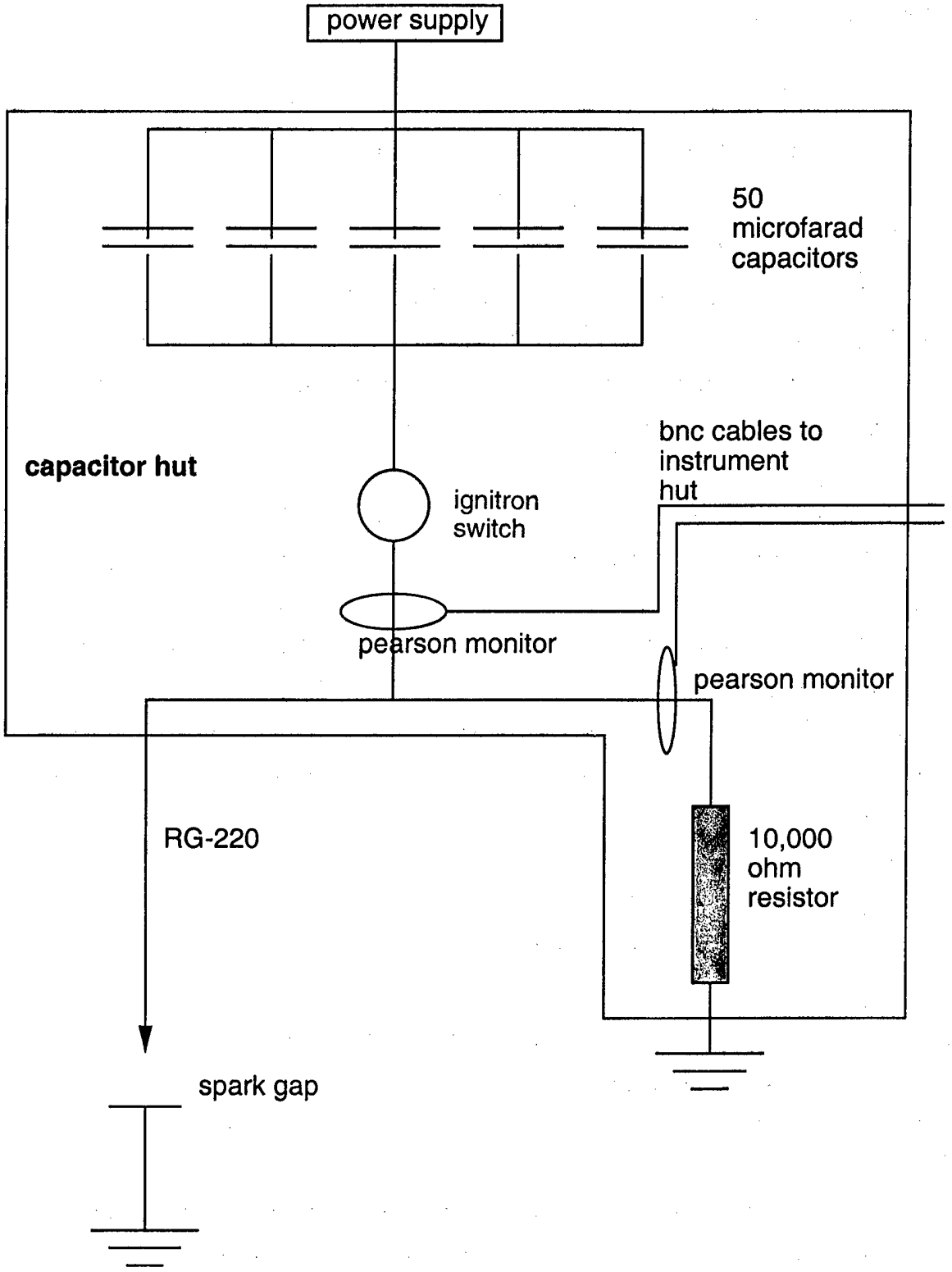

Figure 2.9

Capacitor bank.

AS-99-9

2.4.3 Water Tank Data

The set of parameters that were varied were voltage, capacitance, and the salinity. The voltages were varied from 1 to 10 kV with 1 kV increments. The capacitance values were 300, 600, 1200, and 2350 μF. The conductivity of the pool was set at 0.47, 5.6, 16.2, 28, and 38 mS/cm. The breakdown voltages for the different configurations are displayed in Table 2.1. A series of sample oscillograms are shown in Figs. 2.10 through 2.19. Breakdown occurs where both the current and voltage waveforms have a discontinuity in their first derivatives; otherwise, the discharge is a corona.

The results displayed in the figures and in Table 2.1 suggest that ionic heating may be an important process in limiting dielectric breakdown. As the capacitance is increased, the breakdown voltage is lowered; this result can be explained by the fact that ohmic heating of the bulk water between the anode and the cathode increases with voltage and is diverting the energy from the leaders. The larger capacitances give the circuit a larger RC time constant. The next experiment to be described was designed to demonstrate whether leaders or ionic heating precede breakdown by conducting discharges at different depths in the Gulf of Mexico.

2.4.4 Gulf of Mexico Experimental Setup

The experimental setup was very similar to the salt tank experiments. The electrode used was the WGC. The capacitor bank was replaced by a Marx bank, capable of erecting to 50 kV. Both the data collection instruments and the Marx bank were housed in the same hut, but they were separated by a wall which served to protect the operators and electrostatically shield the electronics. The coaxial cable connecting the electrode with the Marx bank was 1000 ft of RG-220 and was wound around a winch. The hydrophone used was a model TR-225.

Note: the voltage going negative is due to the ringing of the circuit.

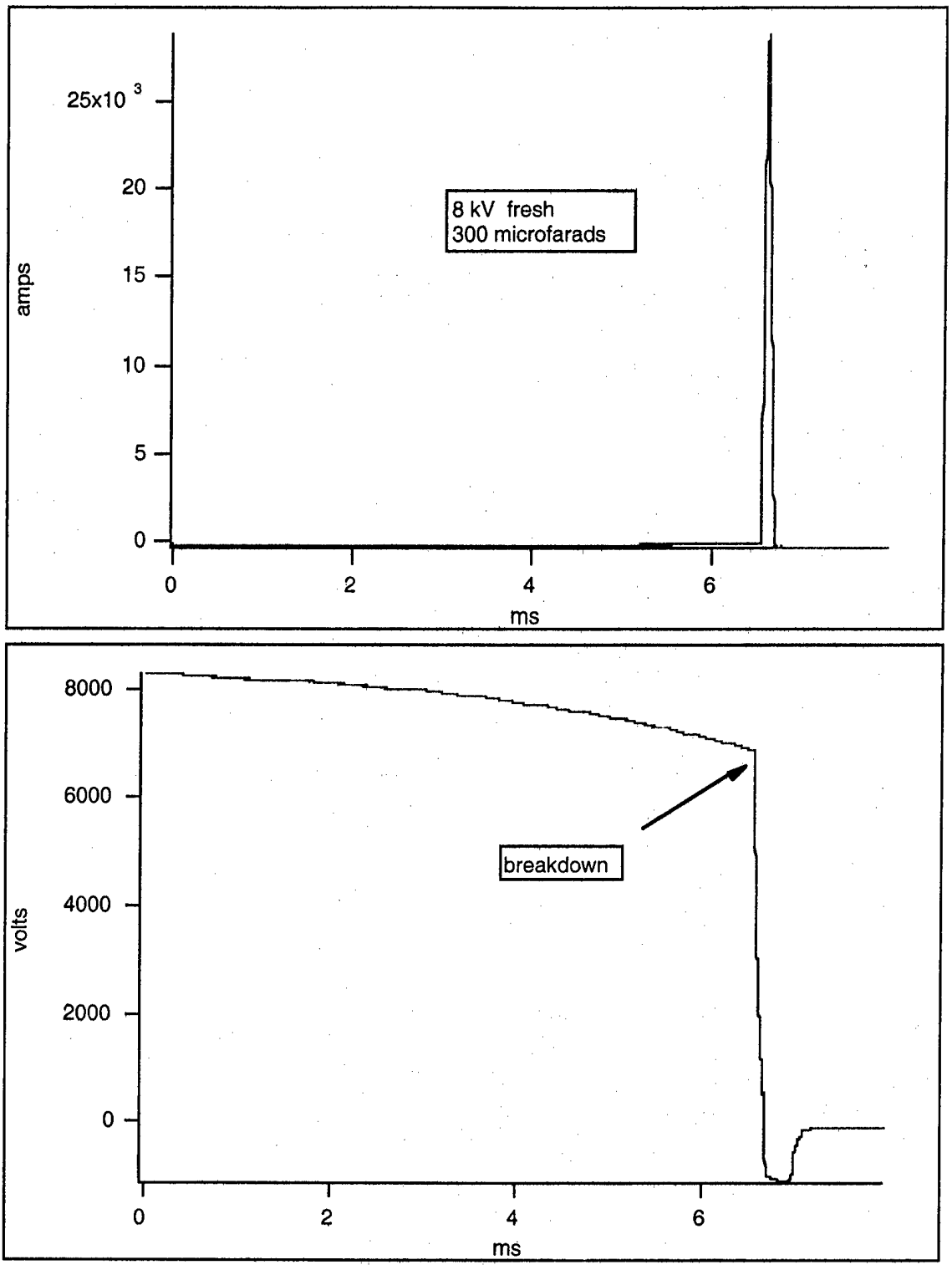

Figure 2.10

Voltage and current.

AS-99-10

Note: this figure depicts voltage and current at the breakdown threshold.

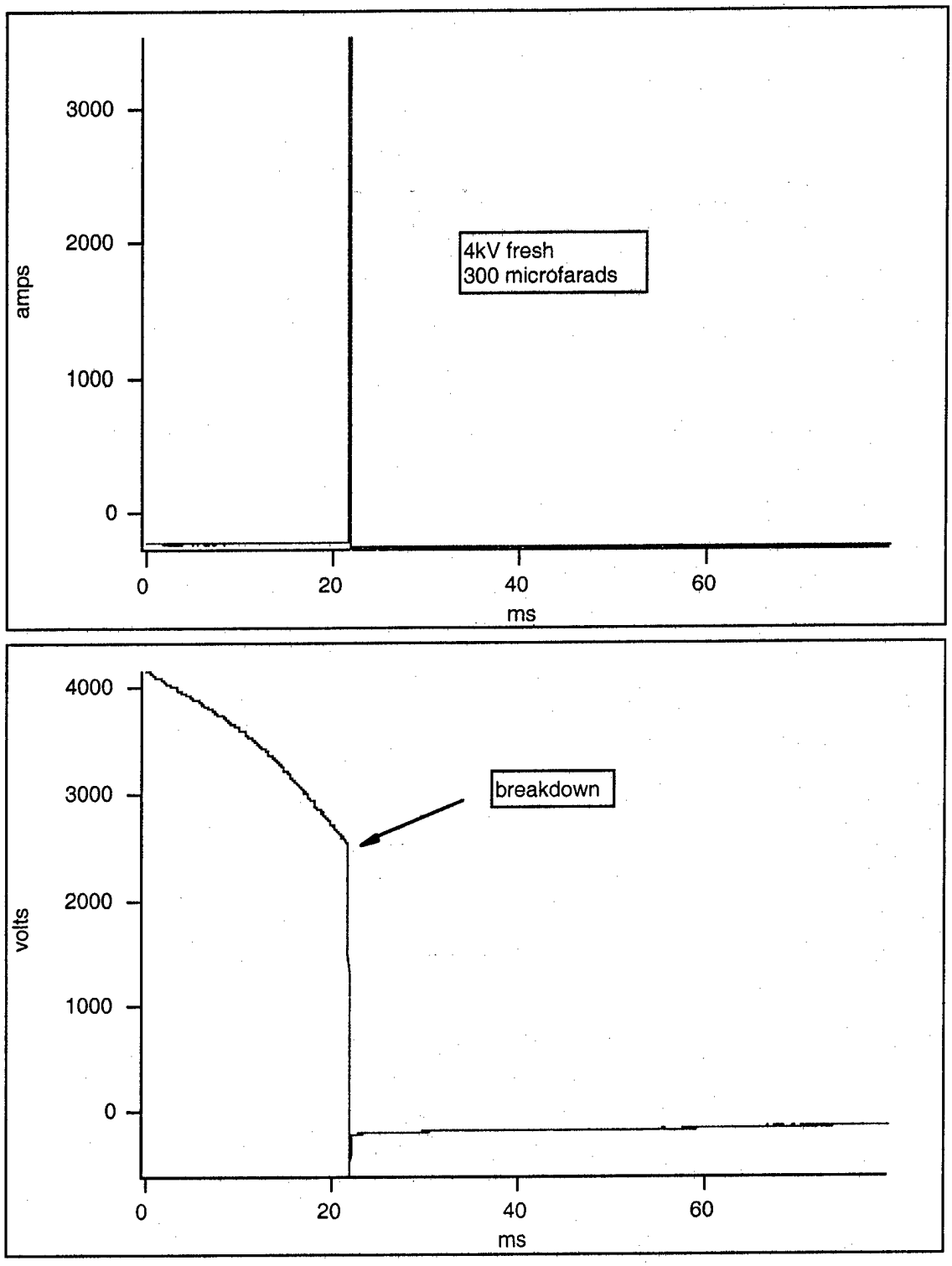

Figure 2.11

Voltage and current.

AS-99-11

Note: current flow is sufficiently small that noise picked up by Pearson current monitor begins to overwhelm signal.

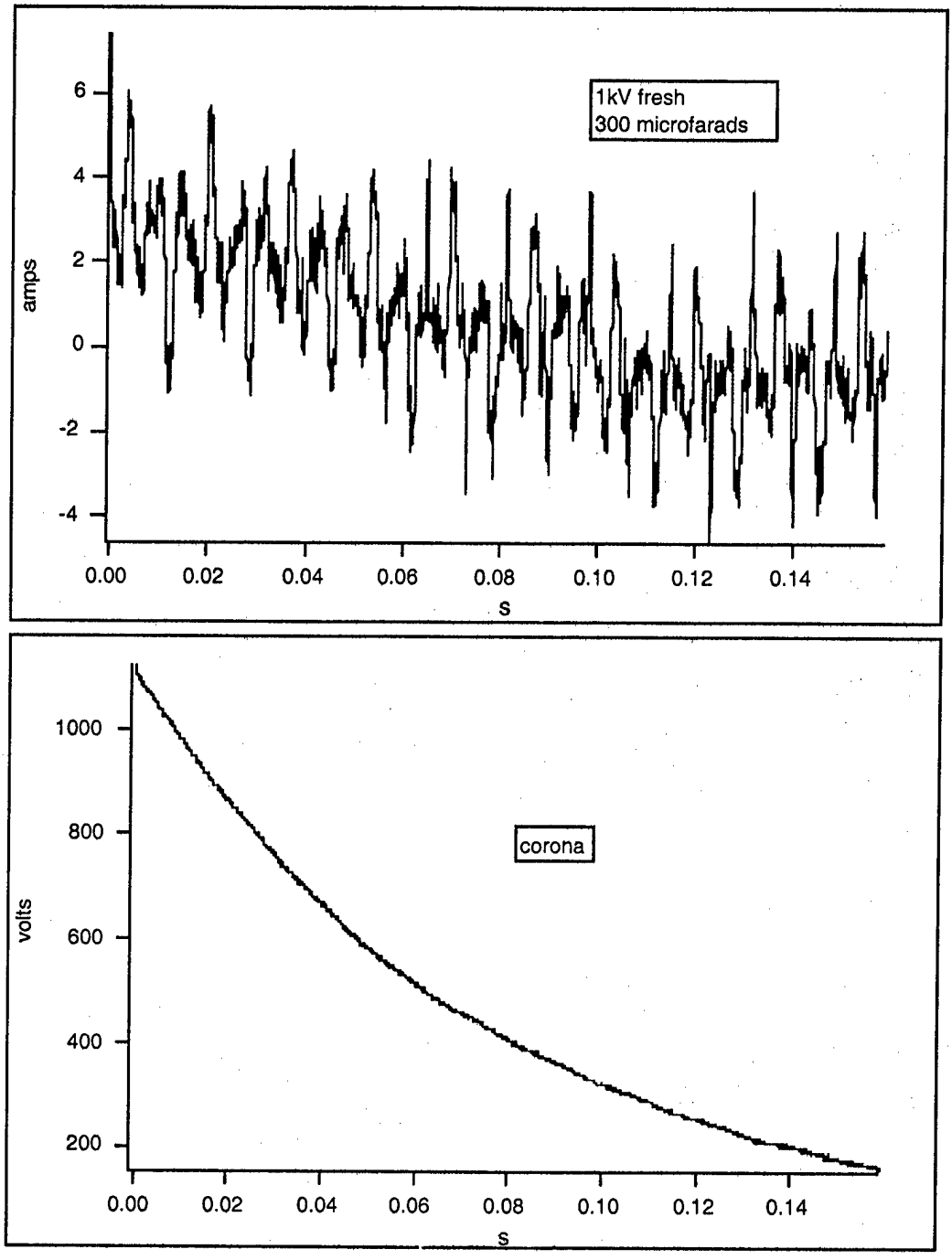

Figure 2.12

Voltage and current.

AS-99-12

Note: current signal cutoff due to oscilloscope settings.

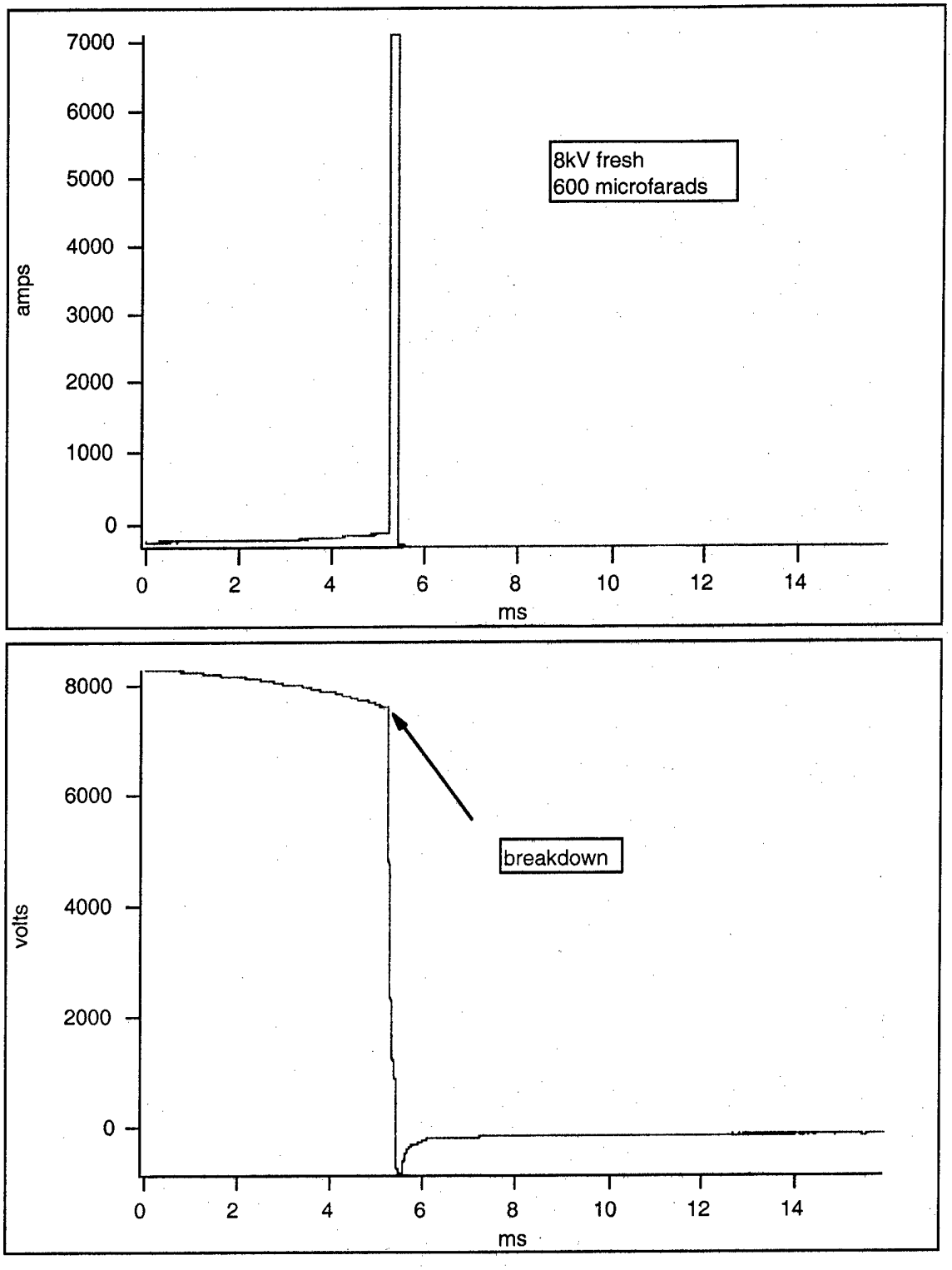

Figure 2.13

Voltage and current.

AS-99-13

Note: about 25% of 20-shot series displayed double breakdown.

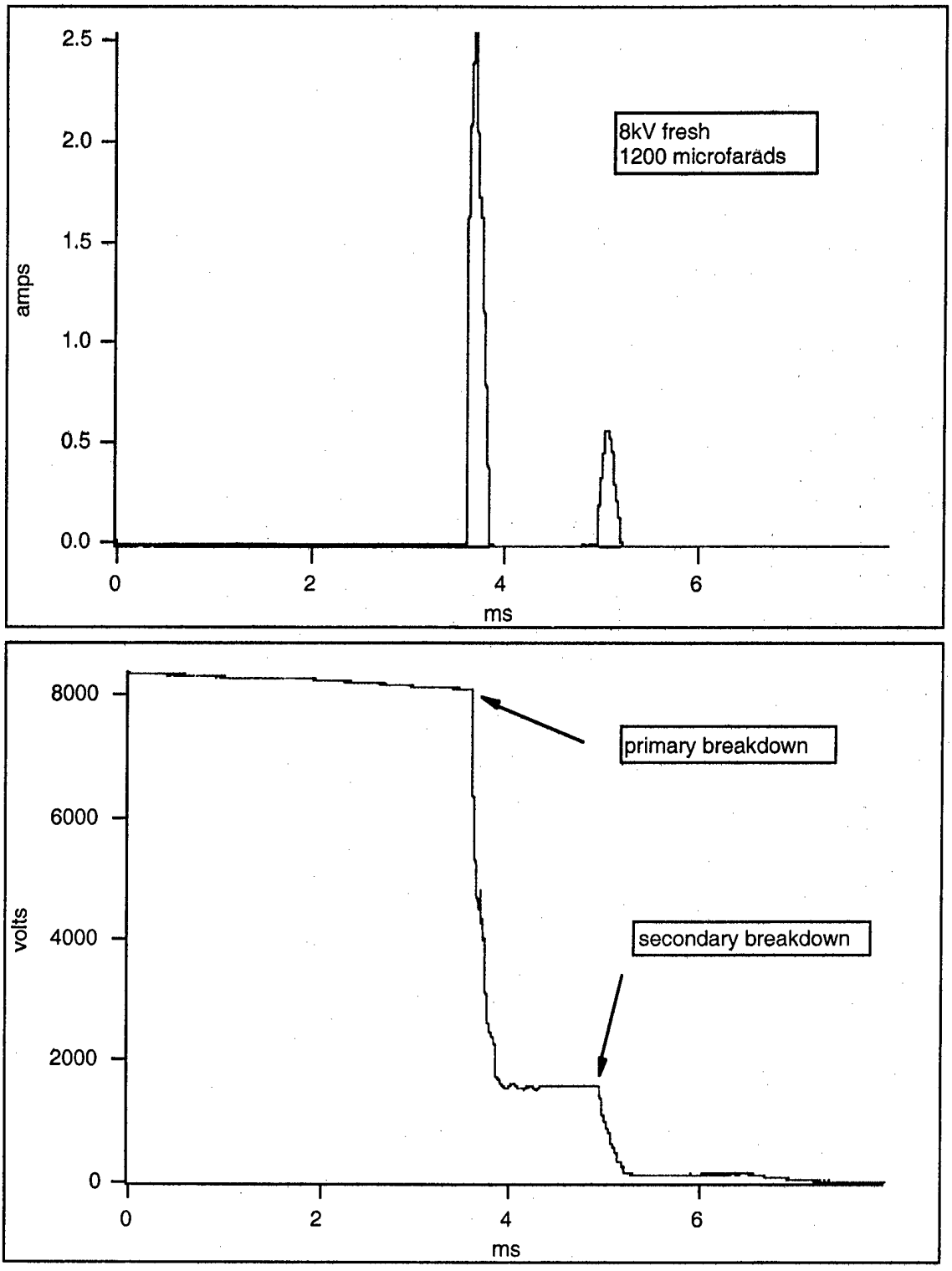

Figure 2.14

Voltage and current.

AS-99-14

Note: compare to Fig. 2.12. Since the conductivity is an order of magnitude higher, the current signal is stronger than the noise.

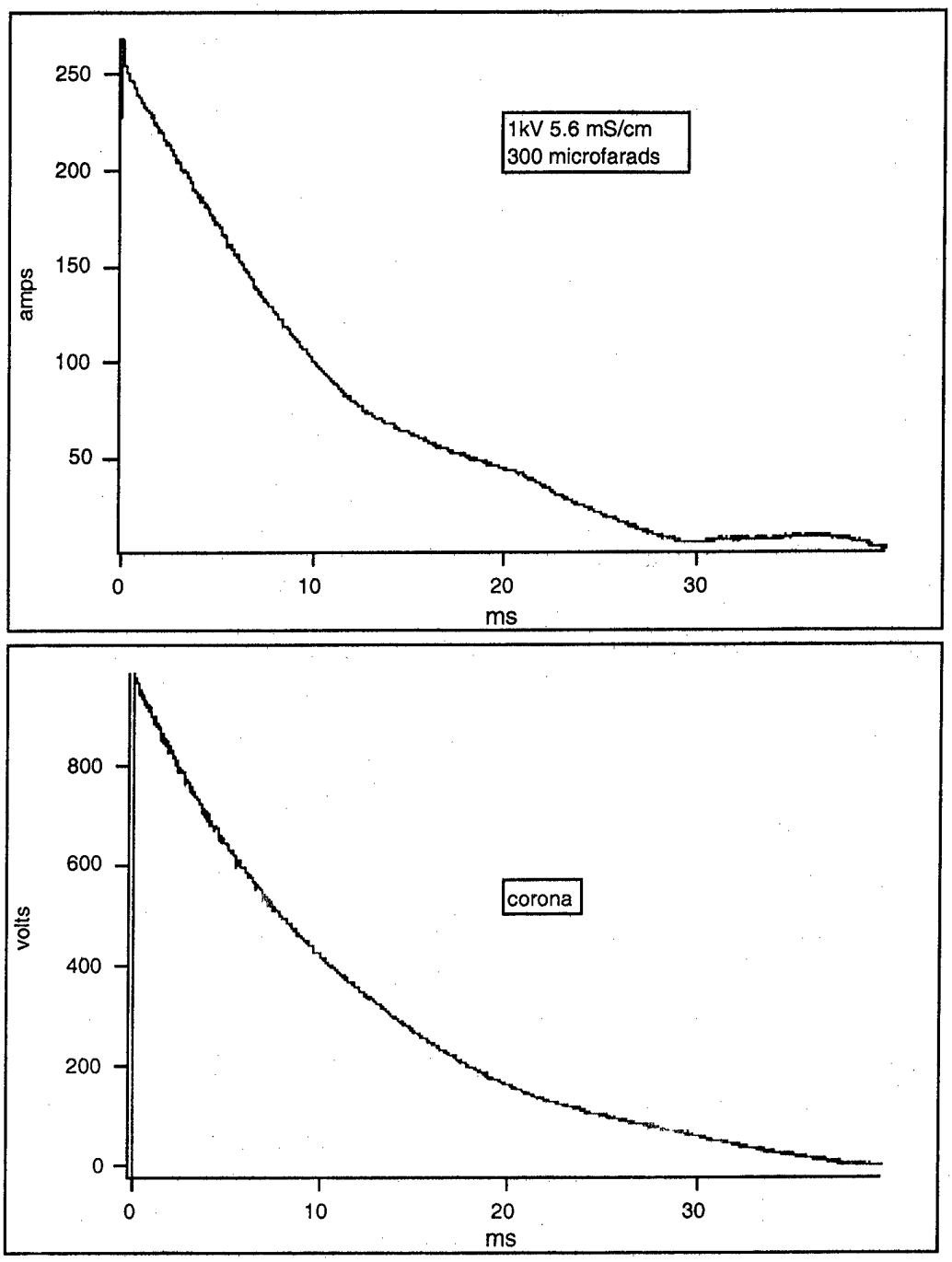

Figure 2.15
Voltage and current.

AS-99-15

Note: this figure depicts the voltage and current for a discharge at the breakdown threshold.

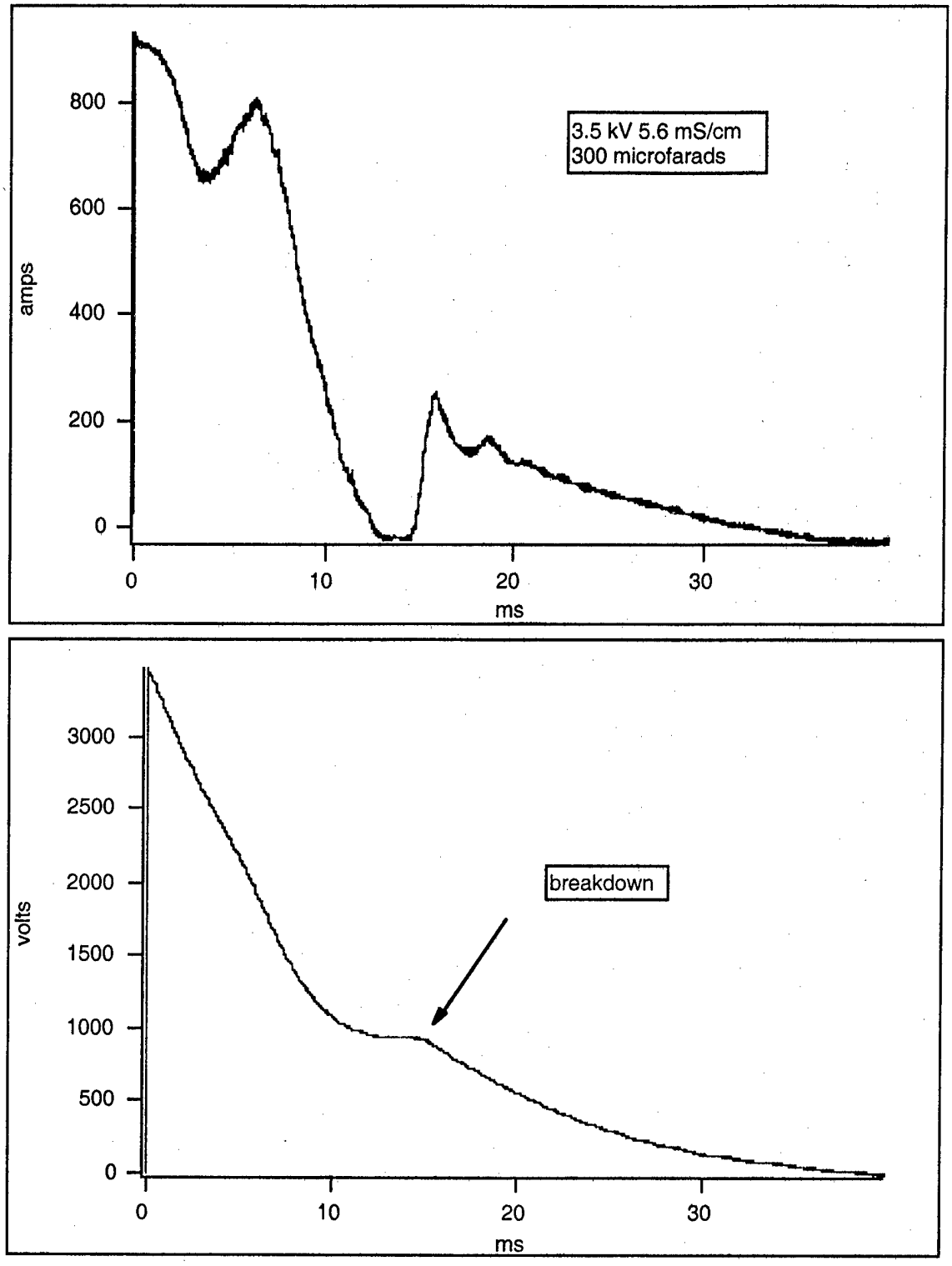

Figure 2.16

Voltage and current.

AS-99-16

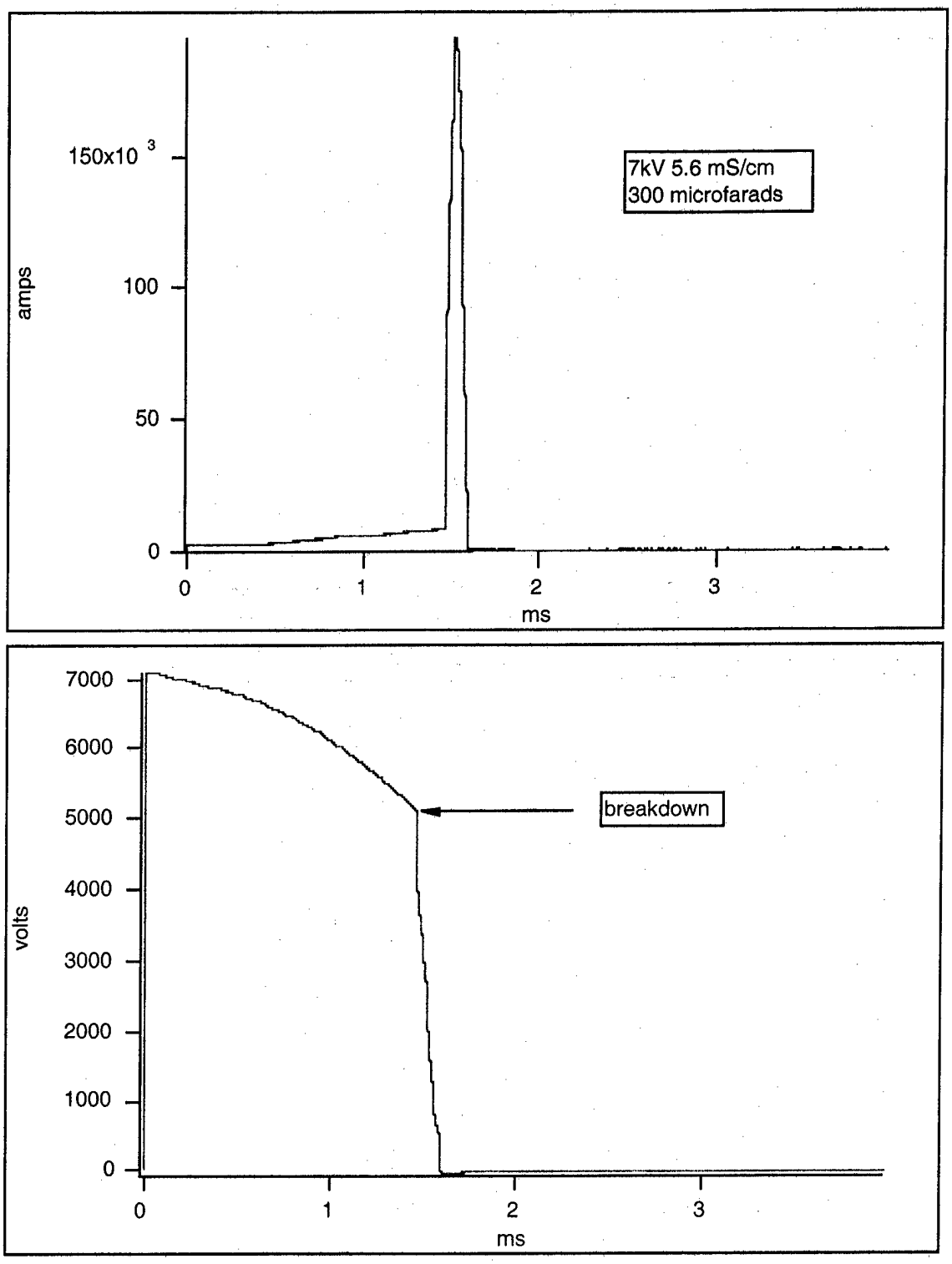

Figure 2.17

Voltage and current.

AS-99-17

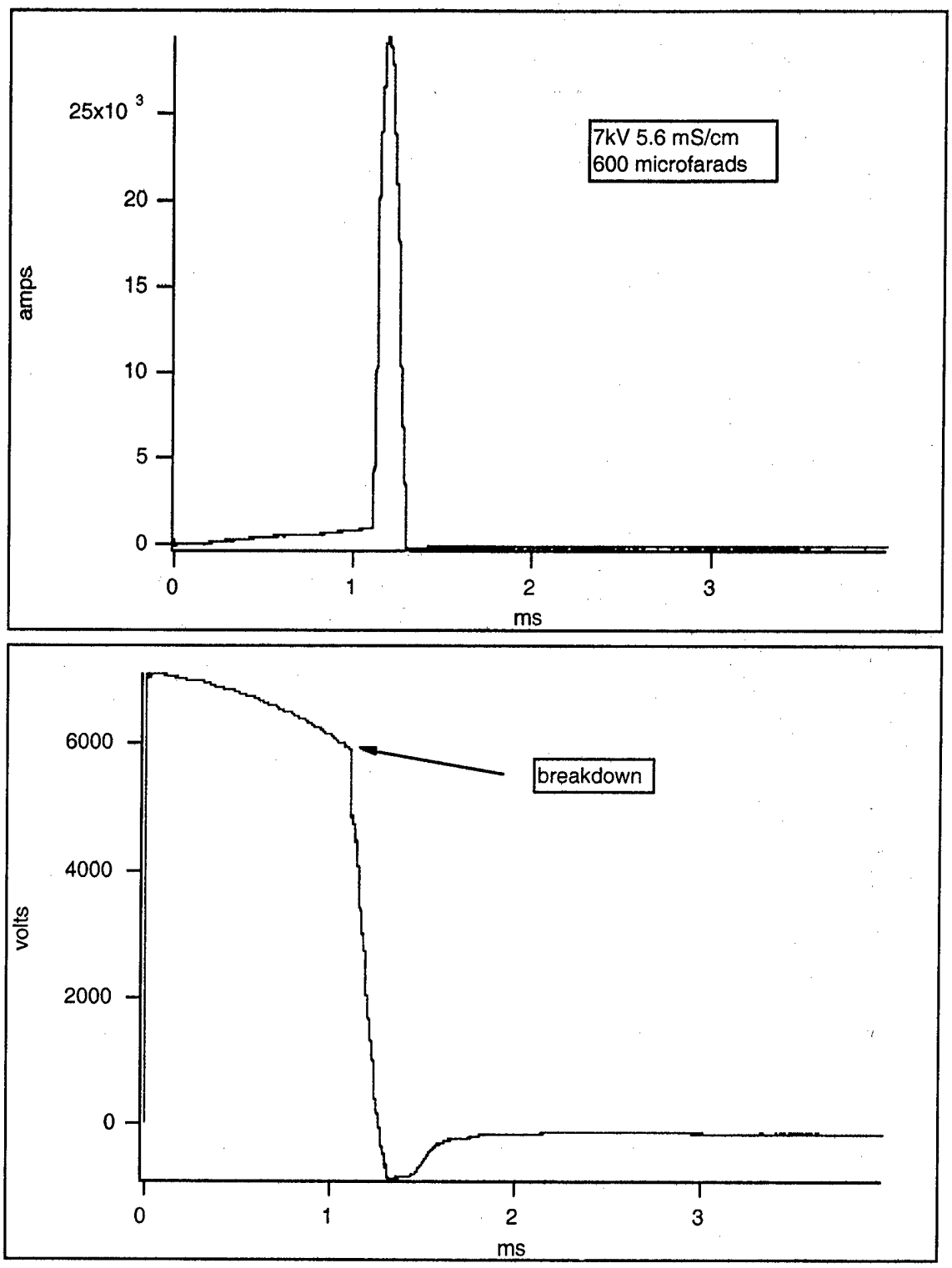

Figure 2.18

Voltage and current.

AS-99-18

Note: compare to Fig. 2.14. The difference in the rate of decay of the voltage is due to large differences in conductivity.

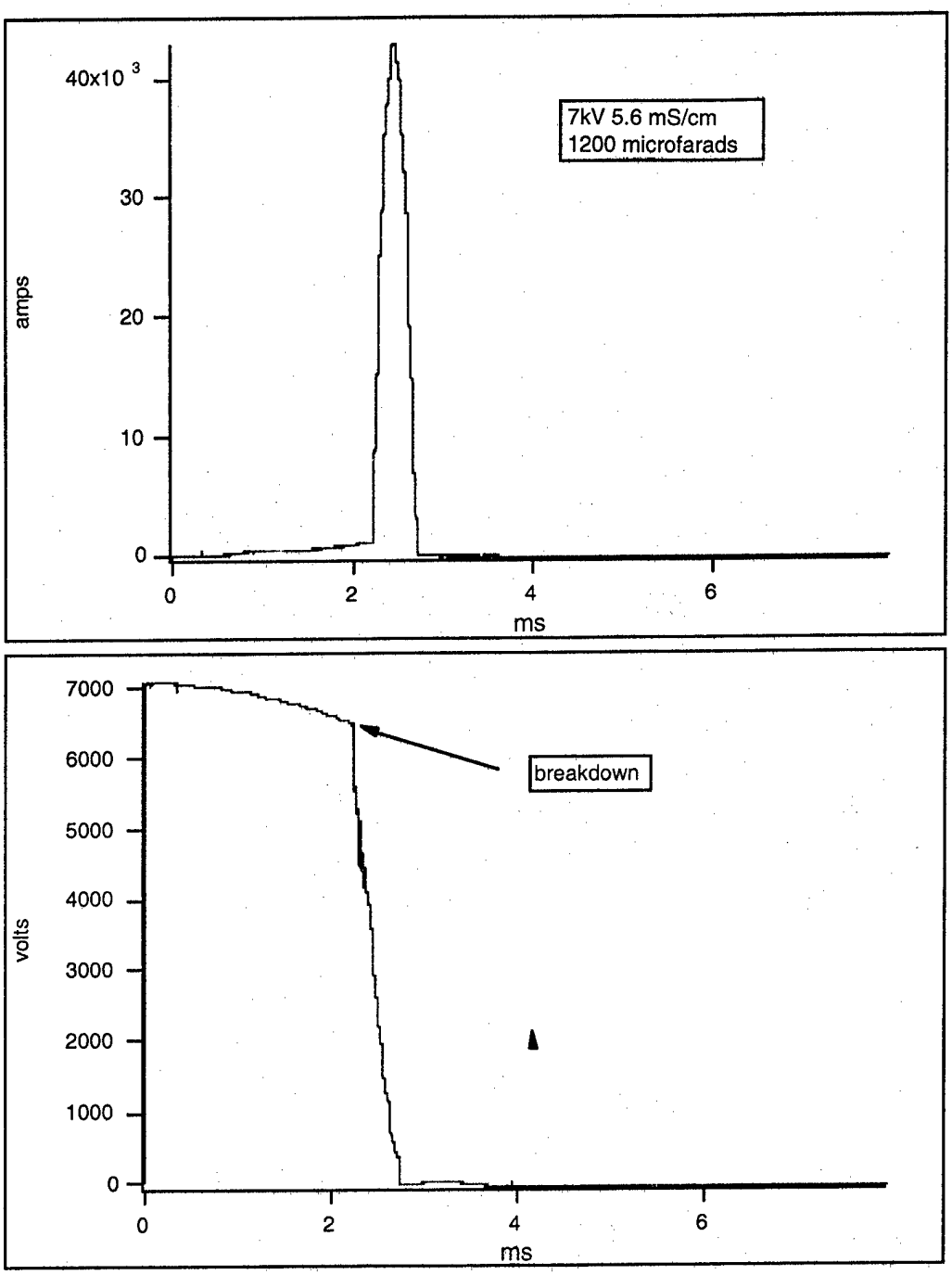

Figure 2.19
Voltage and current.

AS-99-19

Figure 2.20 gives a schematic layout of the experiment on the research vessel (RV) LONGHORN.

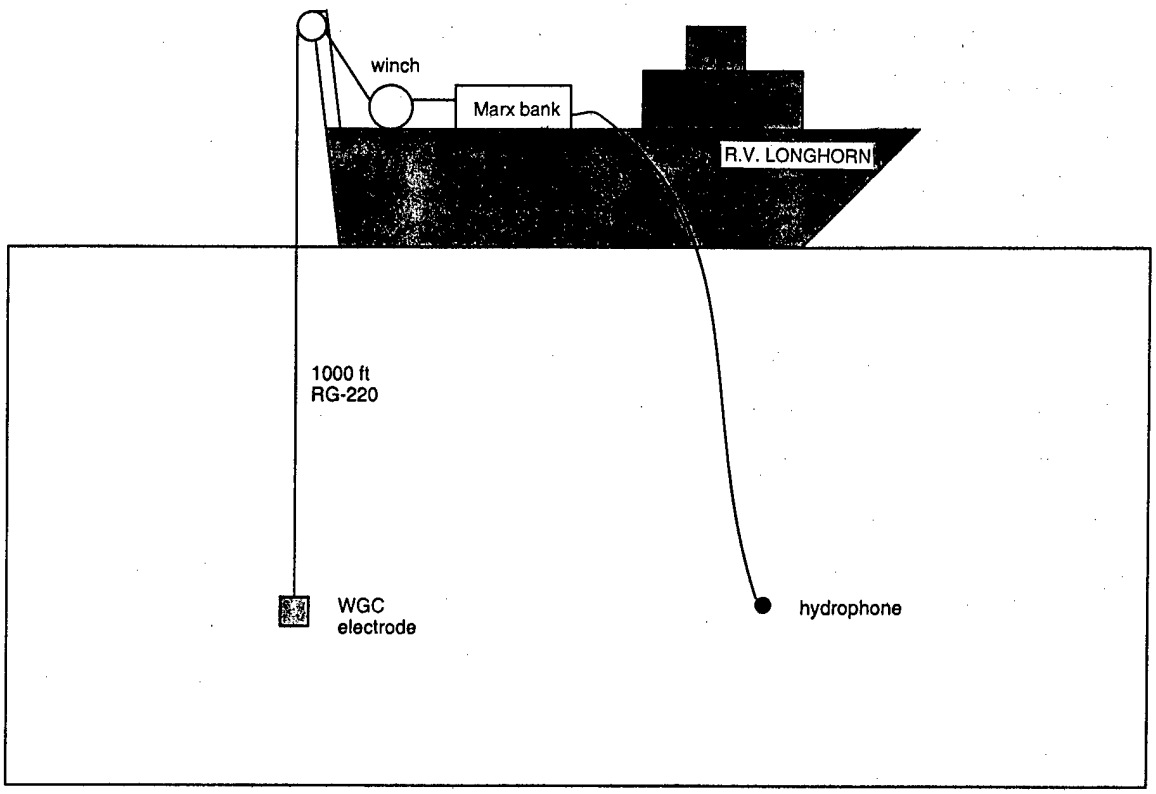

Figure 2.20
Layout of experiment on RV LONGHORN.

AS-99-20

The current was measured by a Pearson current monitor while the voltage was measured by another monitor measuring the current flowing through a series of 10,000-ohm resistors. In order to obtain the voltage at the electrode, the setup was treated as a lumped element circuit. The depth of the electrode was assumed to be the length of the cable fed into the water; this method entails approximately 10% error in the depth, according to a preexisting simulation of the effects of ocean currents on the drift of the coaxial cable. More importantly, it will be seen that the depth had no effect on the breakdown voltages and only a small effect on the corona discharges.

2.4.5 Gulf of Mexico Data Summary

The parameters varied were the voltage, the capacitance, and the depth of the electrode. The different voltages were 28, 32, 36, and 40 kV, while the capacitance was set at two different values: 37.5 and 147.5 microfarads. The electrode was placed at three different depths: 100, 300, and 1000 ft. The most important data set is displayed in Figs. 2.21 and 2.22.

Pressure had no effect on the breakdown and only a minor effect on the corona discharges. Breakdown was identified in the oscillograms by a discontinuity in the first derivative of the current waveform. Some example shots are displayed in Figs. 2.23 through 2.26. Unlike Fig. 2.21, the voltage waveforms displayed were not the calculated voltages at the electrode but the signal actually measured inside the Marx bank. Acoustic waveforms were also included in the figures.

The data taken on the sea trip indicate that the breakdown mechanism for the PSS regime is not a thermal process because depth had no influence on the breakdown voltage.

2.4.6 Lake Travis Experimental Setup

The next experiment to be discussed is neither photographic or empirical. It was an attempt to use a preexisting model developed by previous investigators at ARL:UT. A defect of the model is that there are more fitting parameters than equations. Acoustic data from corona discharges in different salinities were

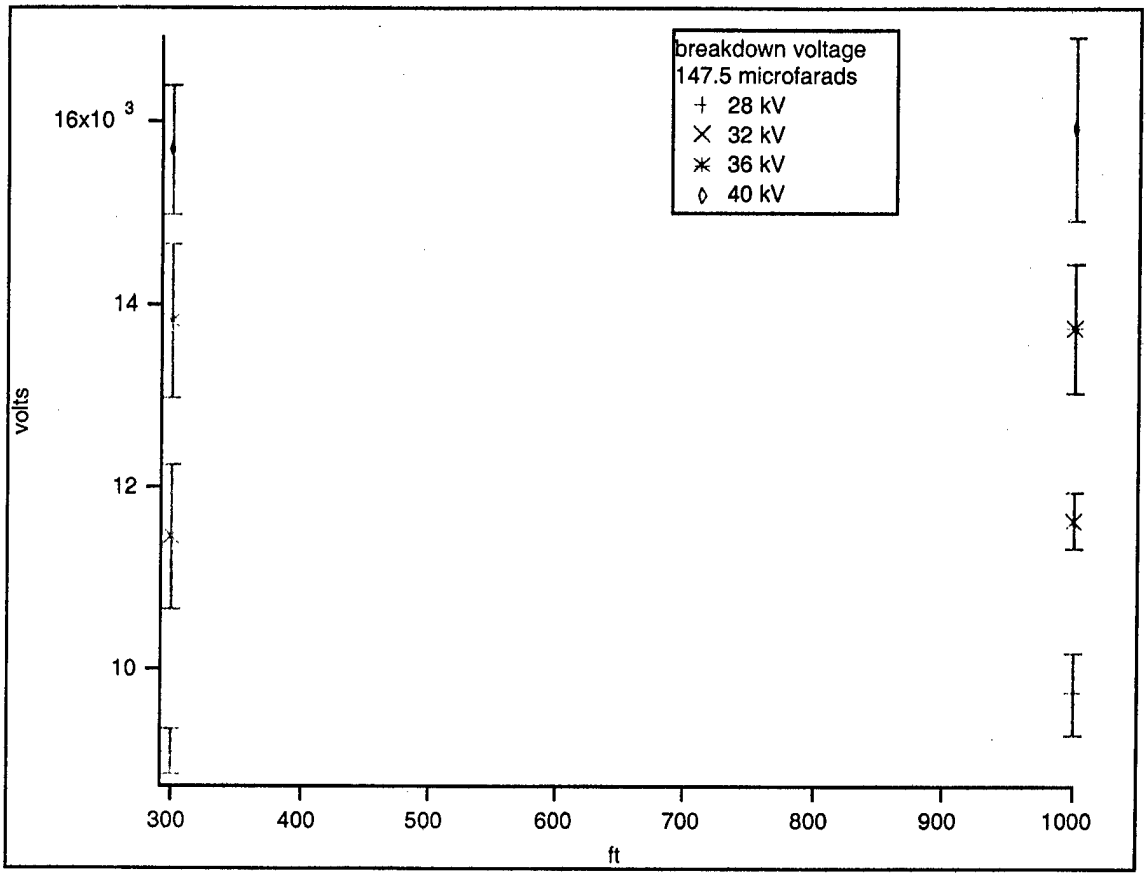

Figure 2.21

Breakdown voltages for WGC electrode.

AS-99-21

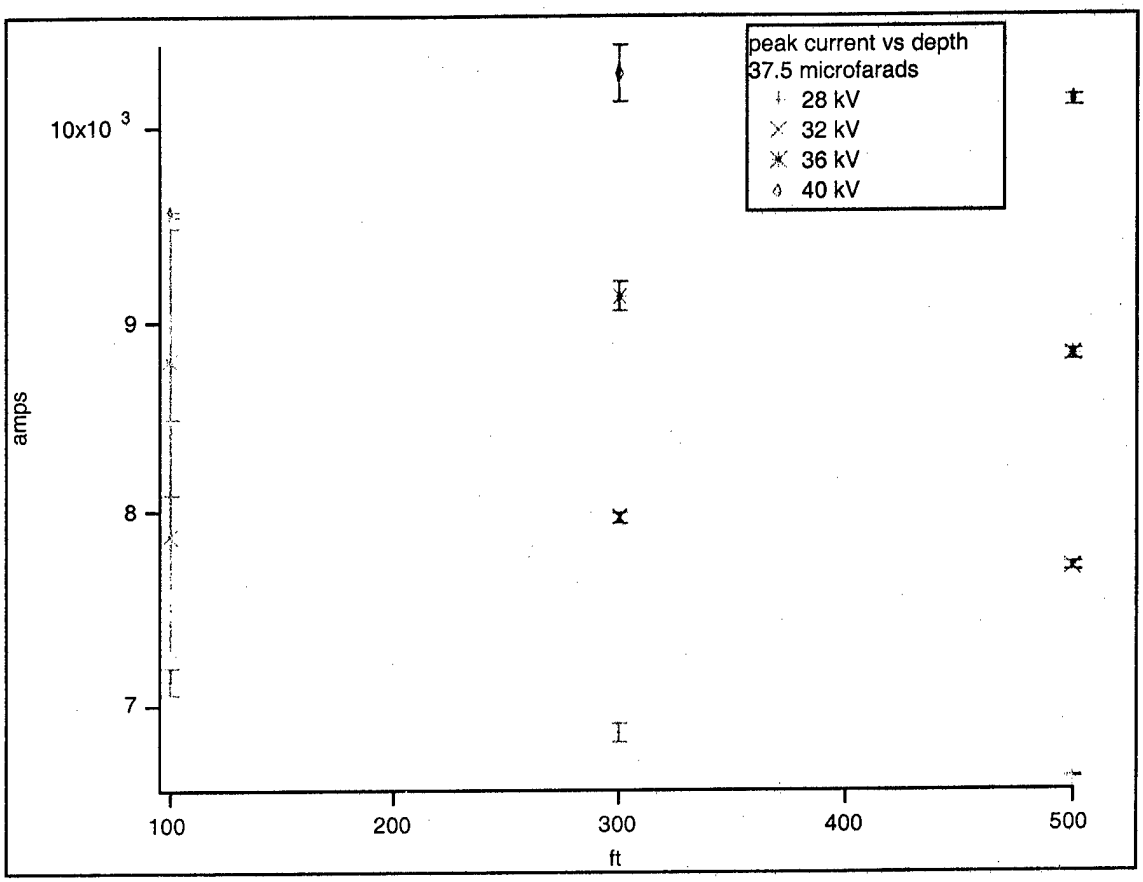

Figure 2.22

Breakdown voltages for WGC electrode.

AS-99-22

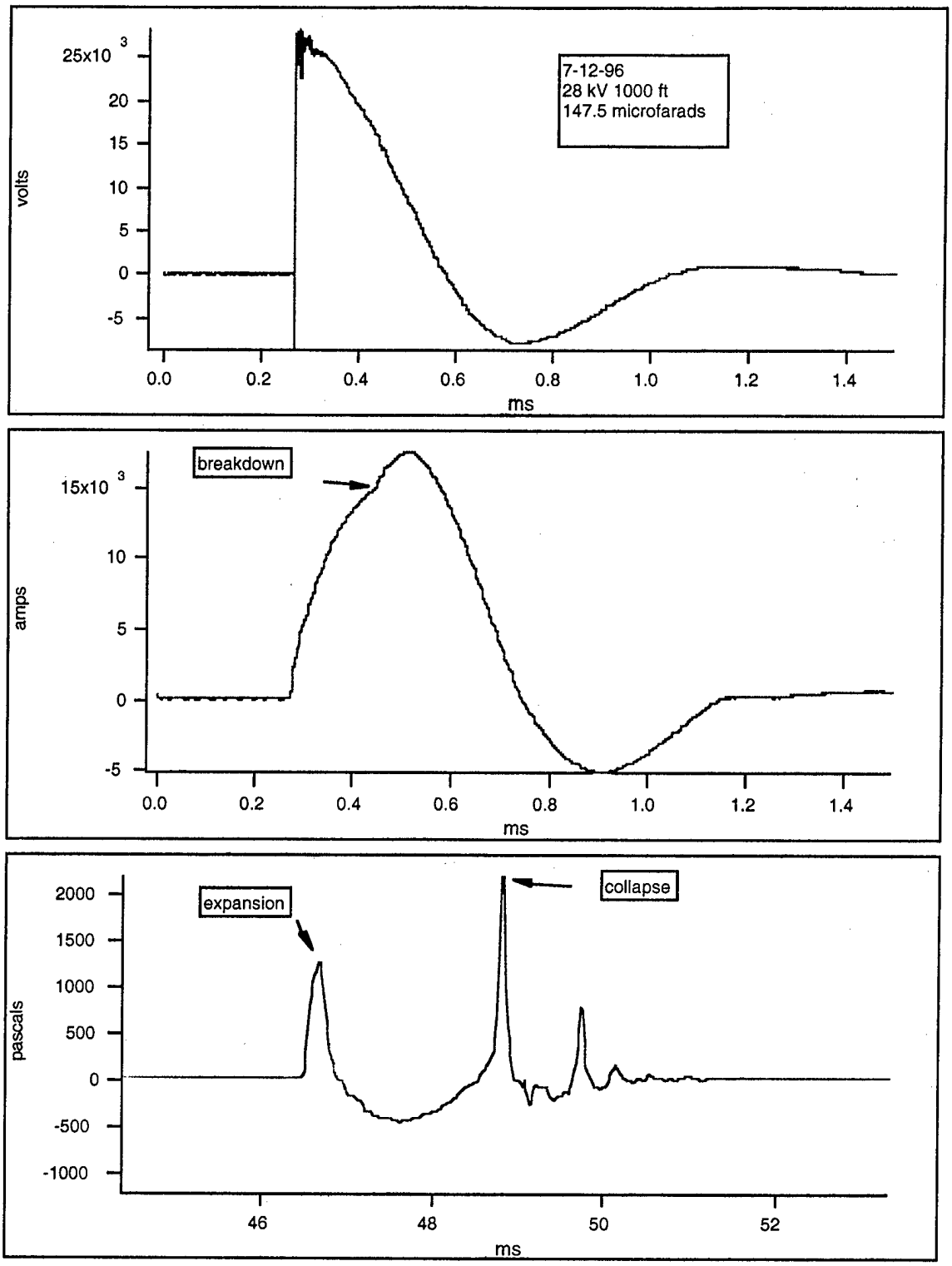

Figure 2.23

Voltage, current, and hydrophone.

AS-99-23

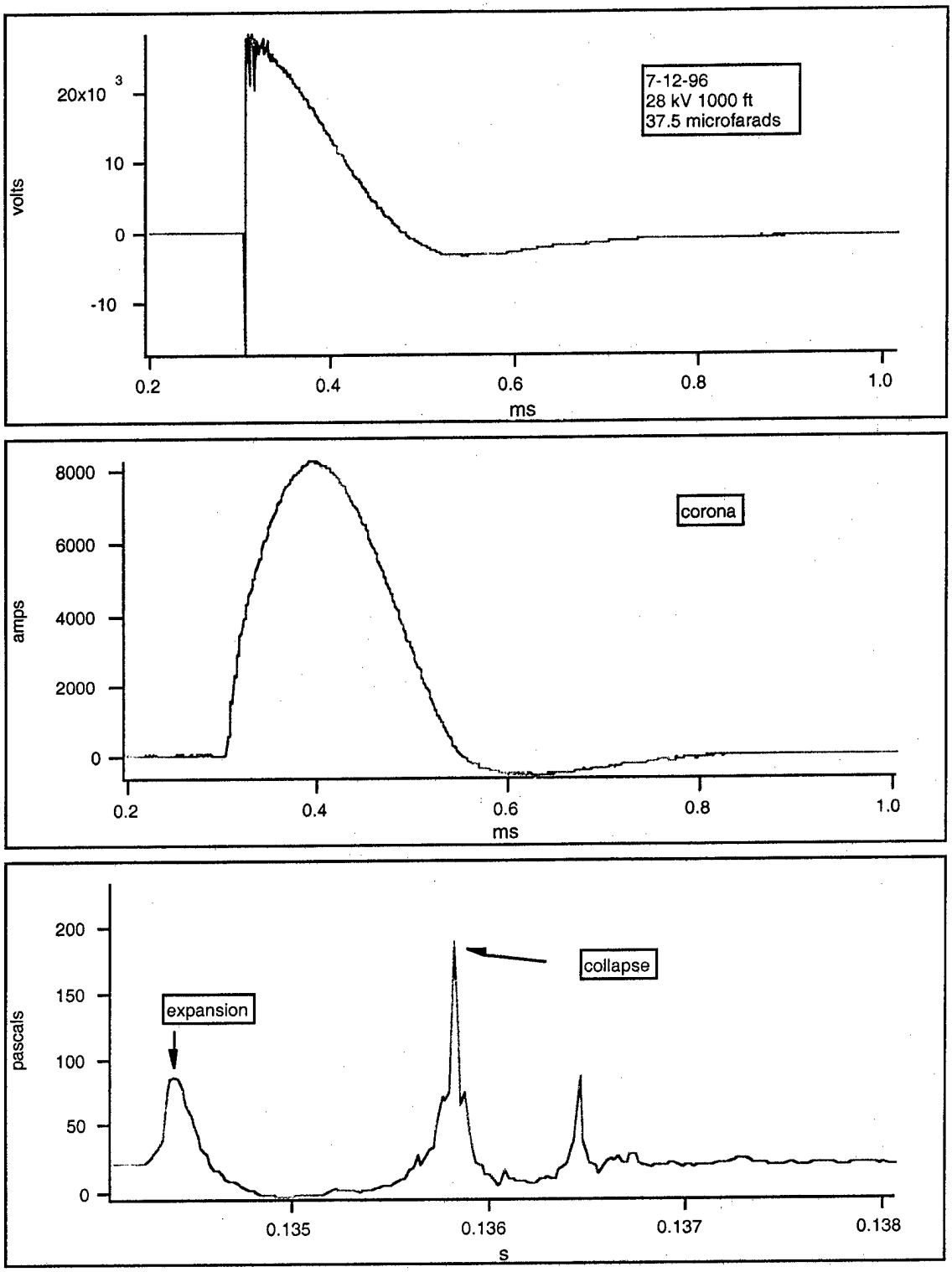

Figure 2.24

Voltage, current, and hydrophone.

AS-99-24

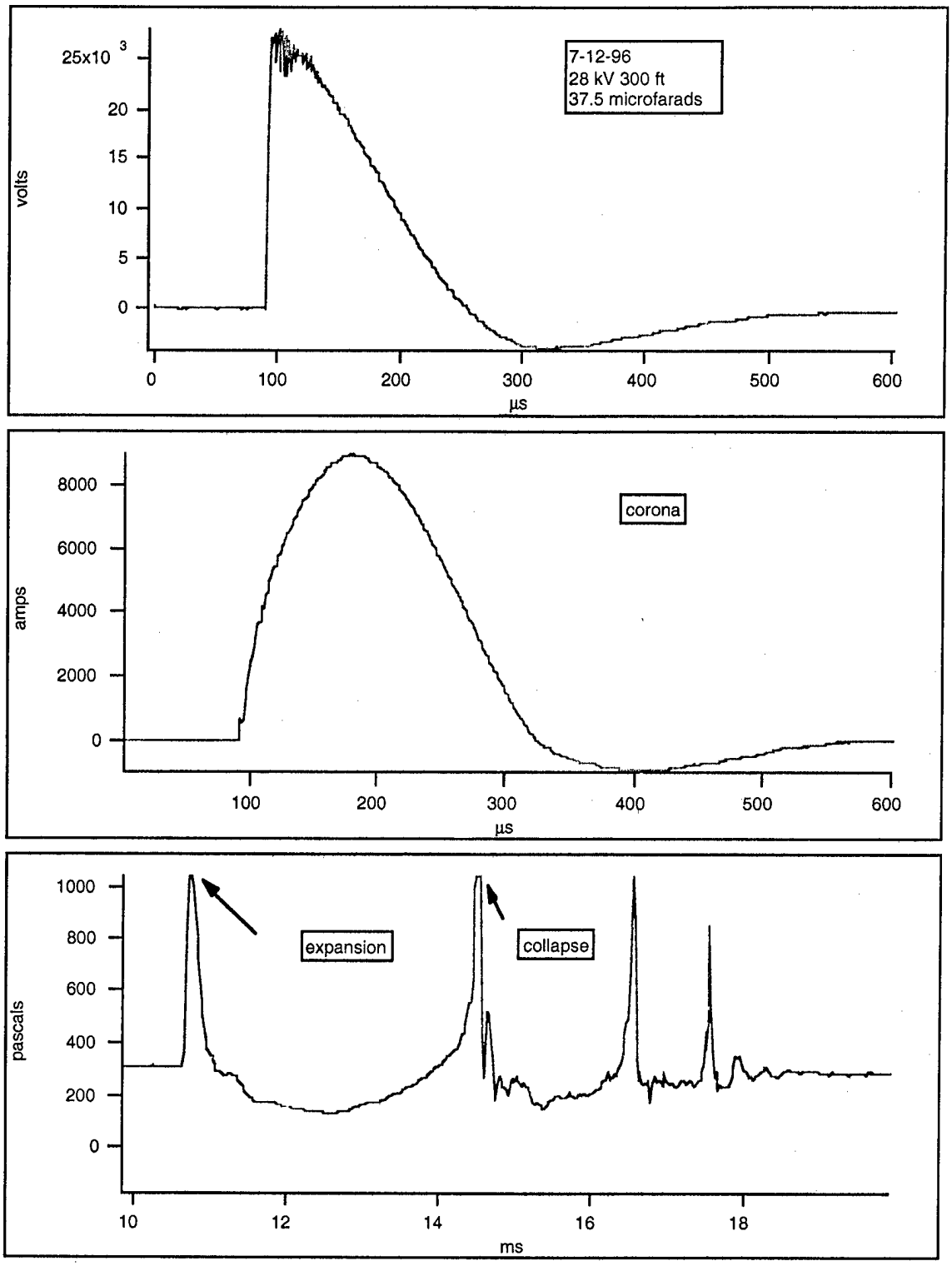

Figure 2.25

Voltage, current, and hydrophone.

AS-99-25

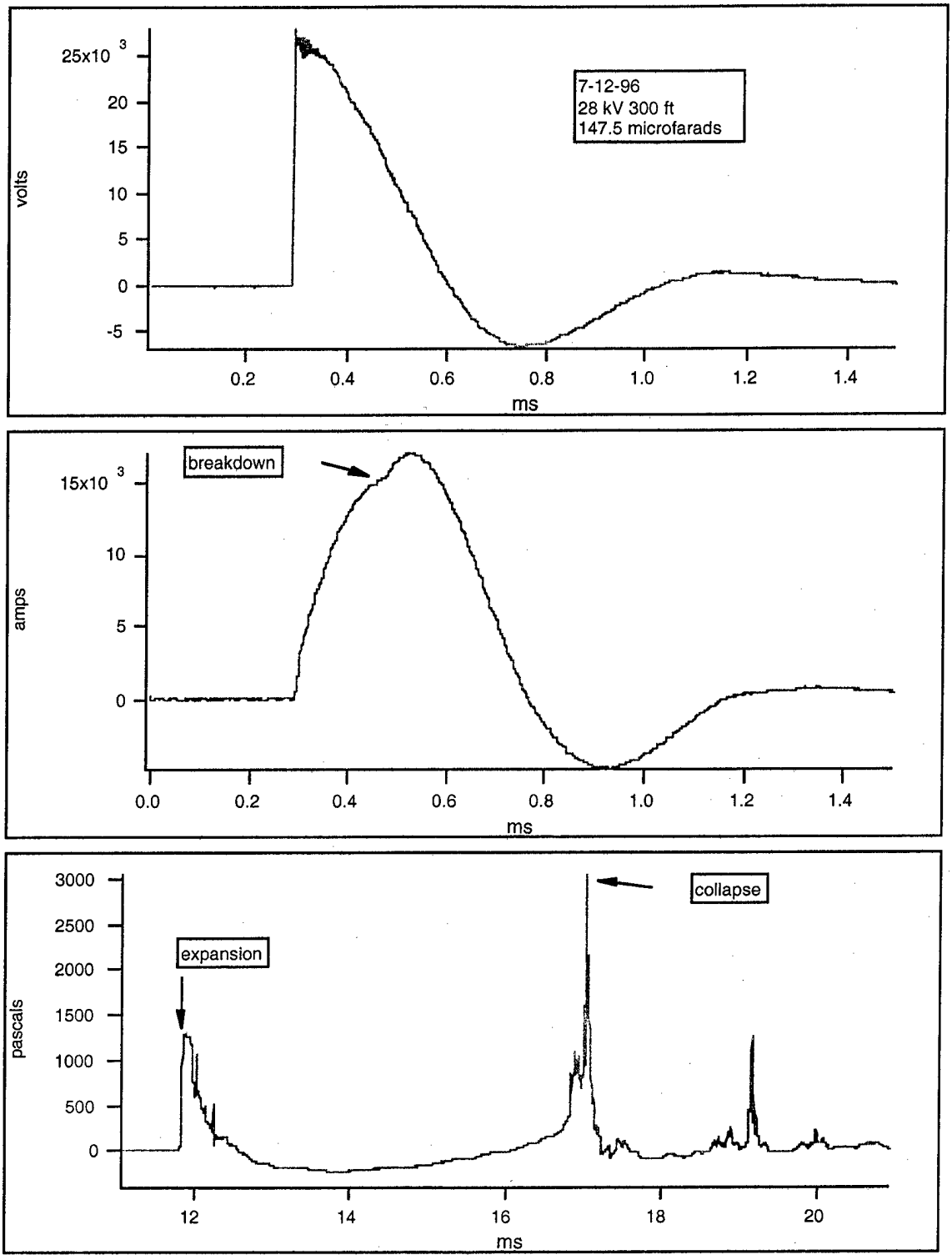

Figure 2.26

Voltage, current, and hydrophone.

AS-99-26

taken in order to attempt to fix one of the parameters. The model equations are as follows:

$$R(N) = R_0 / N \quad ,$$

$$N(r) = \left(r / r_0\right)^{\alpha} \quad ,$$

$$R(r) = R_0 \left(r_0 / r\right)^{\alpha} \quad ,$$

$$I = \left(r(t) / r_0\right)^{\alpha} V / R_0 \quad ,$$

$$dr / dt = \beta \left(V / V_c\right)^{\gamma} \quad .$$

The first equation describes how the resistance of a tree-like structure decreases as the number of branches increases. The second equation gives the number of leader tips as a function of distance from the electrode. Choosing a scale length for one leader tip selects a resistance scale if one assumes that a leader tip can be modeled by a sphere with radius r_0. The parameter α adjusts the amount of branching and can take on values between 0 and 3; a value of 3 would simulate a volume-filling plasma sphere. The equation for the resistance R_0 is plugged into Ohm's law, giving us a relationship between current and voltage. In order to complete the model, one must decide on how fast the leaders are growing away from the electrode. The last equation supplies us with the answer. V_c is a selected scale voltage. Gamma is varied in order to fit the electrical data. No obvious way of connecting the acoustic data with this model was found, but parameters of the model were found to make the equations fit the electrical waveforms.

A diagram showing the basic experimental setup is shown in Fig. 2.27. The setup was housed on the step barge at the Lake Travis Test Station (LTTS). The power supply was capable of charging the 50-microfarad capacitor up to

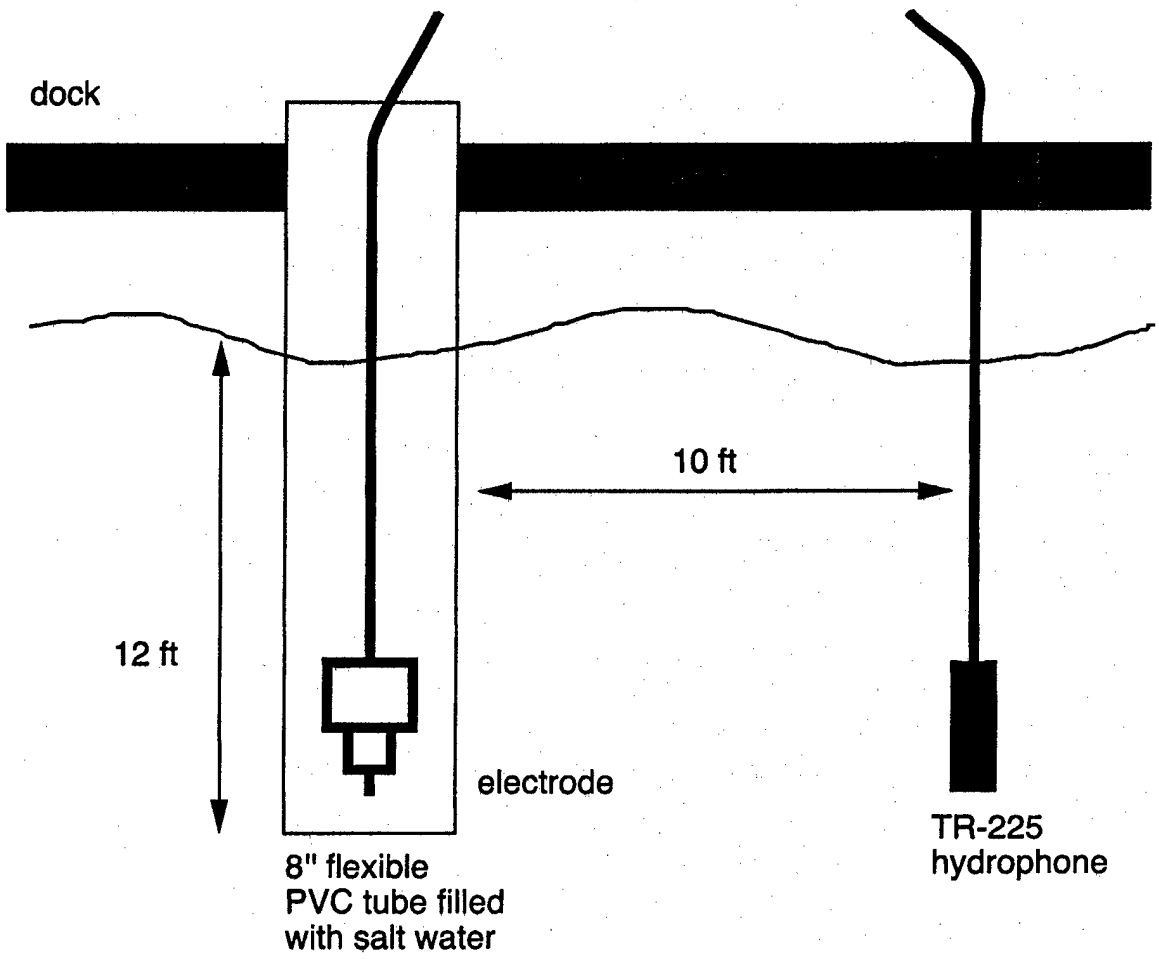

Figure 2.27

Sea test experimental setup.

AS-99-27

10 kV. The cable connecting the corona electrode to the ignitron was a 10-gauge, 8-conductor electrical cable, about 20 ft long. The current was measured using a Pearson current monitor model number 101. The voltage was measured by connecting a 10,000 ohm network in parallel with the electrode and monitoring the current passing through the network.

2.4.7 Lake Travis Data Summary

As already mentioned in the previous section, this experiment was conducted as an attempt to fix parameters in a fractal model and was not an attempt to take large quantities of data. The free parameters in the model were adjusted in order to fit the experimental data, but since the model excludes ionic heating, the physical meaning of the fractal model may be overwhelmed in this low voltage regime. Figures 2.28 through 2.30 show sample discharges at 7 kV in three different conductivities.

2.4.8 Wollensak Photographic Experiment

The inability to use the acoustic signals to fix one of the free parameters in the fractal model forced us to examine a corona photographically using the electrode shown in Fig. 2.31. A preexisting framing camera, capable of framing speeds of up to 6000 frames per second, was used inside a 30-gallon aquarium tank to film discharges of the corona electrode also used at Lake Travis. In order to match up the electrical waveforms with the frames, a timing light was used to expose an edge of the film. The same electrical setup as in the Lake Travis experiment was used. A schematic of the optical setup is shown in Fig. 2.32. Only two conductivities were photographed: fresh tap and 1 mS/cm. Any higher conductivities increased the danger of the aquarium being destroyed.

Two pairs of electrical waveforms are shown in Figs. 2.33 and 2.34.

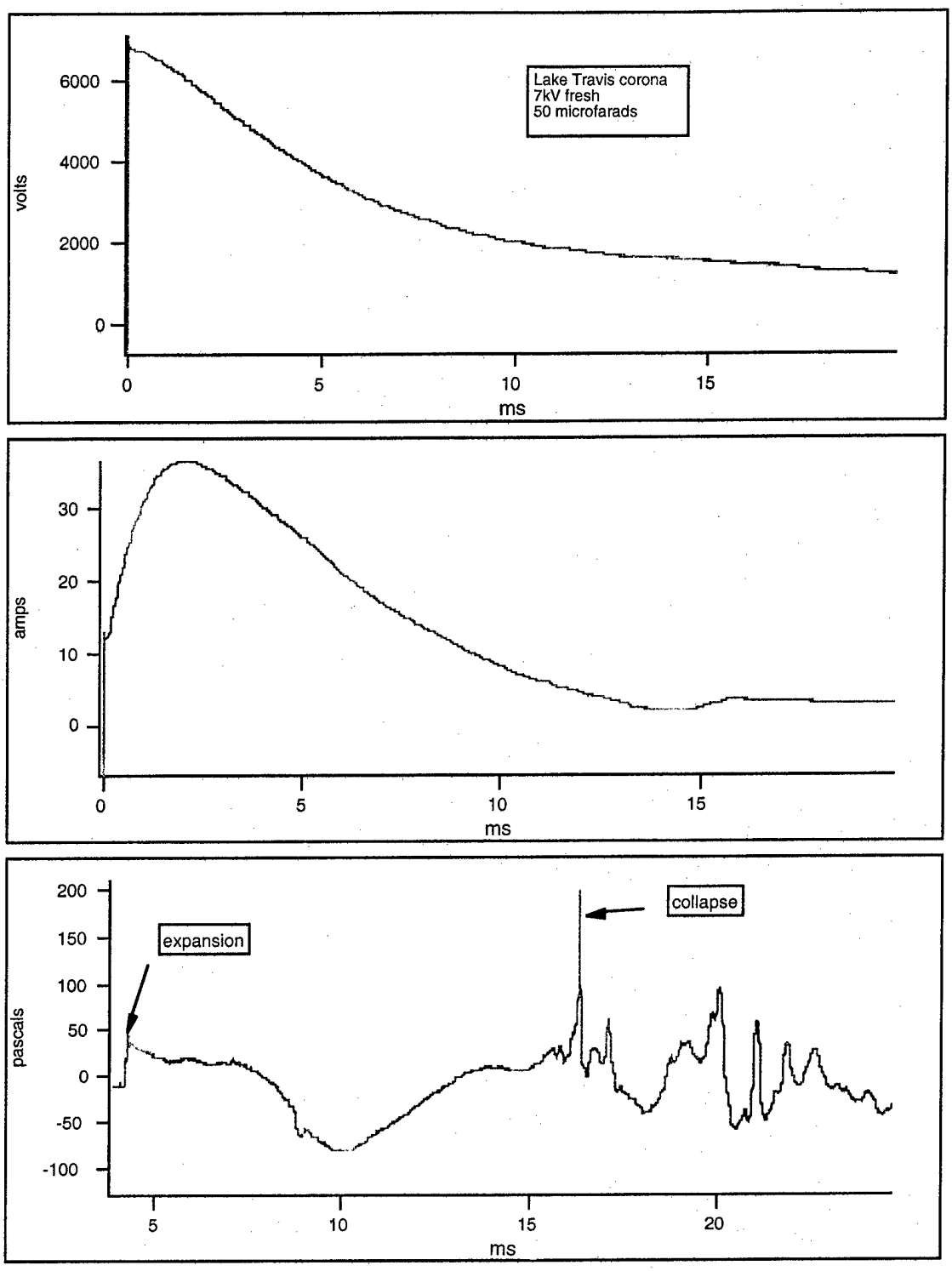

Figure 2.28

Voltage, current, and hydrophone.

AS-99-29

Note: the voltage waveform cutting off at about 3.5 ms is due to the ignitron.

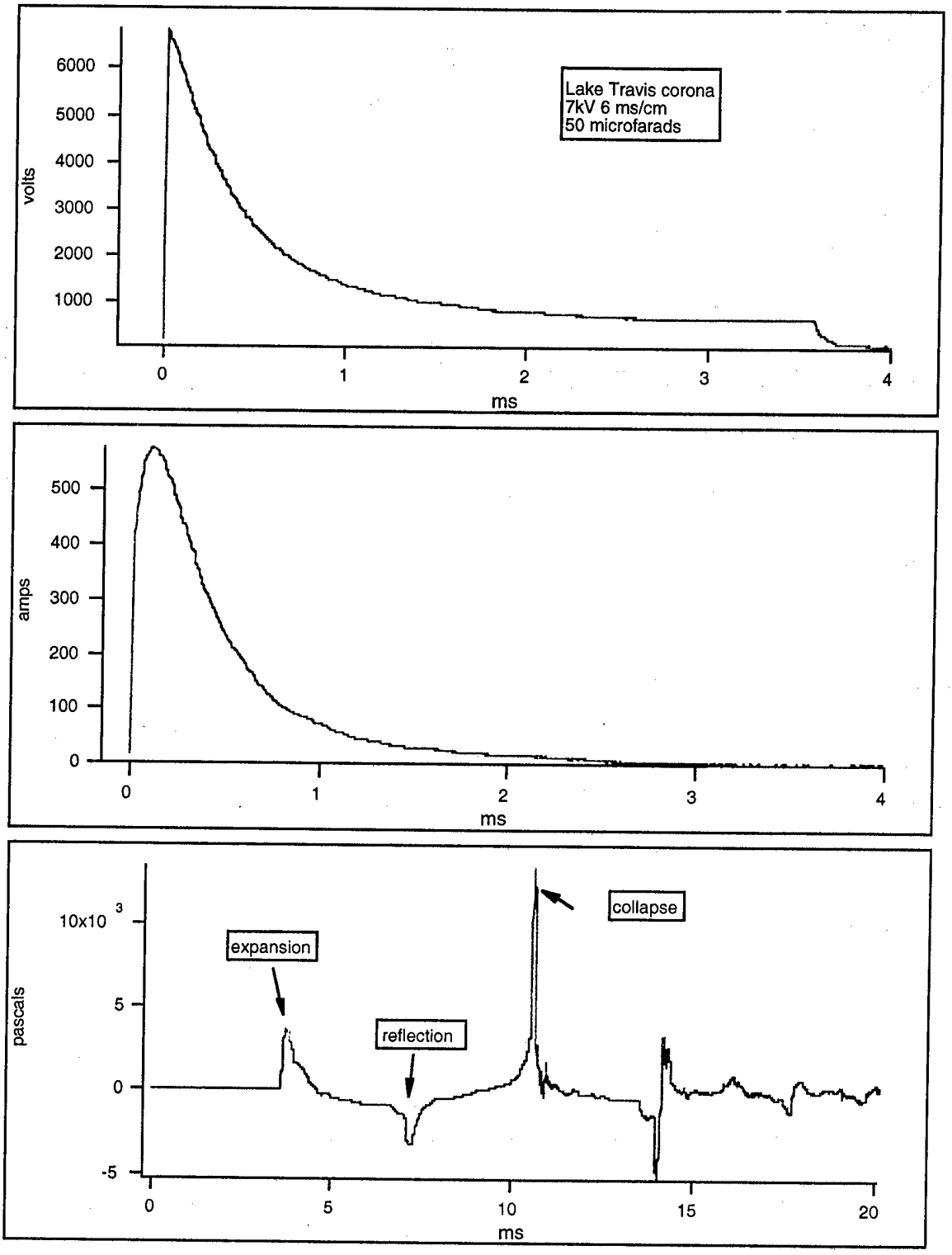

Figure 2.29

Voltage, current, and hydrophone.

AS-99-30

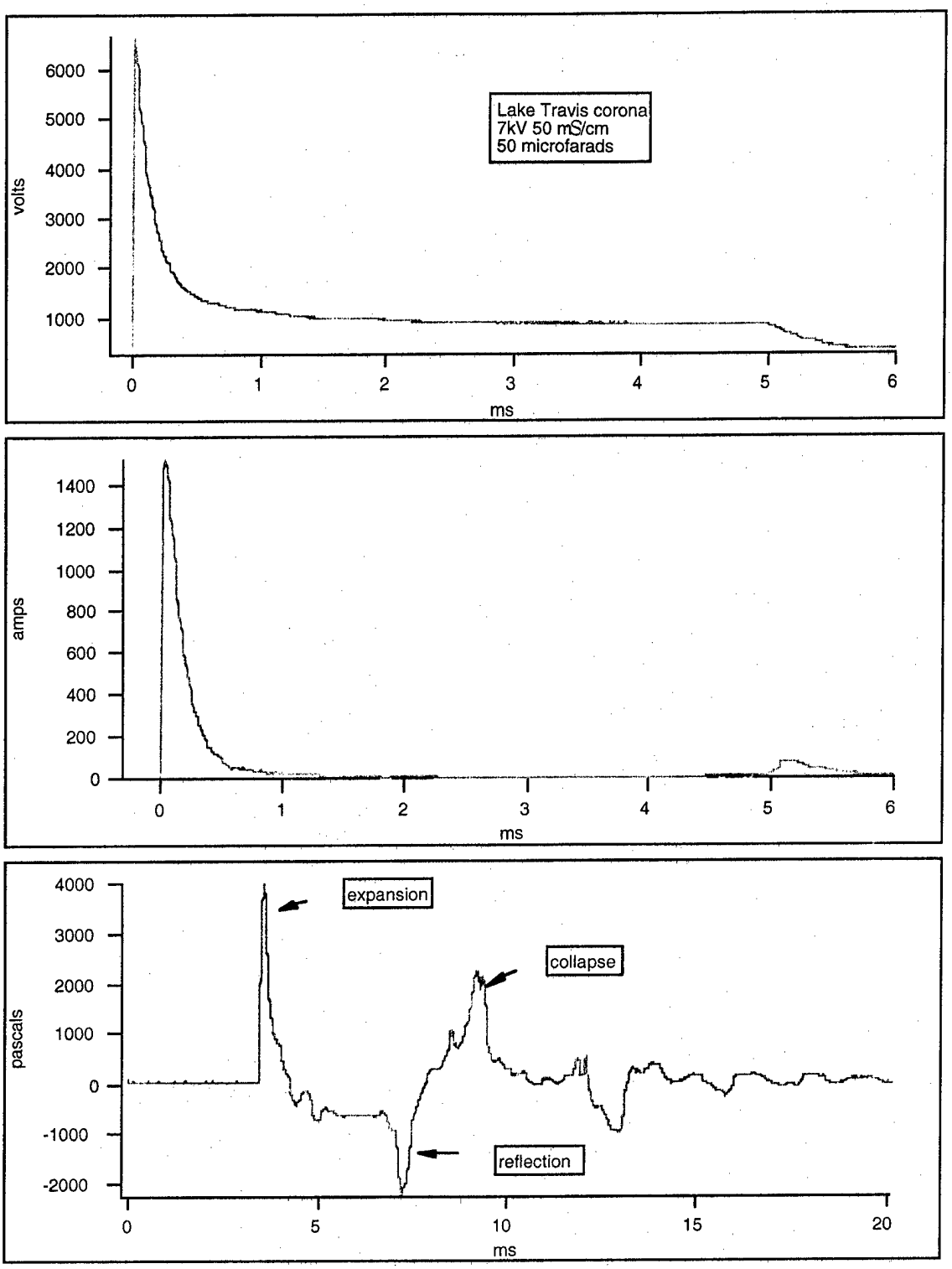

Figure 2.30

Voltage, current, and hydrophone.

AS-99-31

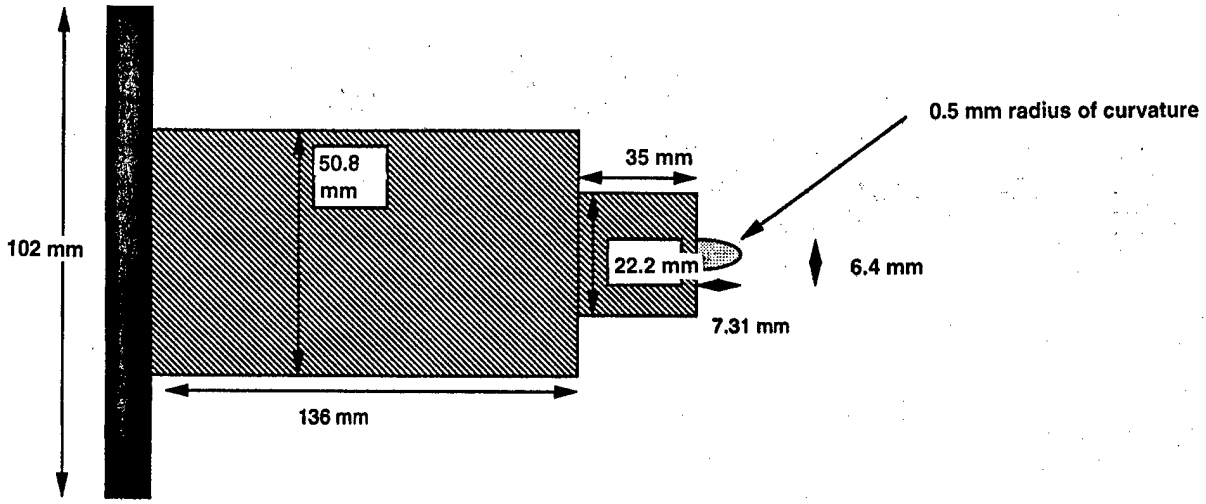

Figure 2.31

An expanded view of the electrode used in the experiment.

AS-99-28

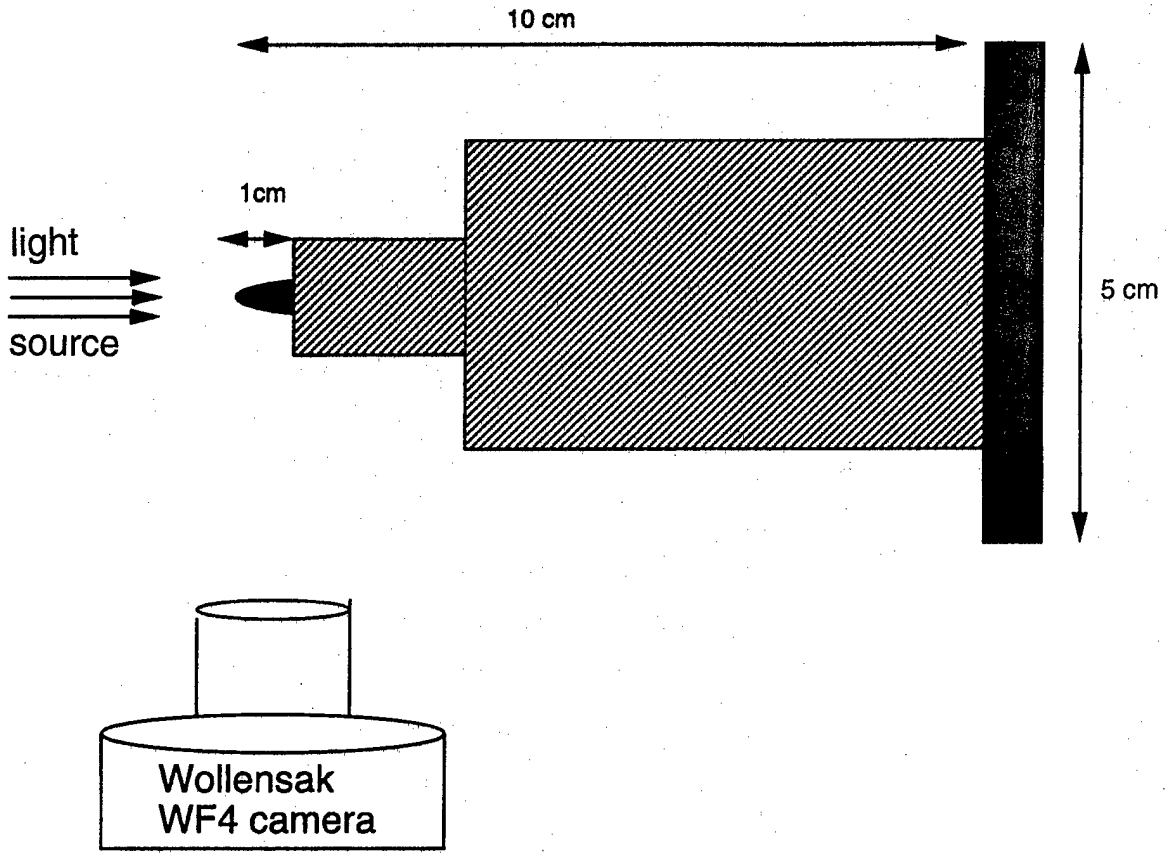

Figure 2.32

Configuration for high speed photographs.

AS-99-32

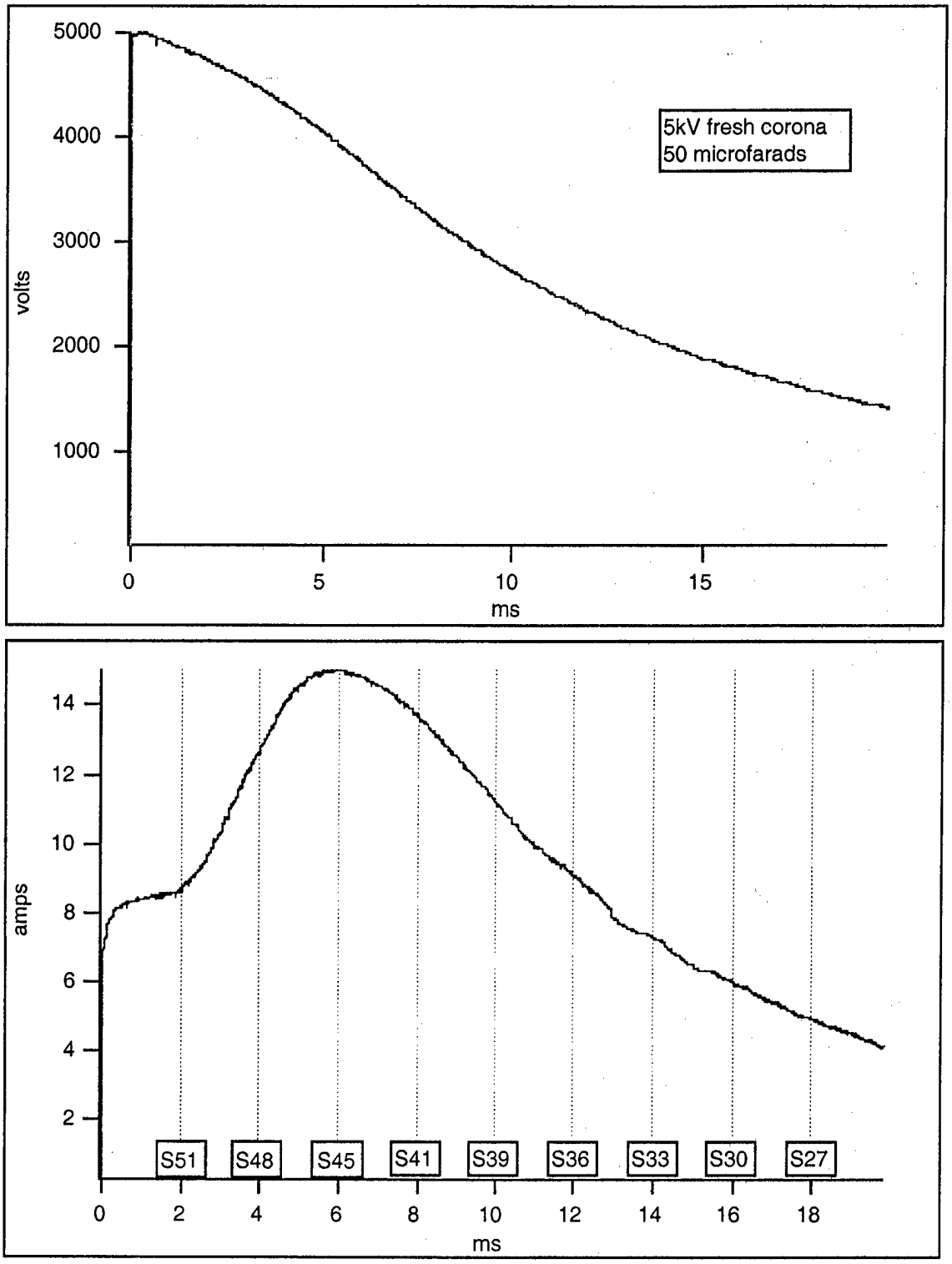

Figure 2.33

Voltage and current.

AS-99-33

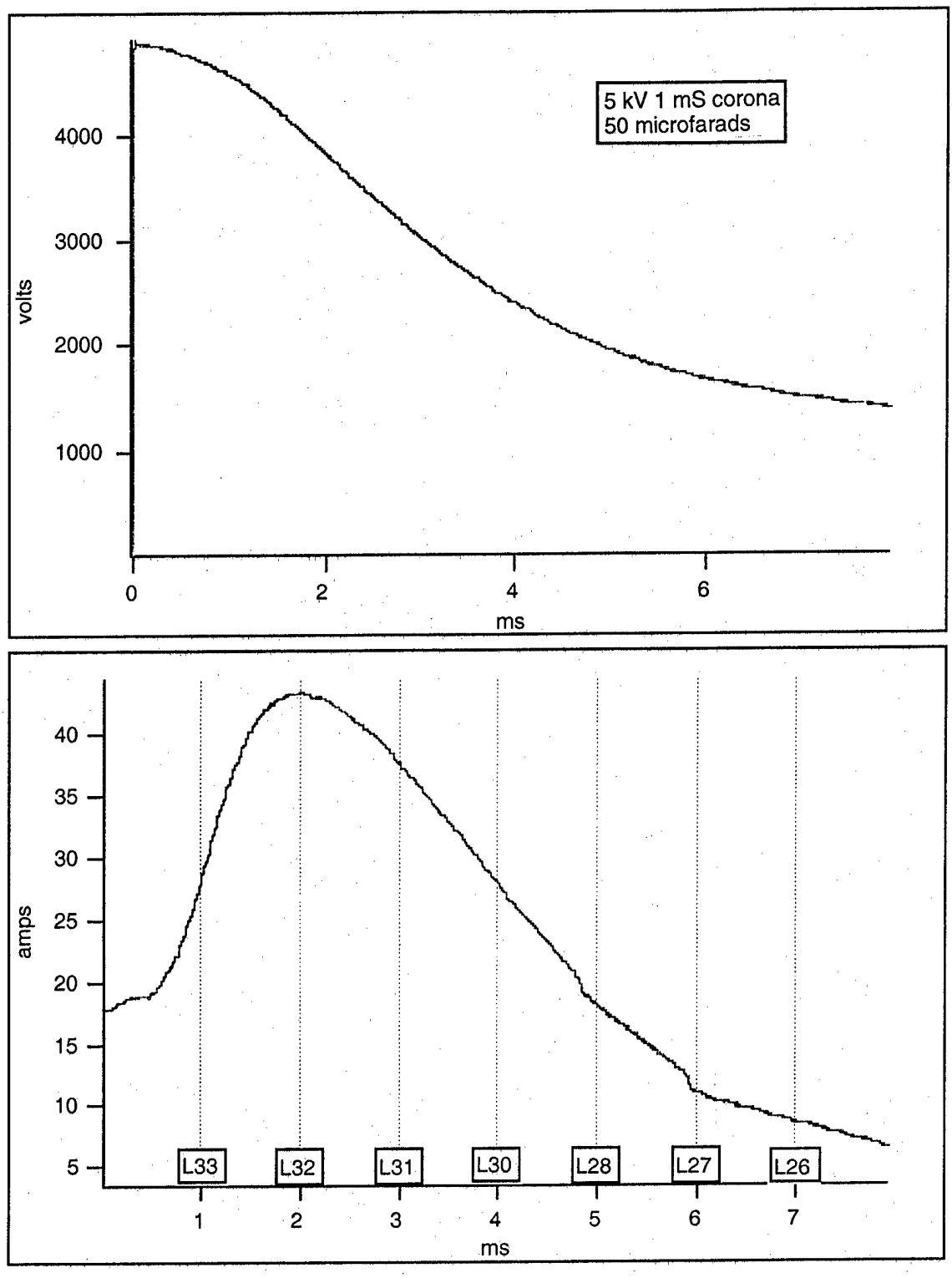

Figure 2.34

Voltage and current.

AS-99-34

2.4.9 CCD Camera Experiments

The photographs from the Wollensak experiment showed that there is a nonluminous precursor; most of the luminous events occur either at or after the current peak. To see the physical phenomena occurring in the shoulder of the current waveforms of the corona discharges, a faster camera was needed. An HS Motion Analyzer Model 450 was rented; it was capable of framing speeds of 40,500 frames per second, able to record events with low light levels, and had video storage capability. The corona electrode was filmed just as in the Wollensak experiment, and the electrical data were collected just as in the Lake Travis experiment. Four discharges are shown in Figs. 2.35 through 2.43. They corroborate the findings from the Wollensak experiment that the brightest part of the discharge occurred after the peak current. Figure 2.39, with its corresponding sequence of photographs, clearly shows a preexisting bubble located on or near the tip of the corona electrode. This bubble stretches when the electric field is first turned on, relaxes after the Maxwellian relaxation time of the solution, and then plays no further part in the discharge. Thus, we do not see any evidence that the bubble was an initiation point for leader formation. This sequence of photographs gives strong evidence against electrical discharges being preceded by thermal processes. The film of the corona in Figs. 2.42 and 2.43 suggests the beginnings of leaders, but the data are inconclusive on this point.

2.4.10 Discussion

The experiments demonstrated the presence of ionic heating in leader or prebreakdown phase of the arc discharges. They also confirmed the similarity between the ARL:UT regime and the existing literature on dielectric breakdown in water. There is no evidence that steam bubble growth contributes to breakdown, but it may slow down breakdown by diverting energy away from the leaders. To study the leaders, more sophisticated techniques must be brought to bear on this physical phenomenon.

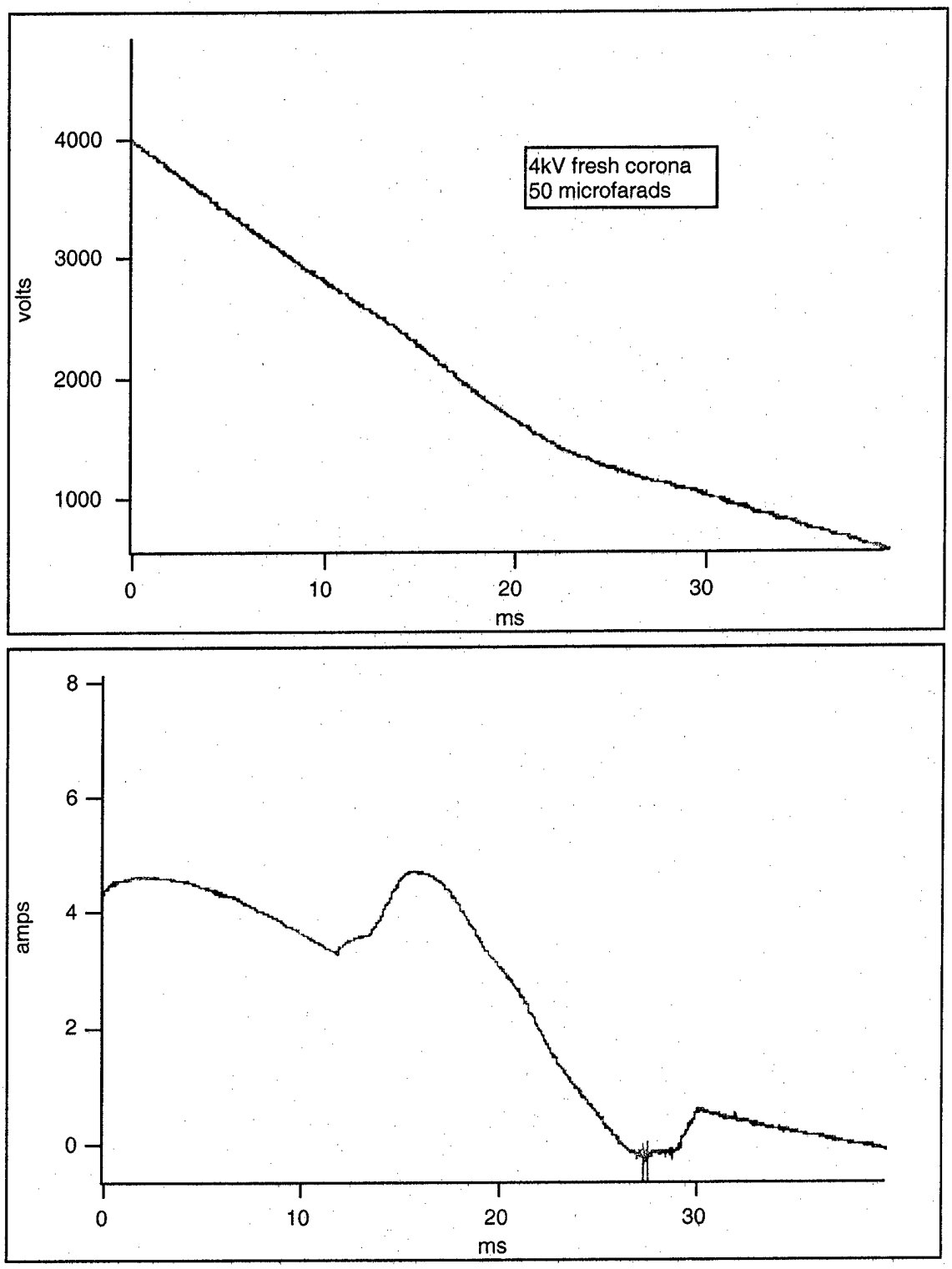

Figure 2.35

Voltage and current.

AS-99-35

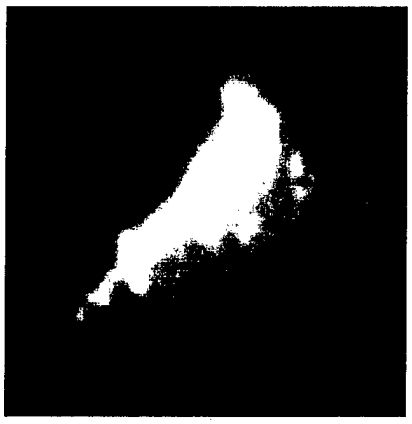

Frame 80 / Time: 0.0087

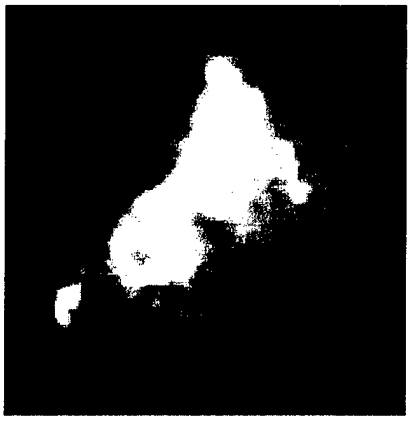

Frame 107 / Time: 0.0110

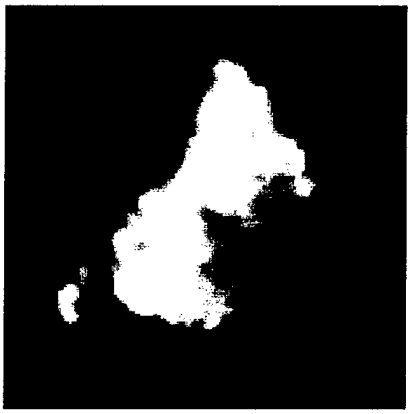

Frame 108 / Time: 0.0118

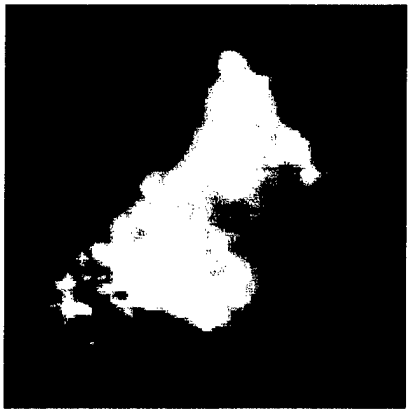

Frame 109 / Time: 0.0120

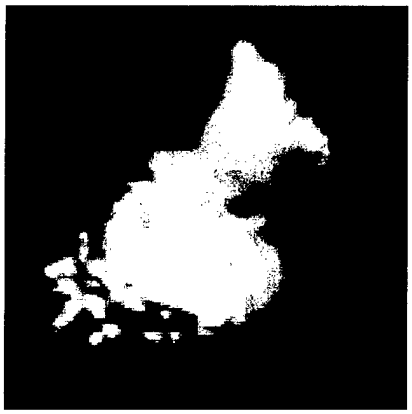

Frame 110 / Time: 0.0121

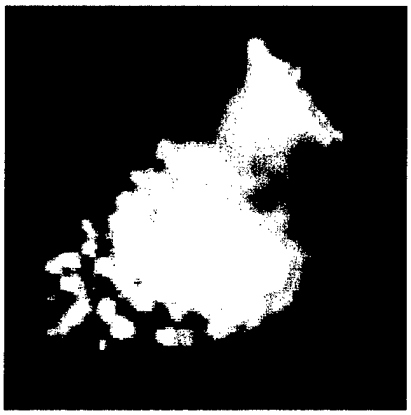

Frame 111 / Time: 0.0122

ID No. 4
Rec. Rate: 9000

Figure 2.36

Photographs corresponding to Fig. 2.35.

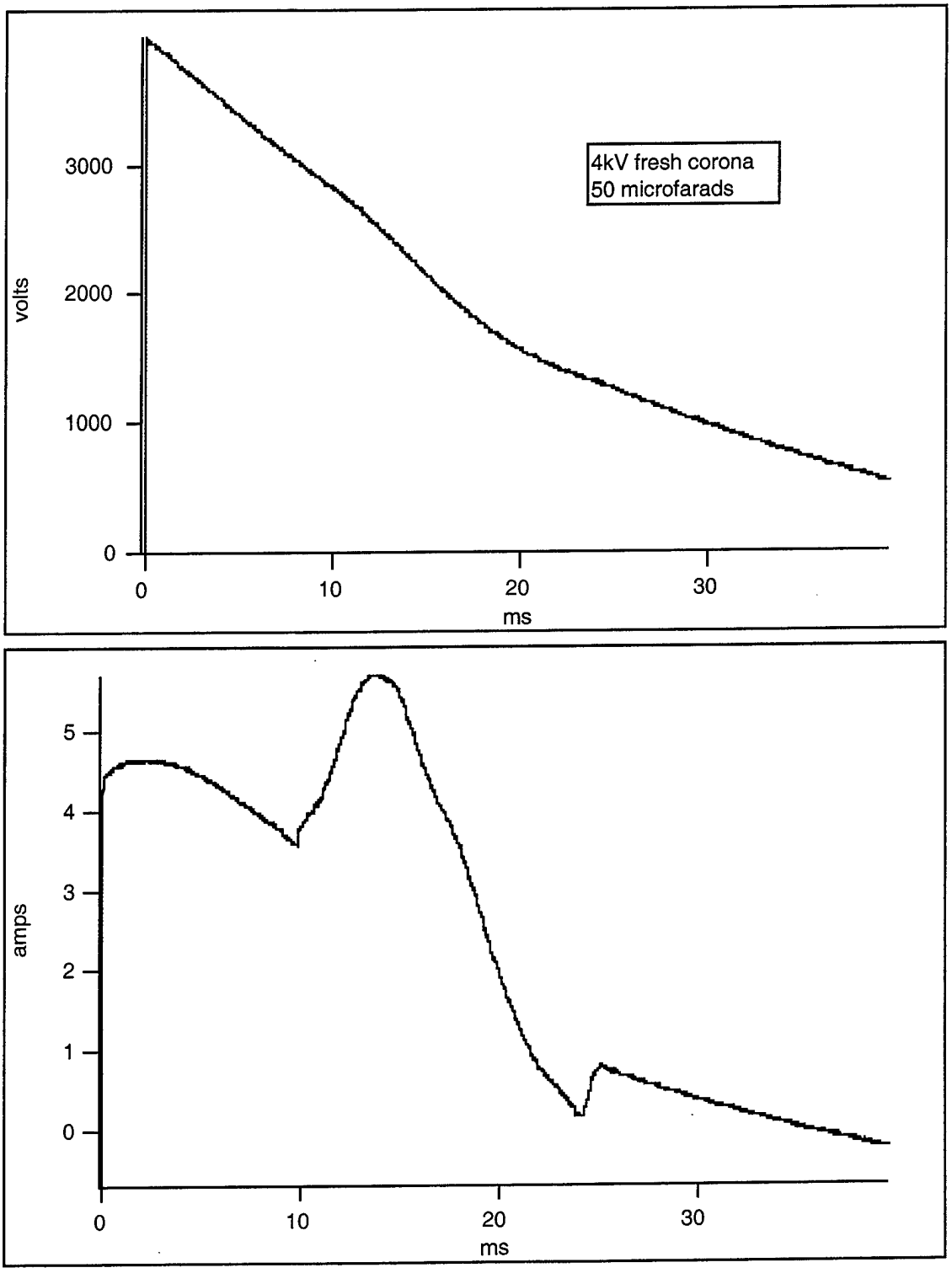

Figure 2.37

Voltage and current.

AS-99-37

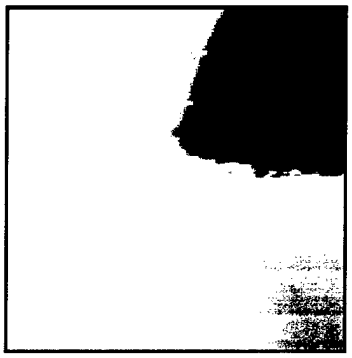

Frame 3 / Time: 0.0001

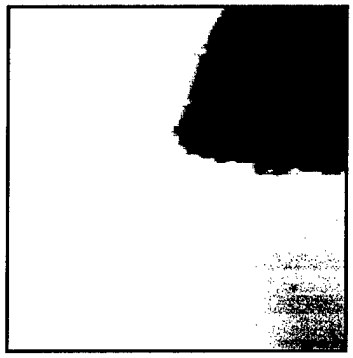

Frame 4 / Time: 0.0002

Frame 5 / Time: 0.0002

Frame 6 / Time: 0.0003

Frame 7 / Time: 0.0004

Frame 8 / Time: 0.0005

Frame 9 / Time: 0.0005

Frame 10 / Time: 0.0006

ID No. 7
Rec. Rate: 13500

Figure 2.38

Photographs corresponding to Fig. 2.37.

Note: filmed at 9000 frames per second; corresponding picture ID No. 6. Clearly shows small attached bubble not contributing to discharge.

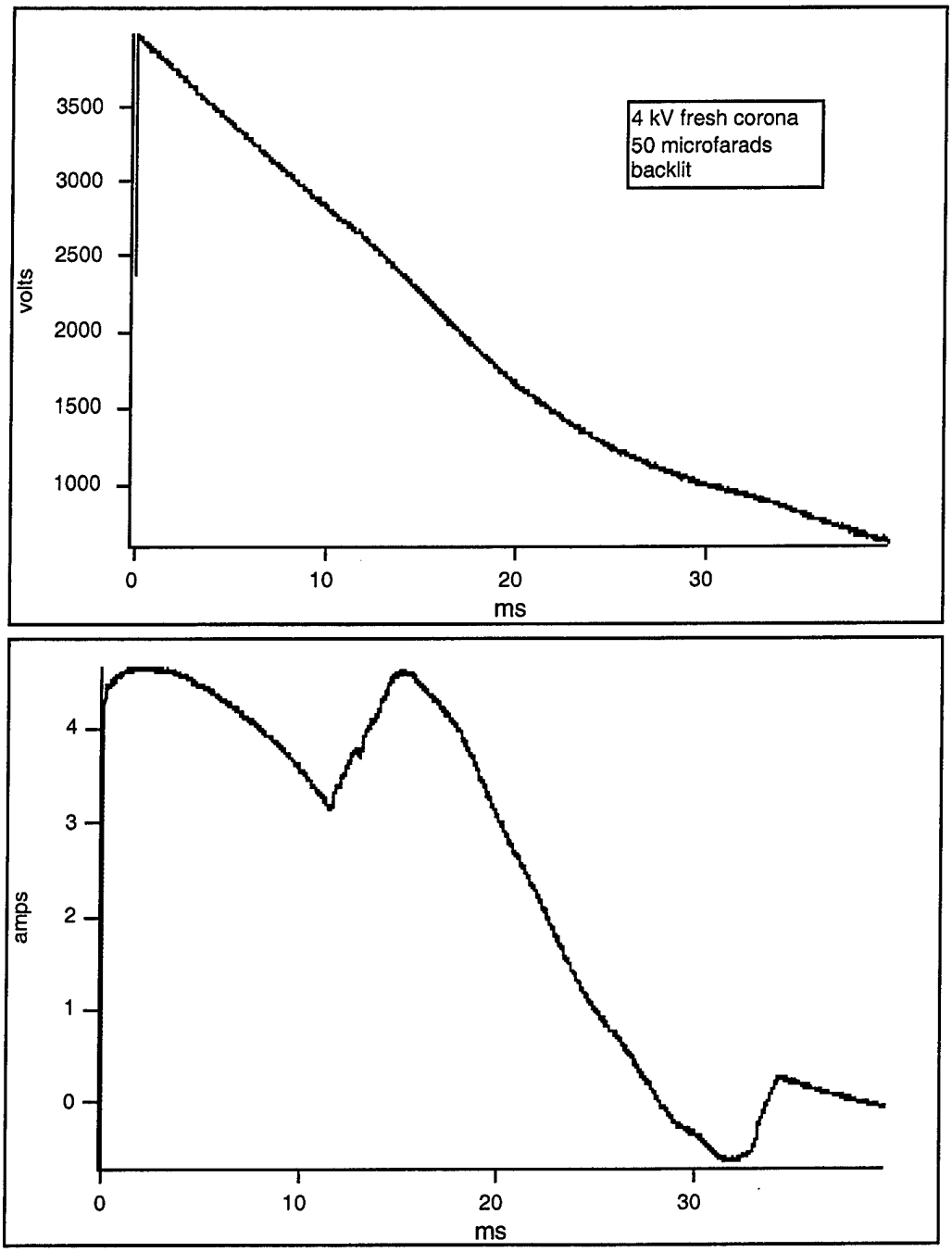

Figure 2.39

Voltage and current.

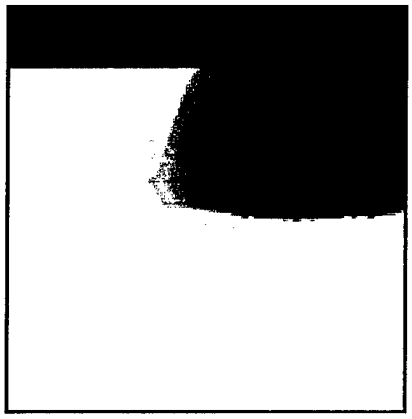

Frame 2 / Time: 0.0001

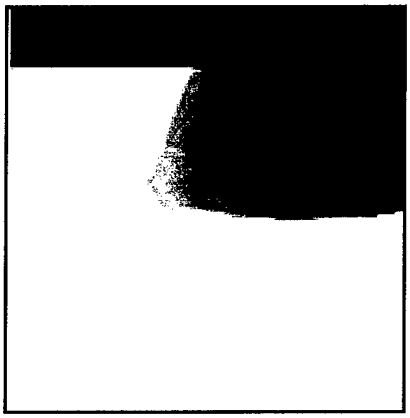

Frame 3 / Time: 0.0002

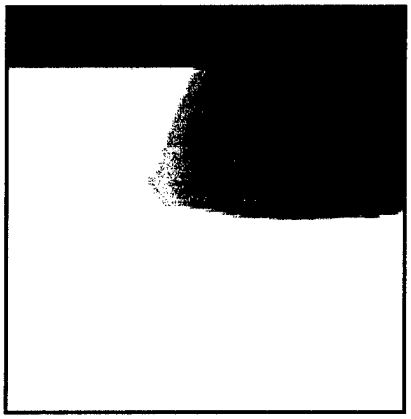

Frame 4 / Time: 0.0003

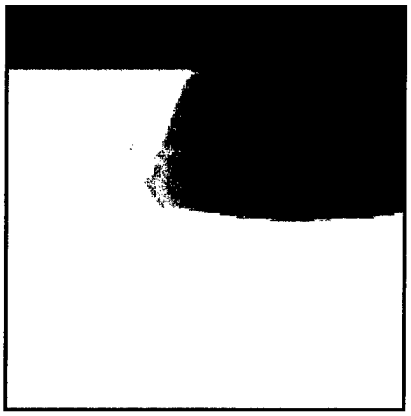

Frame 5 / Time: 0.0004

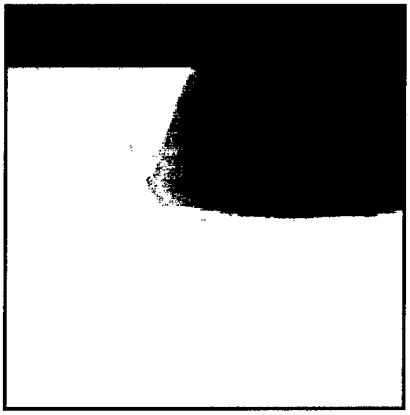

Frame 6 / Time: 0.0005

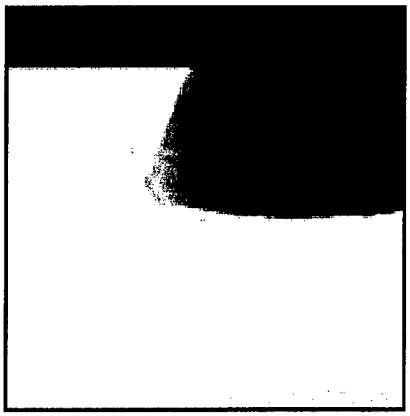

Frame 7 / Time: 0.0006

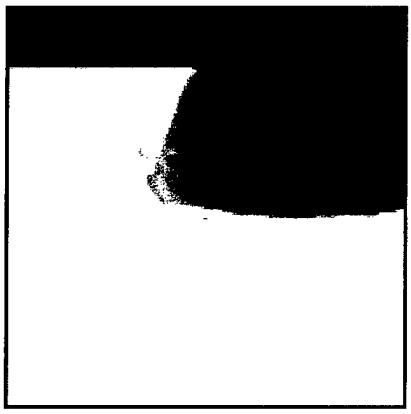

Frame 8 / Time: 0.0007

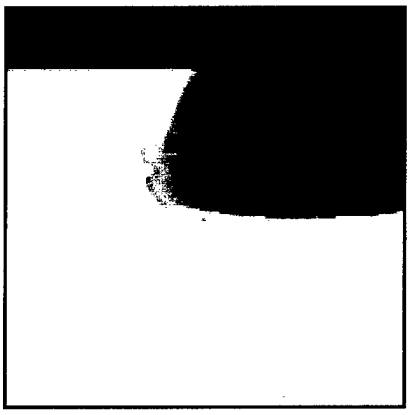

Frame 9 / Time: 0.0008

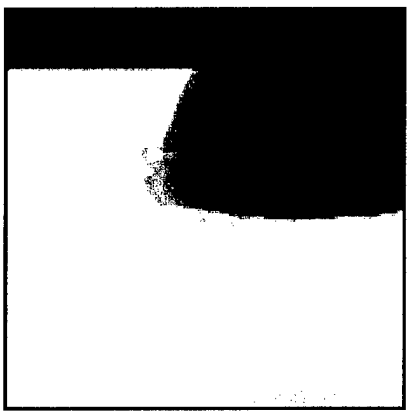

Frame 10 / Time: 0.0010

ID No. 6
Rec. Rate: 9000

Figure 2.40

Photographs corresponding to Fig. 2.39.

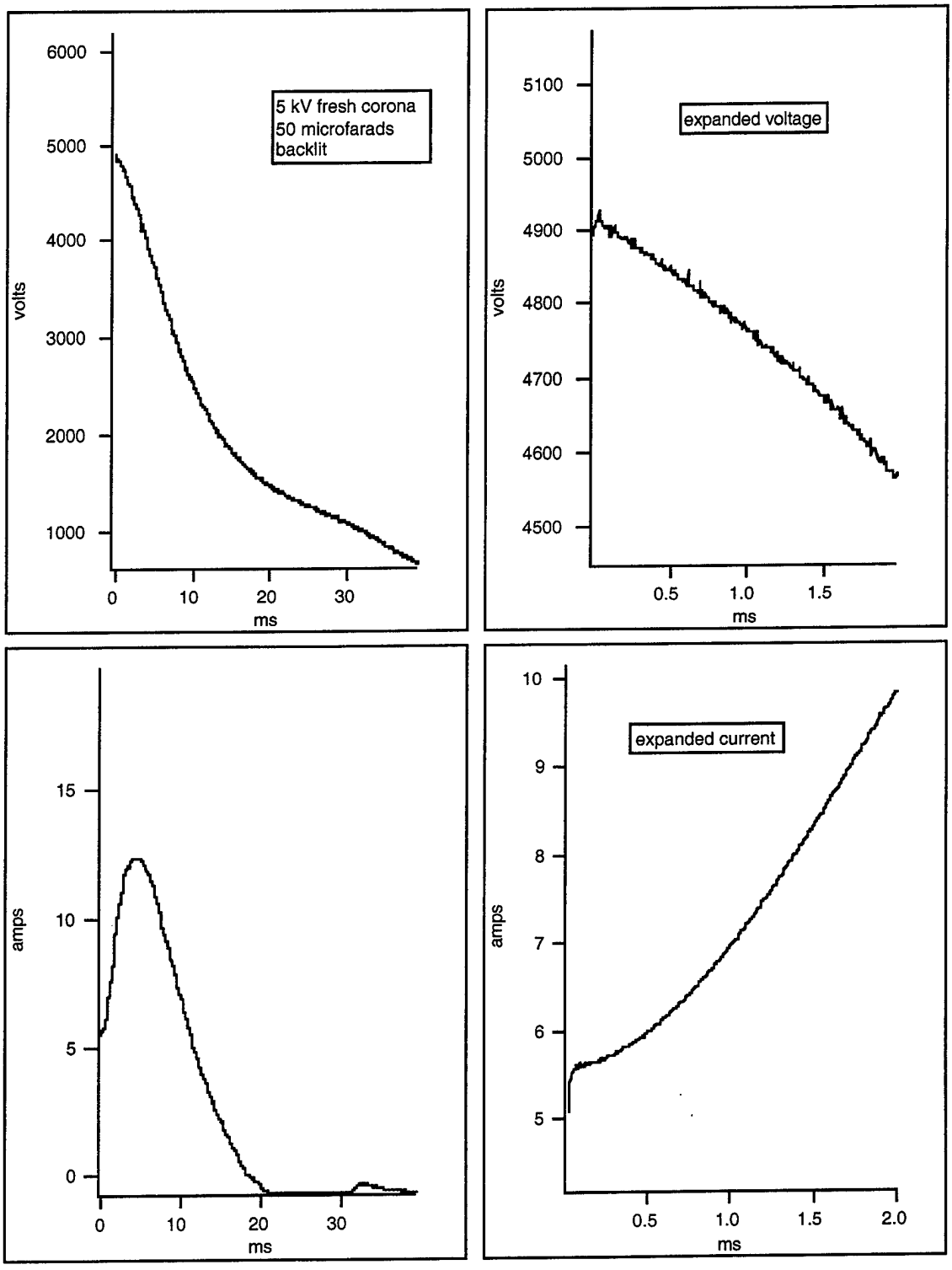

Figure 2.41

Voltage and current.

AS-99-41

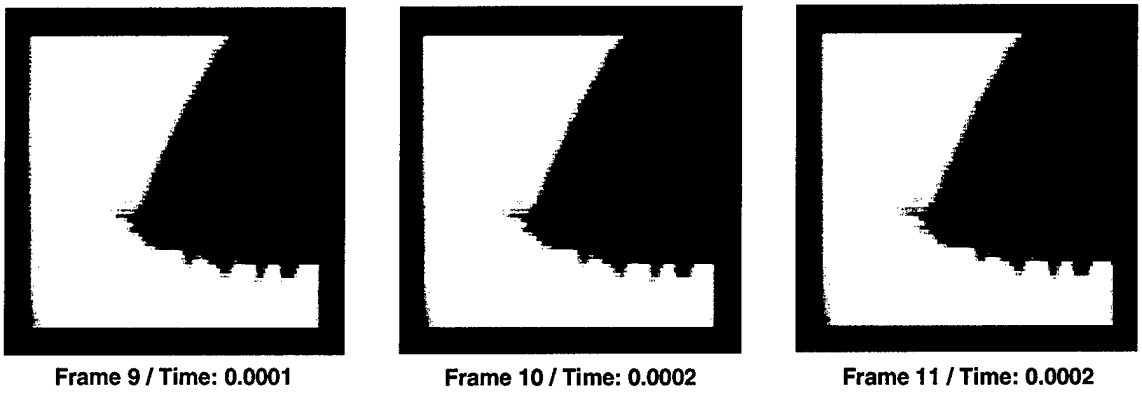

Frame 9 / Time: 0.0001 | Frame 10 / Time: 0.0002 | Frame 11 / Time: 0.0002

Frame 12 / Time: 0.0002 | Frame 13 / Time: 0.0002 | Frame 14 / Time: 0.0003

Frame 15 / Time: 0.0003 | Frame 16 / Time: 0.0003 | Frame 17 / Time: 0.0003

Frame 18 / Time: 0.0004 | Frame 19 / Time: 0.0004 | Frame 20 / Time: 0.0004

ID No. 8
Rec. Rate: 40500

Figure 2.42

Photographs corresponding to Fig. 2.41, frames 1—20.

AS-99-42

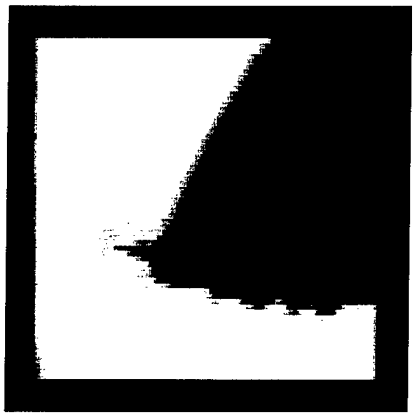

Frame 25 / Time: 0.0005

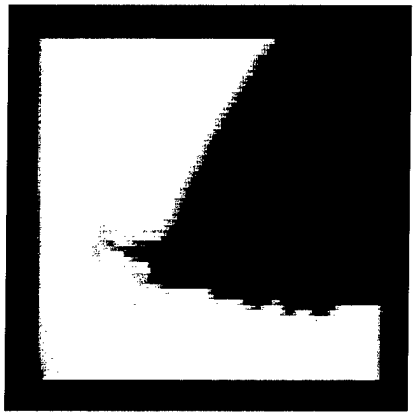

Frame 30 / Time: 0.0007

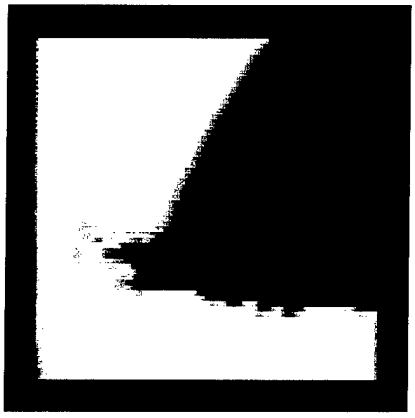

Frame 40 / Time: 0.0009

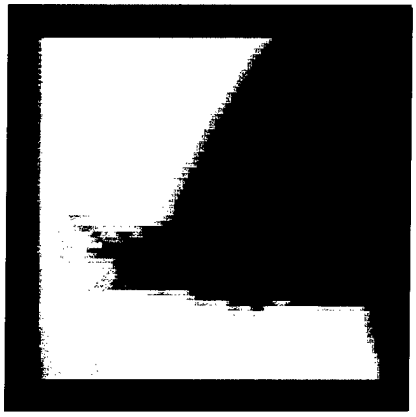

Frame 50 / Time: 0.0012

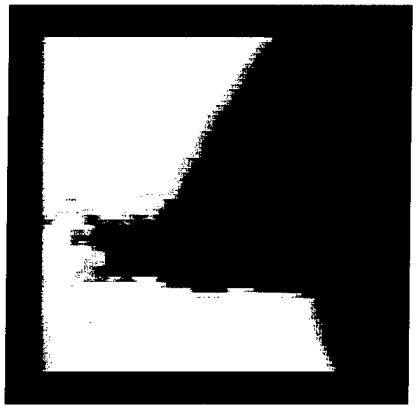

Frame 60 / Time: 0.0014

ID No. 8
Rec. Rate: 40500

Figure 2.43

Photographs corresponding to Fig. 2.41, frames 25—60.

AS-99-43

2.5 CONCLUSION

The foregoing experimental evidence demonstrates that new ideas are needed to explain dielectric breakdown in water. Steam generation appears to be a byproduct and not a precursor of arc formation. Ionic heating only serves to divert energy away from leader formation. Electron avalanches at liquid densities are not possible because of the large energy gap between the conduction and valence bands. The only possible explanation left, which is in concurrence with the observed data, is the creation of a proton cascade. The activation energies for creation and transport of a proton cascade are far smaller than those needed for the creation of steam or electron avalanches. Enhanced proton transport combined with dissociation of water molecules explain qualitatively the macroscopic phenomenology; it is this successful explanation, combined with the microphysics of water, that forces one to accept this new idea in spite of the difficulty of calculating the properties of these quasiparticles.

This page intentionally left blank.

3.0 PHYSICAL DYNAMICS OF AN ARC IN WATER

3.1 INTRODUCTION

The arc phase (compared to the breakdown phase) of a high voltage discharge into water was investigated using a newly developed fluid code in one-dimensional cylindrical coordinates in the radial direction. The external driving circuit was modeled as an RLC circuit. The energy was introduced into the bubble by the arc through the bubble's resistance. Multiple species ionization within each interior slice was allowed to take on any state from water vapor to doubly ionized oxygen. The influx of water vapor, and therefore the cooling of the bubble boundary, was due to the absorption of blackbody radiation. This boundary cooling induced acoustic pulses within the bubble because of an increasing temperature gradient in time and space. The pressure of the high temperature core was equalized by the lower temperature, but higher density, bubble boundary. This high density bubble boundary was formed by the influx of water molecules and convective flow from the interior. The net effect was a very hot core with a bubble boundary that had a much lower temperature but higher density. Possible applications to fusion were discussed.

An electrical discharge into water can be decomposed into three parts: the corona (breakdown) phase; the arc phase; and a hydrodynamic phase. The initial or corona phase deals with the formation of the leaders and/or steam bubble which eventually connects the two electrodes. Once the connection is made, the resistance between the electrodes drops very quickly, which leads to the arc phase. During the final or hydrodynamic phase, the arc current ceases and the bubble evolution is determined by the pressure of the bubble and inertia of the water. While there is still considerable controversy about the physics in the prebreakdown phase, the arc phase is believed to be better understood. To date, the arc phase is believed to have a spherical geometry and to be uniform throughout.[65, 13] In this report, the arc phase is considered to be cylindrical in geometry and allows for spatial (axial) nonuniformity in the dynamic variables.

Figure 3.1 shows schematically how the current direction is related to the mechanical configuration of the arc model. The nonlinear inviscid fluid equations were used with the ideal gas equation of state with variable numbers of constituent components (depending on the ionization and dissociation states of the original component gases). The simulations include any state of water: water vapor to double ionized oxygen, thermal conduction because of electrons and radiation in the bubble interior, mass influx because of vaporization of the bubble boundary by blackbody radiation, energy loss by that blackbody radiation, and energy input because of the resistance of the bubble. This is shown schematically in Fig. 3.1. Although the arc phase is believed to be better understood, the diagnostic techniques available to measure any of the computed parameters of the interior plasma are very limited. Thus, there are no known methods available to verify many of the results given here.

The study of the arc phase has importance beyond its obvious physical interest. This is where the electrical energy from the capacitor is converted into the mechanical, thermal, and electromagnetic energy of the bubble. For practical applications such as sound sources or lithotripsy, the developer may wish to maximize the energy entering the bubble, or the way it is distributed in time or space. To this end it is necessary to understand the physics of the arc phase.

3.2 THEORY

3.2.1 Dynamics for the Exterior

The evolution of the water in the exterior of the bubble is modeled through the nonlinear fluid equations. The continuity equation is

$$\frac{\partial \rho}{\partial t} + \nabla \bullet \rho \mathbf{v} = 0 \quad , \tag{3.1}$$

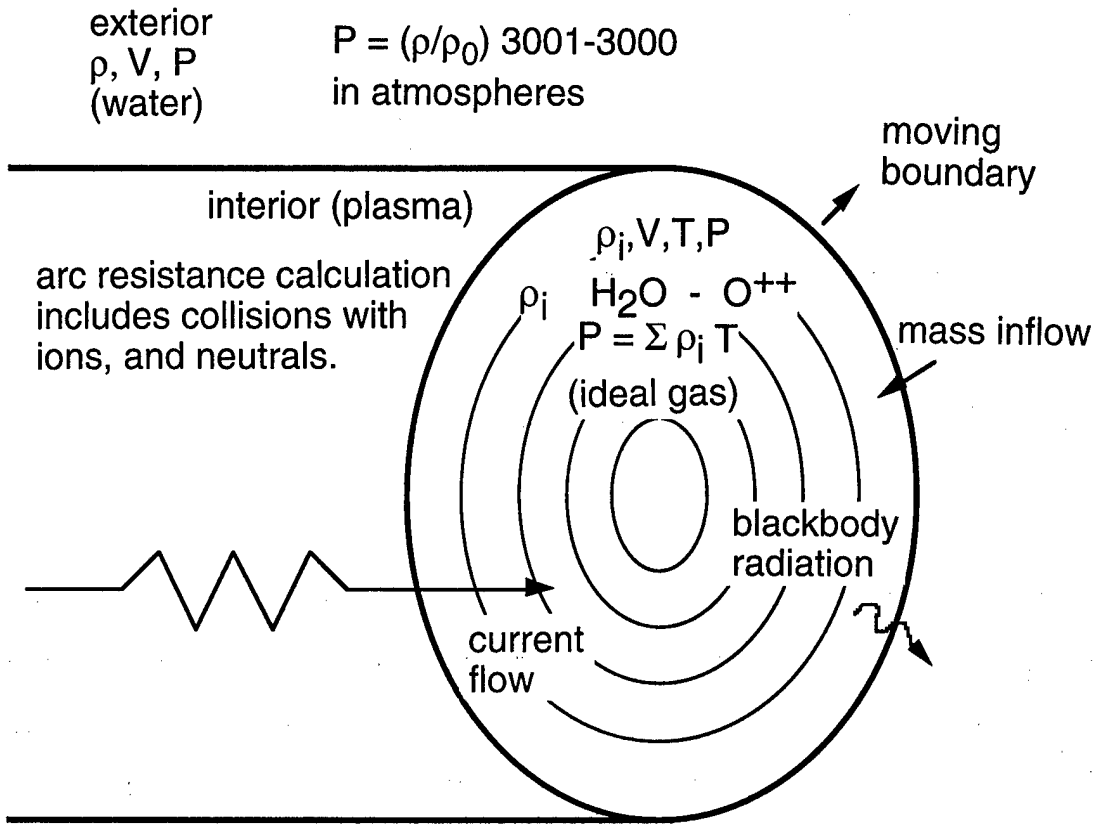

- Interior and Exterior Discretization

- 1-D Axially Symmetric Nonlinear Fluid Code

- Two-Fluid System -- Interior Gas (Plasma) and Exterior Liquid Water

- Moving boundary Followed by Moving Coordinate System

- Energy Input from Capacitor through the Resistance of Each Slice of the Bubble Modeled as RLC Circuit

- Mass Inflow from Heating by Blackbody Radiation

Figure 3.1

Diagram of the arc phase model.

AS-99-44

the momentum equation is

$$\frac{\partial \mathbf{v}}{\partial t} + \mathbf{v} \bullet \nabla \mathbf{v} = \frac{-\nabla P}{\rho} \quad , \tag{3.2}$$

and the empirical isentropic equation of state is

$$P = \frac{A\rho}{\rho_0} - B \quad , \tag{3.3}$$

where A is 3001 atm of pressure, B is 3000 atm of pressure, ρ_0 is the density of the water at 1 atm, P is the pressure, ρ_0 is the density and **v** is the fluid velocity. Although the equations shown here are for a general velocity vector, only the radial component of velocity is computed; the θ and z components (circumferential and longitudinal components, respectively) are assumed to be zero. The exterior is made discrete for the simulations on an expanding grid in a one-dimensional, axially symmetric coordinate system. As the bubble boundary evolves, the grid expands, i.e., the grid point initially at the bubble boundary follows the boundary with a uniformly spaced but expanding grid. The pressure on the boundary is determined by the dynamics inside the bubble.

3.2.2 Dynamics for the Interior

The evolution of the interior is considerably more complex than the simple one-species evolution of the exterior. Each slice of the interior contains multiple ionization species from water vapor to doubly ionized oxygen. The density of each species is a function of the temperature and pressure.[66] The interior is assumed to be an ideal gas and all the species in a slice are assumed to be in thermal equilibrium and have the same velocity **v**; as before, only the radial

component is computed. Therefore the continuity equation is

$$\frac{\partial n_i}{\partial t} + \nabla \bullet n_i \mathbf{v} = S_i \quad , \tag{3.4}$$

where n_i is the *number density* of each species, and S_i is the source for each species due to mass influx at the boundary. The influx of water molecules at the boundary is distributed across several mean free path lengths from the boundary. The water influx from the boundary in each slice is brought into thermal equilibrium with the rest of the matter in that slice.

The equation of state for an ideal gas is then used to determine the pressure:

$$P = \sum n_i kT = nkT \tag{3.5}$$

where P is the pressure, T is the temperature, k is Boltzmann's constant, and n_i is the number density of each species. Also the total number density of particles is:

$$n = \sum n_i \quad . \tag{3.6}$$

Then the momentum equation becomes:

$$\frac{\partial \mathbf{v}}{\partial t} = -\frac{\nabla P}{\rho} - \mathbf{v} \bullet \nabla \mathbf{v} \quad , \tag{3.7}$$

where **v** is the velocity and ρ is the effective mass density and is computed by:

$$\rho^* = \sum M_i n_i \quad , \tag{3.8}$$

where M_i is the mass per particle of the ith species. The energy equation is

$$C_p(T)\frac{\partial T}{\partial t} = C_p(T)\mathbf{v} \bullet \nabla T + \nabla \bullet (\kappa \nabla T) + \frac{I^2}{\sigma} \quad , \tag{3.9}$$

where $C_p(T)$ is the specific heat at constant pressure, κ is the thermal conduction coefficient, I is the electrical current, and σ is the electrical conductivity. The calculation of the temperature is determined from the internal energy and the specific heat, which is a function of temperature. The specific heat includes the energy change due to dissociation and ionization of water. Included in the internal energy change is thermal conduction due to electrons and radiative transfer. Energy transfer due to radiative effects are calculated using the Rosseland approximation[67] along with a smooth cutoff, once the Rosseland mean free path becomes larger than the bubble dimensions. Also included is the energy loss resulting from blackbody radiation leaving the bubble. The emissivity of the bubble is calculated using the Rosseland approximation to determine the mean free path and an equivalent spherical bubble radius for a uniform temperature sphere.[65] The weighted average temperature of the bubble is used in determining the mean free path and emissivity. This energy loss by the core is returned to the bubble via the water vapor that enters the bubble through vaporization of the bubble wall.

The energy transferred to the bubble from the electrical circuit is determined from the current (I) and the conductivity (σ) of the bubble. The electrical circuit is an RLC circuit where the resistance R is composed of the line resistance of the cable feeding the arc and the time-varying resistance of the bubble. This equivalent circuit model is shown in Fig. 3.2. The resistance of the bubble is determined through contributions from the plasma through Spitzer's

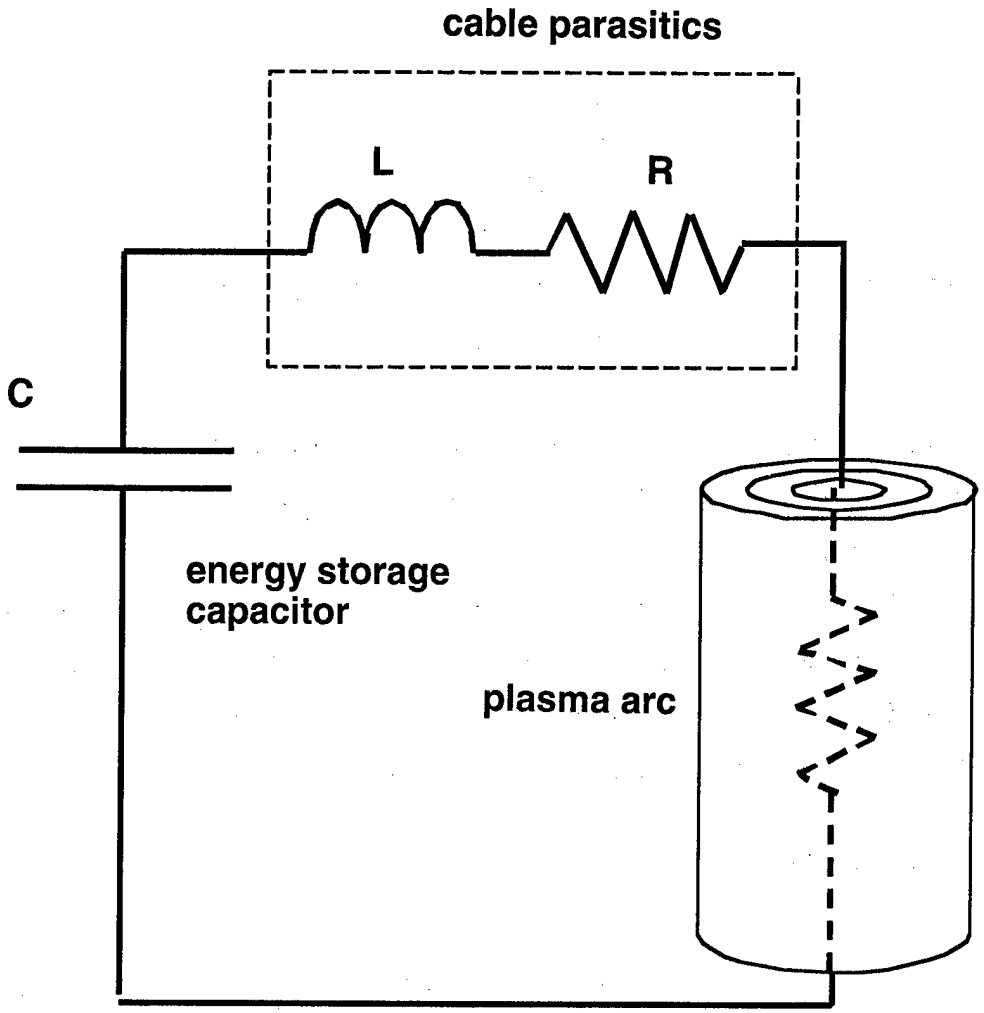

Figure 3.2

Equivalent circuit used in arc model calculations.

AS-99-45

formula,[68] and also those contributions due to the neutrals. The electrical conductivity is determined by the receptacle sum of the conductivity from the plasma and the neutrals.

$$\frac{1}{\sigma} = \frac{1}{\sigma_{plasma}} + \frac{1}{\sigma_{neutral}} \quad . \tag{3.10}$$

Included are cutoffs to take into account the finite size of the electrodes when determining the resistance of the bubble.

The electrode's true experimental configuration is actually a flat-face electrode with a central disk and a concentric ring comprising the anode and cathode. As the bubble expands, the central path length of the cylinder increases for each internal slice. This effect is included by increasing the path length used to determine the resistance as well as the energy per unit length deposited due to the bubble resistance. This length is determined each time step based on the electrode spacing and bubble radius.

3.3 COMPUTATIONAL METHODS

The partial differential equations for the interior and exterior previously described were discretized. All the variables are considered to be functions of only the cylindrical radial coordinate and time. This gives the geometry of a long cylindrical bubble expanding in the radial direction. The discretization of the radial coordinates is done in a moving coordinate system. The number of slices inside and outside the bubble is a constant in time allowing the bubble boundary to be always at a fixed discretization slice that moves with the bubble as the bubble expands. Although the discretization spacing distance varies in time, spacing in the interior and exterior of the bubble is uniform. The fluid equations for the interior and exterior are evolved by the McCormack method,[69] and the order of the discretization (forward or backward) is reversed on each time step. The resistance of the plasma in an RLC circuit is shown in Fig. 3.2. An initial

voltage on the capacitor provides the driving energy for the arc, and the inductance and linear resistance in the circuit account for the parasitics introduced by the cable. The voltage and current in the circuit are calculated through a fourth order Runge-Kutta solver, simultaneously with the parameters of the plasma.

As shown in Fig. 3.1, the interior of the bubble includes water from steam to double-ionized oxygen. The amount of each component of water depends upon the temperature and pressure within that particular discretization slice. The resistance per unit length of each slice of the bubble is calculated based on Spitzer's formula as described previously. The parallel resistance of each slice, along with the bubble length, is used to calculate the total resistance of the bubble. The electrode spacing and the radius of the bubble determine the bubble length used to calculate the resistance for the simulation. This resistance is used in the Runge-Kutta solver to determine the voltage drop across the bubble. The current through each slice of the bubble is then calculated along with the energy deposited into each slice due to the resistance of that slice. In each discretization slice, the density of each component, the ionized water vapor, the temperature, pressure, resistance, specific heat, and radial velocity are all tracked at each time step. In addition, the voltage and current through the system, the discretization spacing, water vapor influx through the bubble boundary, energy loss due to blackbody radiation, and the radiative mean free path and emissivity of the bubble are also tracked at each time step.

3.4 SIMULATION RESULTS

Evolution of the fluid equations is accomplished through the use of a McCormack solver for both the interior and exterior equations. The order of the discretization (forward or backward) is reversed on each time step. The RLC circuit is calculated through a fourth order Runge-Kutta solver.

During the initial phase of bubble growth, the interior temperature of the bubble grows at a spatially uniform rate. However, as blackbody radiation is absorbed by the boundary and, as a consequence, water on the boundary is vaporized, the rate of change of the bubble boundary temperature slows or reverses sign compared to the bubble's interior. Blackbody radiation transfers energy from the hot interior to the exterior and bubble wall. As mass flows into the bubble from the boundary, there are two competing effects. The mass flowing into the boundary and energy from the arc tend to increase the boundary pressure; however, at the same time the boundary is cooled because of the cooler temperature of the mass influx and work done in expanding the bubble. This influx of mass at the boundary initially reduces the boundary pressure, as a result of the temperature dependence of the pressure, while the core temperature increases. Although the boundary cools, blackbody radiation from the core continues to cause mass influx into the boundary. This is partly illustrated in Fig. 3.3, which shows the temperature at five different radii from the core of the bubble to the boundary as a function of time. The highest temperature is at the bubble core and the coolest temperature is at the bubble boundary. Initially, the temperature is uniform as the bubble grows. As the temperature of the bubble increases, and therefore the blackbody radiation increases, water is vaporized on the bubble boundary. This influx of water cools the bubble boundary, causing a large spatial temperature gradient. The bounces of the acoustic pulses within the bubble are apparent from the oscillation of temperature as the pulses transverse the bubble.

As the boundary temperature approaches that of the mass influx, the temperature change caused by this mass influx decreases and, finally, the boundary pressure starts to increase as the density increases. Eventually, the pressure on the boundary surpasses that of the interior, causing mass to flow towards the interior. This induces acoustic pulses that reflect between the origin and boundary. These pulses are reinforced by the increasing pressure gradient in time and space at the boundary. Evidence of this process is shown in Fig. 3.4, which shows the radial velocity at the total bubble radius as a function of time.

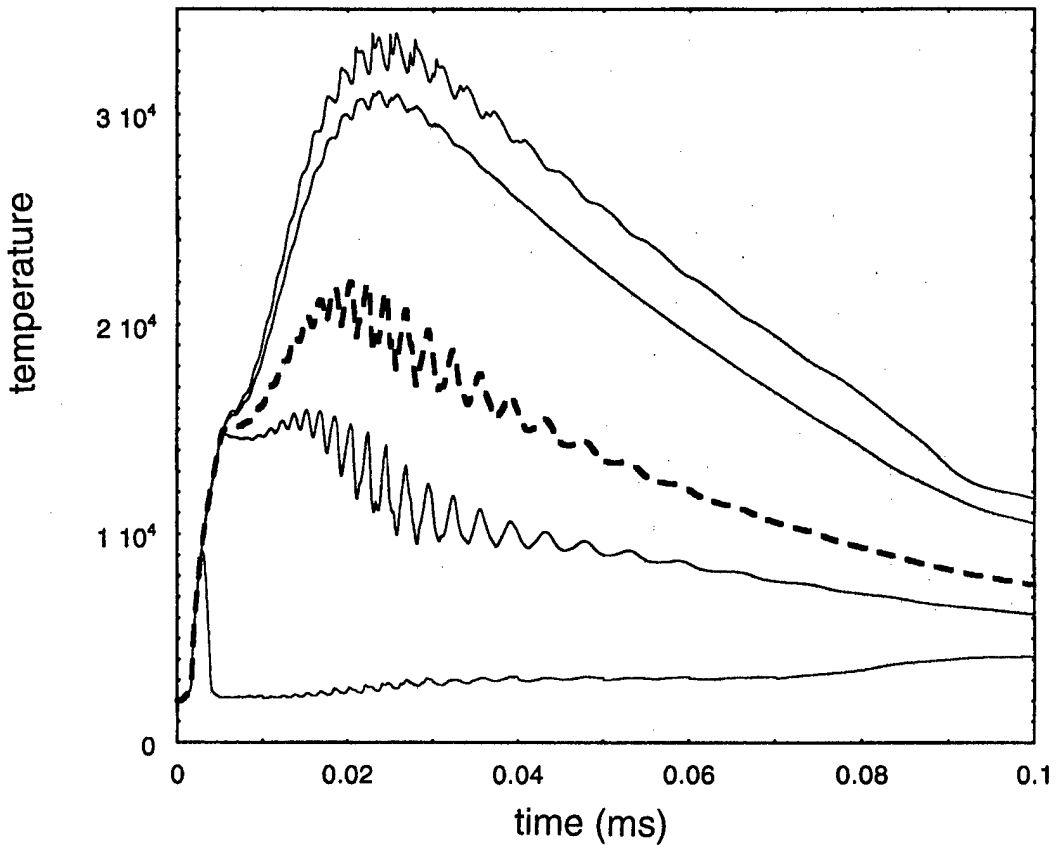

Figure 3.3
Temperature at five different radii.

AS-99-46

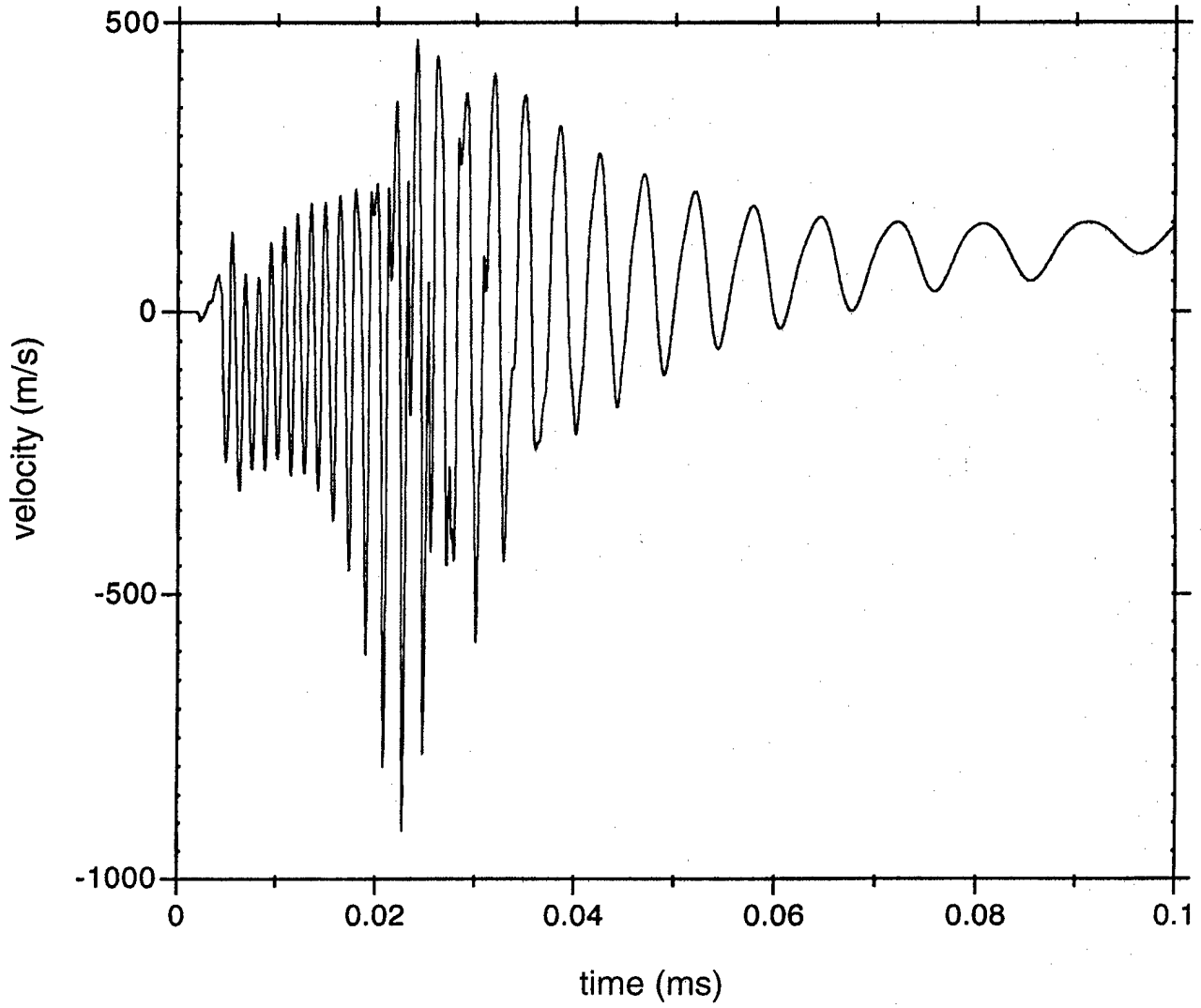

Figure 3.4

Radial velocity at a single radius.

AS-99-47

As the bubble radius increases with time, the period of the time for the acoustic pulses to transverse the bubble increases. This is seen in the increasing wavelength of the oscillations in velocity. Figure 3.5 shows the radial velocity through approximately one bounce of the acoustic wave within the bubble at five different times. The acoustic pulse is initially at position 1 and progresses to position 5, which then returns to approximately the form of 1.

During the time the bubble wall is accelerating, the energy loss caused by the acoustic pulse traveling towards the boundary is more than made up for by the pulse traveling away from the boundary. This is due to the increasing pressure gradient in time as the boundary is approached. Therefore, the pulse has a net gain in energy. During bubble wall deceleration, the opposite effect takes place and there is a net loss in energy by the acoustic pulses. During this phase, the amplitude of the acoustic pulses decreases. Depending upon the capacitor voltage and RLC parameters, the internal acoustic pulses may develop into nonlinear shock structures.

3.5 SUMMARY AND DISCUSSION

Using a high voltage spark in water as an acoustic source is well known, but there are other possible applications for this. One application could be the use of the hot core for high temperature fusion; another application could be as a light source.

The influx of mass at the bubble boundary caused by blackbody radiation sets up acoustic pulses that reflect at the bubble boundary and axis. The amplitude of the acoustic pulses increases during the acceleration phase of the bubble growth and decreases during the deceleration phase. Energy is coupled into the water as the acoustic pulses within the bubble reflect off the bubble boundary. These internal acoustic pulses are observed riding on the main acoustic pulse in the water in both simulations and experiments.

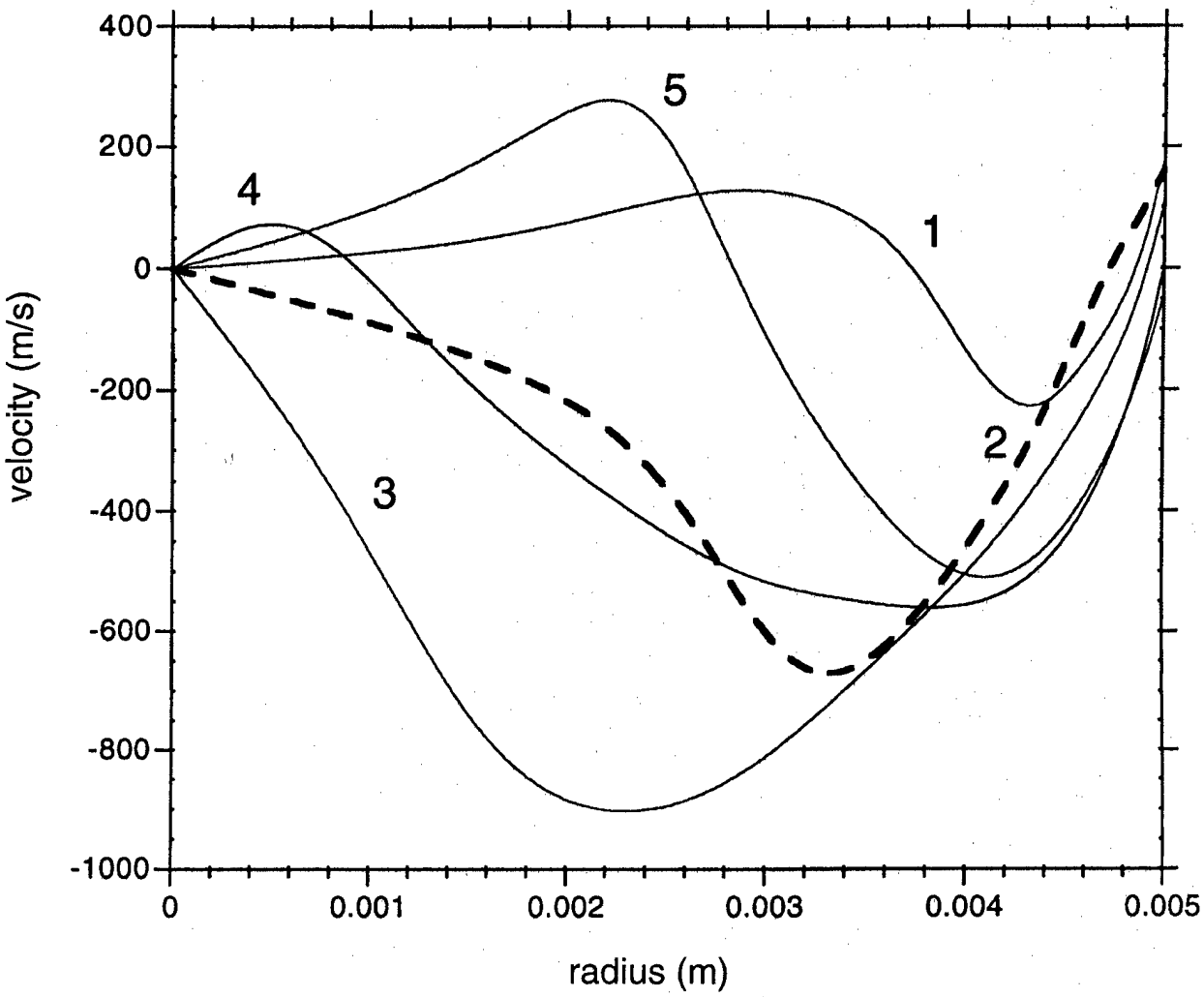

Figure 3.5
Radial velocity at five different times.

AS-99-48

4.0 CONCLUSION

Understanding the mechanisms associated with the breakdown of water is critical for the advancement of PSS technology and requires better understanding of the mechanisms involved with the dielectric breakdown of water. It also requires a more complete understanding of the internal dynamics of the arc formed after breakdown, which is primarily responsible for the production of sound.

This report described a general theoretical approach of modeling dielectric breakdown in water as well as providing a review of experimental evidence from the literature and experiments performed at ARL:UT that supports the notion of a leader structure being the primary mechanism for breakdown. Experimental evidence indicates that the steam-bubble breakdown model is not likely to be correct. Some photographs showed bubbles resident on the electrode, but these bubbles did not show any evidence of being initiation points for breakdown. Thermally created bubbles were observed in high speed photographs, as well as acoustically, but they occurred after the leader structure formed.

Because electrons are relatively immobile in water and the energy to create a free electron is of the order of 9 eV, it is unlikely that electrons are the charge carriers in the leaders. In contrast, protons only require 0.5 eV of energy to become mobile. Furthermore, in weak fields, ionic conduction is the accepted mechanism for conduction. This strongly suggests that the protons are more likely to be the mobile carriers than electrons.

Further effort in this area should concentrate on quantitative assessment of this model, as well as orienting toward a time-evolution model of the leader formation. Also, it may be possible to obtain more definitive experimental evidence for protonic charge transport by observing the properties of deuterium water (D_2O) and comparing it with ordinary water (H_2O). If protons are indeed the charge carriers in ordinary water, differences in the masses of the charge

carriers, H^+ and D^+ ions, should cause differences in the rates of leader growth and branching, while the electronic structures of deuterium and ordinary water would remain identical.

The hydrodynamic model shows that the internal dynamics of the arc are complex and interesting. Interior gradients in temperature and density cause internal acoustic waves to propagate radially from the center of the arc channel. The oversimplified geometry of this model limits its practical usefulness, but it shows that most of the current, and hence most of the heating, occurs in a small core in the center of the plasma. The particle transport to the outer layers of the plasma dramatically alters the parameters of the outermost layers.

Future work in this area should focus on the calculation of arc dynamics in a realistic electrode geometry. However, the three-dimensional calculations are very complex. Furthermore, to correctly model the arc behavior, effects such as magnetohydrodynamic (MHD) instabilities will need to be included.

This work has laid the groundwork for a greater understanding of the processes of dielectric breakdown and arc formation in water. Further technological advances and the development of advanced plasma sound source designs will require more detailed understanding of these processes.

APPENDIX A
PRESENTATIONS AND PUBLICATIONS

This page intentionally left blank.

Presentations given under Grant N00014-94-1-0150, Plasma Sound Source Basic Research:

"Modifications of a Fractal Model for a Corona Discharge," J. Espinosa, R. L. Rogers, A. M. Gleeson, 131st Meeting of the ASA, May 16, 1996, Indianapolis, IN.

"Assessment of a Fractal Model for Corona Discharges in Salt Water," J. Espinosa, H. M. Jones, A. M. Gleeson, R. L. Rogers, 130th Meeting of the ASA, Nov. 28, 1995, St. Louis, MO.

No papers or reports were published under Grant N00014-94-1-0150, Plasma Sound Source Basic Research.

This page intentionally left blank.

REFERENCES

1. R. L. Rogers, "Intermediate Energy Tests and Analysis of a Plasma Sound Source," Applied Research Laboratories Technical Report No. 92-15 (ARL-TR-92-15), Applied Research Laboratories, The University of Texas at Austin (June 1992).

2. R. M. Roberts, "The Energy Partition of Underwater Sparks," Applied Research Laboratories Technical Report No. 93-9 (ARL-TR-93-9), Applied Research Laboratories, The University of Texas at Austin (May 1993).

3. J. A. Cook, "Interaction of Multiple Spark-Generated Bubbles in a Compressible Liquid," Applied Research Laboratories Technical Report No. 93-10 (ARL-TR-93-10), Applied Research Laboratories, The University of Texas at Austin (June 1993).

4. N. P. Mel'nikov, G. A. Ostroumov, and M. Yu. Stoyak, "The Development of an Electric Discharge in Aqueous Electrolytes," Soviet Physics-Doklady **8**(2), 176-1789 (1963).

5. I. M. Garvrilov, V. R. Kukhta, V. V. Lopatin, P. G. Petrov, and V. Ya Ushakov, "Impulsive Discharge Formation in Water," Soviet Physics Journal **32**(1), 74-78 (1989).

6. I. M. Gavrilov, V. R. Kukhta, V. V. Lopatin, and P. G. Petrov, "Dynamics of Prebreakdown Phenomena in a Uniform Field in Water," IEEE Trans. Elec. Ins. **1**(3), 496-502 (1994).

7. E. V. Yanshin, I. T. Ovchinnikov, and Yu. N. Versinin, "Optical Study of Nanosecond Prebreakdown in Water," Sov. Phys. Tech. Phys. **18**(10) 1301-1306 (1974).

8. V. Kukhta and V. Lopatin, "Discharge Propagation in Water in Nonuniform Field," Conference Record of the ICDL 96, 259-262 (1996).

9. J. Sidney Clements, M. Sato, and R. H. Davis, "Preliminary Investigation of Prebreakdown Phenomena and Chemical Reactions Using a Pulsed High-Voltage Discharge in Water," IEEE Trans. Indust. Appl. **IA-23**(2), 224-234 (1987).

10. L. G. Kutsenko and A. V. Kortnev, "Pulse Breakdown in Aqueous Solutions of Lithium Chloride," Ukranian Physics Journal **12**(9), 1490-1494 (1967).

11. H. M. Jones and E. E. Kunhardt, "Prebreakdown Currents in Water and Aqueous Solutions and Their Influence On Pulsed Dielectric Breakdown," Journal of Applied Physics **78**(5), 3308-3314 (1995).

12. K. A. Naugol'nykh, and N. A. Roi, *Spark Discharges in Water: A Hydrodynamical Description* (Nauka Publishing Co., Moscow, USSR, 1971).

13. N. P. Mel'nikov, G. A. Ostroumov, and M. Yu. Stoyak, "Formation of Electrical Breakdown in Aqueous Sodium Chloride Solutions," Soviet Physics Technical Physics **9**(5), 730-733 (1964).

14. H. M. Jones and E. E. Kunhardt, "Development of Pulsed Dielectric Breakdown in Liquids," Journal of Physics D **28**(1), 178-188 (1995).

15. A. P. Alkhimov, V. V. Vorobtev, V. F. Klimkin, A. G. Ponomarenko, and R. I. Soloukhin, "The Development of Electrical Discharge in Water," Sov. Phys.-Doklady **15**(10), 959-961 (1991).

16. D. B. Fenneman and R. J. Gripshover, "Experiments on Electrical Breakdown in Water in the Microsecond Regime," IEEE Trans. Plasma Sci. **PS-8**(3), 209-213 (1980).

17. N. J. Felici, "Blazing a Fiery Trail with the Hounds (Prebreakdown Streamers)," IEEE Trans. Elect. Insul. **23**(4), 497-503 (1988).

18. A. H. Olson and S. P. Sutton, "The Physical Mechanisms Leading to Electrical Breakdown in Underwater Arc Sound Sources," J. Acoust. Soc. Am. **94**(4), 2226-2231 (1993).

19. P. Krebs, "Localization of Excess Electrons in Dense Polar Vapors," J. Phys. Chem. **88**, 3702-3709 (1984).

20. P. G. Petrov, V. P. Kukhta, and V. V. Lopatin, "On the Nature of Anode Streamers in Water," Sov. Phys. Tech. Phys. **33**(6), 697-699 (1988).

21. V. M. Kosenkov and N. I. Kuskova, "Development of Breakdown in Water," Sov. Phys. Tech. Phys. **32**(10), 1215-1217 (1975).

22. C. D. Jonah, D. M. Bartels, and A. C. Chernovitz, "Primary Processes in the Radiation Chemistry of Water," Radiat. Phys. Chem. **34**(1), 145-156 (1989).

23. T. Goulet, A. Bernas, C. Ferradini, and J.-P. Jay-Gerin, "On the Electronic Structure of Liquid Water: Conduction-Band Tail Revealed by Photoionization Data," Chem. Phys. Letters **170**(5,6), 492-496 (1990).

24. D. Eisenberg and W. Kauzmann, *The Structure and Properties of Water* (Oxford University Press, Oxford, 1969).

25. E. J. Hart and M. Anbar, *The Hydrated Electron* (Wiley-Interscience, New York, 1970).

26. K. H. Schmidt, P. Han, and D. M. Bartels, "Temperature Dependence of Solvated Electron Diffusion in Water and Heavy Water," J. Phys. Chem. **96**, 199-206 (1992).

27. M. Kiselev and K. Heinzinger, "Molecular Dynamics Simulation of a Chloride Ion in Water under the Influence of an External Electric Field," J. Phys. Chem. **105**(2), 650-657 (1996).

28. J. Lobaugh and G. A. Voth, "The Quantum Dynamics of an Excess Proton in Water," J. Phys. Chem. **104**(5), 2056-2069 (1996).

29. M. Tuckerman, K. Laasonen, M. Sprik, and M. Parrinello, "*Ab Initio* Molecular Dynamics Simulation of the Solvation and Transport of Hydronium and Hydroxyl Ions in Water," J. Phys. Chem. **99**, 5749-5752 (1990).

30. M. Tuckerman, K. Laasonen, M. Sprik, and M. Parrinello, "*Ab Initio* Molecular Dynamics Simulation of the Solvation and Transport of Hydronium and Hydroxyl Ions in Water," J. Phys. Chem. **103**(1), 150-161 (1995).

31. M. E. Tuckerman, D. Marx, M. L. Klein, and M. Parrinello, "On the Quantum Nature of the Shared Proton in Hydrogen Bonds," Science **275**, 817-820 (1997).

32. A. Luzar and D. Chandler, "Hydrogen-Bond Kinetics in Liquid Water," Nature **379**, 55-57 (1996).

33. M. F. Toney et al., "Distribution of Water Molecules at Ag(111)/Electrolyte Interface as Studied with Surface X-Ray Scattering," Surf. Sci. **335**, 326-332 (1995).

34. X. Xia and M. L. Berkowitz, "Electric Field Induced Restructuring of Water at a Platinum-Water Interface: A Molecular Dynamics Computer Simulation," Phys. Rev. Lett. **74**(16), 3193-3196 (1995).

35. X. Xia, L. Perera, U. Essmann, and M. L. Berkowitz, "The Structure of Water at Platinum/Water Interfaces: Molecular Dynamics Computer Simulations," Surf. Sci. **335**, 401-415 (1995).

36. K. J. Schweighhofer, X. Xia, and M. L. Berkowitz, "Molecular Dynamics Study of Water next to Electrified Ag(111) Surfaces," Langmair **12**(16), 3747-3752 (1996).

37. K. Laasonen, M. Sprik, M. Parinello, and R. Car, "*Ab initio* liquid water," J. Phys. Chem. **99**(11), 9080-9089 (1993).

38. R. N. Barnett, U. Landman, and A. Nitzan, "Excess Electron Transport in Water," J. Phys. Chem. **93**(11), 8187-8195 (1990).

39. E. S. Fois, M. Sprik, and M. Parrinello, "Properties of Supercritical Water: an *Ab Initio* Simulation," Chem. Phy. Letters **223**, 411-415 (1994).

40. P. J. Rossky and J. Schnitker, "The Hydrated Electron: Quantum Simulation of Structure, Spectroscopy, and Dynamics," J. Phys. Chem. **92**, 4277-4285 (1988).

41. J. Schnitker and P. J. Rossky, "Excess Electron Migration in Liquid Water," J. Phys. Chem. **93**, 6965-6969 (1989).

42. St. Pnevmatikos, A. V. Savin, A. V. Zolotaryuk, and Yu. S. Kivshar, "Nonlinear Transport in Hydrogen-Bonded Chains: Free Solitonic Excitations," Phys. Rev. A **43**(10), 5518-5536 (1991).

43. A. V. Zolotaryuk, St. Pnevmatikos, and A. V. Savin, "Charge Transport by Solitons in Hydrogen-Bonded Materials," Phys. Rev. Lett. **67**(6), 707-710 (1991).

44. A. Zolotaryuk and St. Pnevmatikos, "One-Component Model for Proton Transport in Hydrogen-Bonded Chains," Phys. Lett. A **143**(4,5), 233-238 (1990).

45. G. P. Tsironis and St. Pnevmatikos, "Proton Conductivity in Quasi-One-Dimensional Hydrogen-Bonded Systems: Nonlinear Approach," Phys. Rev. B **39**(10), 7161-7173 (1989).

46. St. Pnevmatikos, "Soliton Dynamics of Hydrogen-Bonded Networks: A Mechanism for Proton Conductivity," Phys. Rev. Lett. **60**(15), 1534-1537 (1988).

47. E. S. Nylund and G. P. Tsironis, "Evidence for Solitons in Hydrogen-Bonded Systems," Phys. Rev. Lett. **66**, 1886-1889 (1991).

48. V. Ya. Antonchenko, A. S. Davydov, and V. P. Krainov, "Solitons and Proton Motion in Ice-Like Structures," Phys. Stat. Sol. B **115**, 631-640 (1983).

49. P. V. Hobbs, *Ice Physics* (Clarendon Press, Oxford, 1974).

50. G. P. Parravicini and L. Resca, "Electronic States and Optical Properties in Cubic Ice," Phys. Rev. B **8**(6), 3009-3023 (1973).

51. K. Kobayashik, "Optical Spectra and Electronic Structure of Ice," J. Phys. Chem. **87**, 4317-4321 (1983).

52. N. Mott, *Metal-Insulator Transitions* (Taylor and Francis, New York, 1990).

53. F. Gebhard, *The Mott Metal-Insulator Transition: Models and Methods* (Springer-Verlag, New York, 1997).

54. O. Madelung, *Introduction to Solid State Theory* (Springer-Verlag, New York, 1978).

55. R. E. Thorne, "Charge Density Wave Conductors," Physics Today **49**(5), 42-47 (1996).

56. Yu. S. Kivshar, A. V. Savin, M. J. Velgakis, and A. V. Zolotaryuk, "Nonlinear Transport in Hydrogen-Bonded Chains: Solitons under External Fields and Damping," International Journal of Modern Physics B **8**(8), 1033-1064 (1994).

57. St. Pnevmatikos, A. V. Savin, I. Stylianou, M. J. Velgakis, and A. V. Zolotaryuk, "Proton Transport by Solitons," Physica D **51**, 316-332 (1991).

58. M. Remoissent, *Waves Called Solitons: Concepts and Experiments* (Springer-Verlag, New York, 1994).

59. Y. P. Raizer, *Gas Discharge Physics* (Springer-Verlag, New York, 1991).

60. R. Klingbeil, D. A. Tidman, and R. F. Frensler, "Ionizing Gas Breakdown Waves in Strong Electric Fields," Phys. Fluids **15**(11), 1969-1973 (1972).

61. N. W. Albright and D. A. Tidman, "Ionizing Potential Waves and High Voltage Breakdown Streamers," Phys. Fluids **15**(1), 86-90 (1972).

62. D. L. Turcotte and R. S. B. Ong, "The Structure and Propagation of Ionizing Wave Fronts," J. Plasma Phys. **2**, 145-155 (1968).

63. L. Niemeyer, L. Pietronero, and H. J. Wiesmann, "Fractal Dimension of Dielectric Breakdown," Phys. Rev. Letters **52**(12), 1033-1036 (1984).

64. D. E. Smith, "Theory of the Underwater Spark," Applied Research Laboratories, The University of Texas at Austin, unpublished (1989).

65. R. M. Roberts, J. A. Cook, R. L. Rogers, A. M. Gleeson, and T. A. Griffy, "The Energy Partition of Underwater Sparks," J. Acoust. Soc. Am. **99**, 3465-3475 (1996).

66. L. D. Landau and E. M. Lifshitz, *Course of Theoretical Physics,* Vol. 5 (Pergamon Press, Oxford, NY, 1986).

67. Y. B. Zel'dovich and Y. P. Raizer, *Physics of Shock Waves and High-Temperature Hydrodynamic Phenomena,* Vol. 1 (Academic Press, New York, NY, 1966).

68. L. Spitzer, *Physics of Fully Ionized Gases* (Interscience Publishers, New York, NY, 1962).

69. P. J. Roache, *Computational Fluid Dynamics* (Hermosa Publishers, Albuquerque, NM, 1982).

1 July 1999

DISTRIBUTION LIST
ARL-TR-99-2
Final Technical Report under Grant N00014-94-1-0150
Plasma Sound Source Basic Research

Copy No.

DR LOGAN E HARGROVE ONR 331
OFFICE OF NAVAL RESEARCH
800 NORTH QUINCY STREET
1, 2 ARLINGTON VA 22217-5660

DEFENSE TECHNICAL INFORMATION CENTER
8725 JOHN J KINGMAN ROAD
STE 0944
3, 4 FT BELVOIR VA 22060-6218

DIRECTOR NAVAL RESEARCH LABORATORY
ATTN CODE 2667
4555 OVERLOOK AVENUE SW
5 WASHINGTON DC 20375-5326

PROFESSOR ANTHONY A ATCHLEY
GRADUATE PROGRAM IN ACOUSTICS
PENNSYLVANIA STATE UNIVERSITY
P O BOX 30
6 STATE COLLEGE PA 16804

PROFESSOR HENRY E BASS
DEPARTMENT OF PHYSICS AND ASTRONOMY
UNIVERSITY OF MISSISSIPPI
7 UNIVERSITY MS 38677

PROFESSOR YVES H BERTHELOT
SCHOOL OF MECHANICAL ENGINEERING
GEORGIA INSTITUTE OF TECHNOLOGY
8 ATLANTA GA 30332

PROFESSOR LAWRENCE A CRUM
APPLIED PHYSICS LABORATORY
UNIVERSITY OF WASHINGTON
1013 NE 40TH STREET
9 SEATTLE WA 98105-6698

DR THOMAS B GABRIELSON
GRADUATE PROGRAM IN ACOUSTICS
PENNSYLVANIA STATE UNIVERSITY
P O BOX 30
10 STATE COLLEGE PA 16804

Distribution List for ARL-TR-99-2 under Grant N00014-94-1-0150 (cont'd)

Copy No.

PROFESSOR STEVEN L GARRETT
GRADUATE PROGRAM IN ACOUSTICS
PENNSYLVANIA STATE UNIVERSITY
P O BOX 30
11 STATE COLLEGE PA 16804

DR KEITH A GILLIS
PHYSICAL AND CHEMICAL PROPERTIES DIVISION
NATIONAL INSTITUTE OF STANDARDS
AND TECHNOLOGY
12 GAITHERSBURG MD 20899-8380

PROFESSOR MARK F HAMILTON
DEPARTMENT OF MECHANICAL ENGINEERING
UNIVERSITY OF TEXAS AT AUSTIN
13 AUSTIN TX 78712-1063

PROFESSOR ROBERT M KEOLIAN
GRADUATE PROGRAM IN ACOUSTICS
PENNSYLVANIA STATE UNIVERSITY
P O BOX 30
14 STATE COLLEGE PA 16804

PROFESSOR PHILIP L MARSTON
DEPARTMENT OF PHYSICS
WASHINGTON STATE UNIVERSITY
15 PULLMAN WA 99164-2814

PROFESSOR ANDREA PROSPERETTI
DEPARTMENT OF MECHANICAL ENGINEERING
JOHNS HOPKINS UNIVERSITY
16 BALTIMORE MD 21218

17 J M HUCKABAY ARL:UT

18 R L ROGERS ARL:UT

19 J C ESPINOSA UT

20 D L FISHER ARL:UT

21 LIBRARY ARL:UT

22 ADVANCED TECHNOLOGY LABORATORY ARL:UT

23 - 32 RESERVE ADVANCED TECHNOLOGY LABORATORY